REPORT DOCUMENTATION PAGE

1. AGENCY USE ONLY (Leave blank)	2. REPORT DATE	3. REPORT TYPE AND DATES COVERED
	7 August 1998	

4. TITLE AND SUBTITLE
THE FORMATION OF THE SECOND-ORDER NONLINEARITY IN
THERMALLY POLED FUSED SILICA GLASS

5. FUNDING NUMBERS

6. AUTHOR(S)
THOMAS GUSTAVE ALLEY

7. PERFORMING ORGANIZATION NAME(S) AND ADDRESS(ES)
The University of New Mexico

8. PERFORMING ORGANIZATION REPORT NUMBER

98-020D

9. SPONSORING/MONITORING AGENCY NAME(S) AND ADDRESS(ES)
THE DEPARTMENT OF THE AIR FORCE
AFIT/CIA, BLDG 125
2950 P STREET
WPAFB OH 45433

10. SPONSORING/MONITORING AGENCY REPORT NUMBER

11. SUPPLEMENTARY NOTES

12a. DISTRIBUTION AVAILABILITY STATEMENT
Unlimited distribution
In Accordance With 35-205/AFIT Sup 1

12b. DISTRIBUTION CODE

13. ABSTRACT (Maximum 200 words)

14. SUBJECT TERMS

15. NUMBER OF PAGES
203

16. PRICE CODE

17. SECURITY CLASSIFICATION OF REPORT	18. SECURITY CLASSIFICATION OF THIS PAGE	19. SECURITY CLASSIFICATION OF ABSTRACT	20. LIMITATION OF ABSTRACT

THE FORMATION OF THE SECOND-ORDER NONLINEARITY
IN THERMALLY POLED FUSED SILICA GLASS

BY

THOMAS GUSTAVE ALLEY

ABSTRACT OF DISSERTATION

Submitted in Partial Fulfillment of the
Requirements for the Degree of

Doctor of Philosophy
Optical Science

The University of New Mexico
Albuquerque, New Mexico

August, 1998

THE FORMATION OF THE SECOND-ORDER NONLINEARITY

IN THERMALLY POLED FUSED SILICA GLASS

BY

THOMAS GUSTAVE ALLEY

B.A., Physics, University of Utah, 1984
M.S., Engineering Physics, Air Force Institute of Technology, 1987

DISSERTATION

Submitted in Partial Fulfillment of the
Requirements for the Degree of

Doctor of Philosophy
Optical Science

The University of New Mexico
Albuquerque, New Mexico

August, 1998

DEDICATION

This work is dedicated to my wonderful wife, Valerie, for her love and encouragement, and especially for her patience during the exam preparation period. It is also dedicated to my loving parents, who taught and encouraged me to be inquisitive. And finally, it's dedicated to my boys, who I wish a bright and exciting future.

ACKNOWLEDGMENTS

v

THE FORMATION OF THE SECOND-ORDER NONLINEARITY IN THERMALLY POLED FUSED SILICA GLASS

BY

THOMAS GUSTAVE ALLEY

ABSTRACT OF DISSERTATION

Submitted in Partial Fulfillment of the
Requirements for the Degree of

Doctor of Philosophy
Optical Science

The University of New Mexico
Albuquerque, New Mexico

August, 1998

THE FORMATION OF THE SECOND-ORDER NONLINEARITY
IN THERMALLY POLED FUSED SILICA GLASS

by

Thomas Gustave Alley

B.A., Physics, University of Utah, 1984

M.S., Engineering Physics, Air Force Institute of Technology, 1987

Ph.D., Optical Science, University of New Mexico, 1998

ABSTRACT

This study examines the physics underlying the formation of a second-order nonlinearity through thermal poling in bulk fused silica glass. The technique of thermal poling involves applying a large voltage across the glass at an elevated temperature, and then allowing the glass to cool with voltage applied. Nominally, a nonlinearity is created from a high-field space-charge region that forms within ~ 10 μm of the anode surface. This dissertation presents an investigation of the dynamics of the formation of the space-charge region.

In situ experiments are reported that monitor second-harmonic generation and electrical conductivity as the nonlinearity is formed, and as the applied field's polarity is reversed as well as switched on and off. Complex dynamic behavior was observed. Several response time scales were noted. An incubation period of the second harmonic signal occurs until conductivity space-charge relaxation begins. A transient second

harmonic signal from the cathode side was observed after field reversal.

Two microscopic probe techniques are presented that indicate the extent of the nonlinearity in the glass. Poled fused silica samples were usually commercially available flame fused quartz optical flats with ~ 1-5 ppm of various alkali ions and ~ 100 ppm OH. Hydroflouric acid etching was used to etch the cross-section of thin samples. A ridge (indicating an affected region with a slow etch rate) was identified that moved approximately logarithmically deeper into the sample with poling time. A groove (indicating an effected region with a faster etch rate) also was identified for long poling periods (≥ 1 hr). Secondary ion mass spectrometry (SIMS) was used to probe impurity distribution levels under the two electrode surface of poled samples. Regions depleted of Li and Na were observed. Li, Na, K and possibly H were identified as being mobile with different mobilities. Na movement upon field reversal was observed to be hindered by near-surface concentrations of other impurities.

A two-carrier conductivity model is developed, based on very slow ion-exchange from the surface as well as fast movement of a host alkali ion. Although the model only provides a qualitative fit to the experimental trend with poling time because of its necessarily approximate nature and the variability inherent in amorphous samples with varying impurity and water content and preparation histories, this model provides the first explanation of experimental observations such as different response times, an incubation period on field reversal or initial poling, and a second harmonic signal at the cathode. These more complex behaviors were not predicted by the earlier single-carrier model.

TABLE OF CONTENTS

LIST OF FIGURES

LIST OF TABLES

Chapter 1: Introduction and Survey of the Literature

1.1 Introduction

This dissertation is focused on the physics of creating a large, permanent second-order nonlinearity in fused silica glass. The method involves electrically poling glass at an elevated temperature and is thus dubbed "thermal poling". Fused silica glass is amorphous and in the electric dipole approximation the second-order nonlinearity should be zero.[1] So, why glass?

Silica-based glass is ubiquitous. Because of its strong mechanical structure, transparency to visible light, and low-cost manufacturability we find silica glass in everything around us. It is as abundant as our ability to fuse grains of sand. One form is "natural" fused quartz or silica, a noncrystalline, amorphous form of SiO_2, which is made from flame-fusing or electrically-fusing quartz sand or powder. Another form of fused silica is a "synthetic" form which comes from flame-fusing or plasma-fusing of $SiCl_4$. The natural form contains higher levels of intrinsic chemical impurities such as alkali ions and aluminum. Synthetic fused silicas are made from $SiCl_4$, and the resultant impurity levels are much lower.

In the world of optics, we use fused silica for its linear optical properties. Fused silica can be made in bulk, thin films, or fibers. For visible-light wavelengths, fused silica is virtually nonabsorptive for light pathlengths of several centimeters or less. In bulk form, it can be polished and shaped into lenses and windows. Waveguides can be

manufactured from thin silica glass films by various methods and hold promise of integration of optical components into silicon-based microelectronics. Flame fusing manufacturing methods can cause relatively large amounts of hydroxl (OH) through the presence of water vapor. By reducing the amount of hydroxl (OH) content in SiO_2 below one part in 10^7 through alternative manufacturing methods, fused silica glass can be made to show very low loss to infrared wavelengths at 1.3 and 1.55 μm. With the doping of Ge to allow index gradients, this glass is pulled from preforms into optical fibers that form the backbone of modern communication networks. Silica glass towers above all other materials in regards to its linear optical properties.

However, if one were asked to select a material that can frequency-double laser light, or that can be electro-optically controlled to switch or modulate laser light, it would not be surprising to neglect fused silica, or most other glasses for that matter. Normally, one looks for a material with a large second-order nonlinearity, usually expressed through its second-order susceptibility, $\chi^{(2)}$. In order to have a $\chi^{(2)}$, the material's basic structure should be macroscopically asymmetric. The response of an asymmetric structure to an electric field in one direction should be different when compared with another direction. Many crystals have this asymmetry, including fused silica's crystalline cousin, quartz. Glasses, on the other hand, consist of randomly intertwined bonding networks that give an amorphous state. On the macroscopic level of an optical wavelength, averaging over the random structure, glass is centrosymmetric; it looks the same to the incoming light's electric field in every direction (in the dipole approximation). Thus glass has no intrinsic second-order nonlinearity, and $\chi^{(2)}$ reduces to zero. However, fused silica glass can be modified in a manner so as to create such an asymmetry. For example, electrical poling

2

causes an internal electric field to form after application of an external field. If the sample is heated and subsequently cooled with the field applied, the internal field can be "frozen-in". The alignment of the field now leaves an asymmetry in the glass, allowing a second-order nonlinearity.

Silica-based glass optical fibers dominate optical communications. Passive devices such as Bragg grating filters are finding increasing application in telecommunications systems and are particularly important for evolving wavelength division multiplexed (WDM) architectures which allow a multiplication of channels in single fibers. Fiber devices based on creating a second-order nonlinearity might also find widespread application. If the nonlinearity can be made large enough for efficient second-order processes such as frequency-doubling or electro-optic modulation, devices based on this nonlinearity in glass will promptly follow. Active, electrically tunable waveguide and fiber devices based on a second order nonlinearity in SiO_2 would find important systems applications, due to the ease of integration with present silica and silicon-based systems.

1.2 Methods of establishing a second-order nonlinearity in fused silica

The focus of this dissertation is on thermal poling, one of the techniques for creating this nonlinearity. There are alternative methods as well. All the methods can be grouped into two main categories, photoinduced $\chi^{(2)}$ and electric-field induced $\chi^{(2)}$. Thermal poling is electric-field induced.

1.2.1 Photoinduced $\chi^{(2)}$

In 1986, Osterberg and Margulis[2] made the first report of a second-order nonlinearity in glass, discovering the effect quite by accident. They observed frequency doubled light coming from a Ge and P-doped optical fiber after leaving a high intensity infrared laser passing through the fiber for a prolonged period of time. They reported conversion efficiencies into the frequency doubled light as high as 5%. The fiber required ~12 hours of preparation from the infrared "pump" laser for the nonlinearity to grow, and then the frequency doubled or second-harmonic generation (SHG) output power saturated. Later it was found by Stolen and Tom[3] that seeding the fiber with the frequency doubled light along with the fundamental infrared would greatly shorten the length of time (from hours to minutes) required to form the nonlinearity and produce SHG light. Because the coherence length is small (~ 20 μm) in a fiber, the relatively high SHG conversion efficiency requires some sort of phase-matching process. Stolen and Tom proposed that a grating was produced from the periodic arrangement of dipoles from defects in the glass. A number of studies investigated the establishment of this self-organized, photoinduced, second-order nonlinearity. The most widely accepted explanation attributes the nonlinearity to an asymmetric photoionization current that produces a high (10^4 to 10^5 V/cm) dc-electric field with a periodic spatial variation that matches the coherence length.[4-7] According to this theory, the photoionization originates from defect sites from doped (e.g. Ge) materials that provide available states in the band gap for multiphoton ionization Interference between one-photon ionization at ω and two-photon ionization at 2ω causes a periodic photocurrent with a corresponding periodic dc

electric field. This in turn results in a self-organized form of quasi-phase matching by establishing a $\chi^{(2)}$ grating, allowing growth of the SH signal along the path of the optical fiber. The $\chi^{(2)}$ is proportional to the product of the dc electric field and the third order susceptibility ($\chi^{(3)}$) of the glass. The dopant seems to be the key to the photovoltaic effect, and although Ge is the most common dopant, Krol and Simpson[8] showed that introduction of a rare-earth dopant into a aluminosilicate fiber allowed the formation of a $\chi^{(2)}$ grating. The Ge E' defect centers may be the ionized defects in germanosilicate fibers. Tsai *et al.* showed a correlation between the concentration of Ge E' centers and SHG conversion efficiency.[9] Other treatments to increase defects have increased the nonlinearity. Anoikin et al. showed that gamma-irradiation increased the SHG conversion efficiency.[6] Ouellette et al. reported an increase in conversion efficiency by hydrogen and heat treatment.[10] Interestingly, photosensitivity in fibers, which is exploited to make Bragg gratings by refractive index variation in fibers, is also a self-organized photoinduced effect dependent on dopant defect sites and hydrogen treatment[11], suggesting a possible relation to photoinduced $\chi^{(2)}$.

The actual $\chi^{(2)}$ nonlinearity achieved by this effect is quite small (10^{-3} to 10^{-4} pm/V), three or four orders of magnitude smaller than the nonlinearity generated by thermal poling. However, the most efficient method of second harmonic conversion achieved to date in silica glass is photoinduced SHG due its inherent ability to quasi-phase match in the optical fiber, allowing very long interaction lengths.

The discovery of this method to generate a second-order nonlinearity in fused silica created much interest and many investigations were made of this effect in fibers and

other silica based waveguides.[12-14] The periodic dc electric field that causes the nonlinearity has been mapped[15], a non-invasive heat scan technique has been used to study the grating[16], and an acid etching has been used to image the grating[17]. It is interesting to note that a photoinduced $\chi^{(2)}$ can be used to create an optical logic gate switch. A group at the US Air Force Academy showed by selective preparation of different waveguide modes in a planar waveguide with seed and pump beams, that all-optical "AND" and "OR" logic gates could be demonstrated.[18,19]

1.2.2 Electric-field induced $\chi^{(2)}$

Several different methods have been used to electrically-pole silica glass and establish a second-order nonlinearity. Those methods are thermal poling, corona poling, electron implantation, proton implantation, and UV-assisted poling. The number of studies completed in this field is small enough that I have attempted to include all the relevant papers to date of which I am aware.

In 1991 at the University of New Mexico, R.A. Myers *et al.* reported the discovery of the thermal poling method to induce a nonlinearity in fused silica glass.[20] The method typically involves placing fused silica glass between two electrodes, heating the sample to an elevated temperature between 250 and 300 °C, and applying a high voltage (1000's of Volts). The sample is then allowed to cool with the voltage still applied. This method was used to create a $\chi^{(2)}$ as high as ~1 pm/V, which is 3 to 4 orders of magnitude larger than that reported in silica based fibers with photoinduced $\chi^{(2)}$.

There have been several related methods that have produced second order nonlinearities on the order of 1 pm/V as well. A group from Keio University in Japan used corona poling to create a $\chi^{(2)}$ in Corning 7059 (barium borosilicate) films on soda-lime or pyrex substrates at temperatures between 20 to 100 °C.[21-24] The poling was done for a long poling period (e.g. 12 hours). Corona uses a pointed electrode held near the sample surface and is often used to orient organic molecules in thin films. The tip does not need to touch the surface, thus eliminating any damage that might occur when attempting to pole a soft surface. The result is essentially the same as other electric-field poling methods; an electric field from the electrode polarizes the material. It is highlighted as a different method than thermal poling here because studies were done in a lower temperature regime, with varying types of glass films and substrates. One study, using x-ray photoelectron spectroscopy, showed a buildup of sodium at the cathodic surface of the film.[23] They attributed the nonlinearity to a sodium depletion region at the anode. The Japanese group also observed a decay in the second-order nonlinearity induced in corona poled thin films.[24] The nonlinearity had a fast decay within several thousand minutes, followed by a slower decay over several ten thousand minutes. The lack of long term stability does not bode well for this technique if practical devices or components are to be constructed.

A group at the University of Southhampton in England showed that a second harmonic signal could be obtained by electron beam exposure in lead-silicate glasses.[25] The most successful results were found in samples of doped lead-silicate glass (Pb ~ 40 wt%, plus several wt% of Ce and TiO_2).[26] The glass was exposed in a scanning electron

microscope to electron-beam currents in the range 0.3 nA to 10 nA, beam voltages between 5 kV and 40 kV, and spot size of 0.5 μm. Using an interaction length of 7 μm, a $\chi^{(2)}$ value of 0.7 pm/V was calculated. Other glasses were tried as well. This technique did not work in fused silica glass, but was useful in erasing the $\chi^{(2)}$ in thermally poled silica.[27] Doped silica glasses also produced a measurable $\chi^{(2)}$ with electron-beam exposure, with albeit at lesser values compared with the doped lead-silicate glass. Ge-doped silica showed 0.25 $\chi^{(2)}$(doped lead glass), Nb-doped silica showed 0.1 $\chi^{(2)}$(doped lead glass), and Ti+Zr-doped silica showed 0.1 $\chi^{(2)}$(doped lead glass). Lead-germanate glass, showed 0.01 $\chi^{(2)}$(doped lead glass), while phosphate glass, showed <0.01$\chi^{(2)}$(doped lead glass).

One further technique is the implantation of protons as reported by a group at the US Air Force Academy,[28] who showed that a large nonlinearity (~1 pm/V) could be established through irradiation of accelerated protons in type I (low water) and type II (high water) natural fused silica, with the largest $\chi^{(2)}$ in type I. Isolated regions in the type I fused silica showed $\chi^{(2)}$ as high as 1.6 pm/V. A type III (high water) synthetic fused silica showed a smaller $\chi^{(2)}$ (~ 0.05 pm/V). Beam energies from 250 to 800 keV and charge dosages from 0.25 to 3.25 mC were studied. A minimum dosage of 0.25-0.5 mC and a minimum irradiation time of 10-15 s was necessary for a large $\chi^{(2)}$. For purposes of calculating a $\chi^{(2)}$ value, a nonlinear depth of 10 μm was used.

A UV-excited poling technique has generated a great deal of curiosity and interest. In 1995, an Australian group at the University of Sydney led by T. Fujiwara[29,30], reported inducing an electrooptic coefficient of ~6 pm/V (equivalent to a $\chi^{(2)}$ of ~ 14

pm/V if the effect is due to electronic motion only) in a specially prepared fiber with electrode wires placed in holes parallel to the fiber core, with the core in-between the holes and the holes approximately 10 μm apart. To form the nonlinearity, a voltage of 800 V was applied across the wires while the fiber was irradiated with UV light from a pulsed ArF excimer laser at 193 nm. The energy density of the laser was 36 mJ/cm^2, pulse repetiton rate of 10 pps, and fibers were irradiated for 1 to 10 min. The nonlinearity was observed by measurements of the electrooptic phase shift. The large value for the nonlinearity is a factor of 10 higher than reported for any other poling processes and is sufficient to make efficient devices in silica-based fibers a reality.

Other groups have not been able to repeat Fujiwara et al.'s result. For example, Kazansky and Pruneri attempted the experiment and estimated the amplitude of the second-order susceptibility to be $\chi^{(2)} \sim 0.01$ pm/V.[31,75] Kazansky and Pruneri also explained UV-assisted poling in terms of a electrically stimulated coherent photoconductivity. The basic phenomenon was modeled by a process similar to photoinduced SHG where the nonlinearity is created by interference of one photon ionization at ω and two photon ionization at 2ω and there is no external applied electric field. When an electric field is applied, there is still interference of light fields at ω and 2ω, and consequently, an interference in the probability of photoionization of defect sites. The modulated terms in this photoionization interference lead to a corresponding modulation of the photoconductivity. The internal electric field which reacts to screen the applied electric field now has an additional term (E_{coh}) caused by and proportional to the modulated part of the photoconductivity (the coherent photoconductivity). The

modulation of the internal field due to E_{coh} was estimated by Kazansky and Pruneri to be ~ 8 % of the applied electric field and like photoinduced $\chi^{(2)}$ leads to a quasi-phase matched $\chi^{(2)} = 3\chi^{(3)}E_{coh}$. Compared to photoinduced $\chi^{(2)}$, the modulated electric field is enhanced by the presence of an externally applied electric field.

Fujiwara continued to repeat and report new results with this technique. A Japanese group including Fujiwara at the Toyota Technological Institute reported UV-excited poling and its effect on SHG in a bulk Ge-doped SiO_2 glass, using electrodes placed in grooves 1 mm apart and the application of an electric field of 1 x 10^4 to 3 x 10^5 V/cm.[32] The glass was simultaneously irradiated with 193 nm eximer laser radiation with an energy density of 100 mJ/cm^2, pulse repetition rate of 10 pps, and a total number of 10^4 shots. The induced nonlinearity saturated at ~ 1.5 x 10^5 V/cm, and they measured a maximum coefficient of $\chi^{(2)}_{33}$ ~ 6.8 pm/V ($\chi^{(2)}_{31}$ ~ 2.2 pm/V). They also observed an anisotropy in refractive index, with a corresponding polarization dependence of the induced SHG, which increased with increasing electric field strength. As the field was increased, an increase and decrease in the index of refraction was observed for the extraordinary and ordinary polarizations, respectively. The group also studied Ge-related defects induced by the UV irradiation.[33] They proposed that the UV-excited poling produces Ge electron-trapped centers which then convert to Ge E' centers (observed peak absorption at 6.3 eV), implying a correlation between the nonlinearity and the Ge E' centers. They reported a measurement of the Ge E' defect concentration with increasing electric field, which like the nonlinearity, saturated at ~ 1.5 x 10^5 V/cm at a concentration of ~ 4 x 10^{17} cm^{-3}. The defect concentration was reported to be in the vicinity of the UV-

irradiated surface within a depth defined by $L_e = \eta L$ where η is a correction factor taking into account the absorption coefficient (45 cm^{-1}) at 193 nm and L is the width of the sample (1 mm). L_e works out to be 220 μm. It should be mentioned that a large concentration of defects would be required if the nonlinearity is attributed to an orientation mechanism, and a reasonable hyperpolarizability (e.g. $\beta \sim 10^{-38}$ m^4/V for p-nitroaniline polymer[34]) is assumed.

Fujiwara *et al.* also made quantitative decay measurements at various temperatures to study the long-term behavior of the UV-excited poling nonlinearity.[35] They found that the decay is a single-exponential process with a decay time constant at 15°C of ~ 280 days. If UV-excited poling proves reproducible, a limiting factor for device application may prove to be its long-term decay.

1.2.3 Thermal Poling

1.2.3.1 Formation of the nonlinearity by thermal poling

Thermal poling so far has proven to be the most stable poling technique for inducing a $\chi^{(2)}$ in fused silica. Although no long-term systematic study has been done, samples that have been stored for years without special precautions at room temperature have shown no appreciable decay. A group in Japan[64] extrapolated Arrhenius temperature behavior of poled fused silica glass and estimated a room temperature lifetime of 720 years. This stability makes the application of the nonlinearity viable. The technique is simple and a nonlinearity is easily producible. It has been investigated by

quite a few groups[36,37], yet there is still much to understand, especially regarding the mechanism leading to the formation of the nonlinearity.

The nonlinearity is observed to form in a near-surface region under the positive electrode (anode).[20] The initial measurements showed a nonlinear region that was ≤ 4 µm thick, determined from Maker fringe scans and HF etching of 1.6-mm thick fused silica samples nominally poled for 15 minutes. Several experiments have provided additional information on the location of the nonlinearity and a space charge region associated with the nonlinearity. For example, Kazansky and Russell used a focused laser to probe the nonlinear layer transverse to the poling direction and observed the nonlinearity to be peaked 12 µm below the anode surface with a 7-µm spatial extent.[38] Kazansky *et al.* later measured charge distributions in thermally poled silica glass via a laser induced pressure pulse probe (LIPP) technique.[39] They found regions of alternating charge at the anode and postulated the formation of real space charge layers and dipole polarization. In Rio de Janeiro, Margulis *et al.*,[40] using a hydroflouric (HF) acid etching technique, measured the regions of glass affected by the poling process by monitoring etch rates. For a long poling time of 225 min., they found a 5.5-µm deep region which they associated with negative charge, as well as a region out to 34 µm that they associated with a weak excess of positive charge. Myers found that long poling times extended the space charge region further into the glass.[19,41] By repeated etching of the surface of poled samples, followed by SH measurement, he found that the depth of the nonlinearity is deeper for a sample poled for 2 hours compared to one poled for 15 minutes. Also, by observing Maker fringes, he showed that the nonlinear region extended deeply enough into the sample to result in destructive interference for samples poled for long periods when a fundamental

12

beam at $\lambda = 532$ nm was used (the coherence length for doubling 532 nm radiation in fused silica is approximately 3 μm). Pureur *et al.* from Stanford University have recently found, using a prism-assisted Maker-fringe technique, that the peak of the nonlinearity is located below the anode surface with its depth determined by poling temperature and voltage.[42] Liu *et al.*,[43] again from Stanford, reported that the strength and depth of the nonlinearity can be slightly improved by poling at temperatures higher than 275 °C and voltages higher than 5 kV, contrary to other observations[20,51].

In contrast to the previously mentioned findings, three groups, one at Mie University, Japan[44], a second at the USAF Academy[45], and a third in Shanghai, China[46] reported Maker fringe patterns (at least in certain circumstances) in bulk thermally poled fused silica which matched that expected for a nonlinearity spread through the full bulk width. The groups interpret their results to indicate that the nonlinearity can exist throughout the bulk and the level of OH or defects associated with the loss of H are associated with it. The second group offered that the nonlinearity could alternatively be interpreted to exist in two regions, one at the anode and the other at the cathode. Recently, a group in France reported an experiment that measured SH signals generated in reflection only from the surfaces of the fused silica samples.[47] They were able to detect SH signal generated in reflection from both the cathodic and anodic surfaces, and attributed it to reorientable moieties.

A few ideas regarding the origin of the nonlinearity have been offered. In all of the proposed models, a large electric field is established in the glass. Myers *et al.* first proposed that the nonlinearity arises from the movement of ionic carriers at an elevated temperature, exposing an immobile space charge, and the subsequent trapping of the

carriers by cooling the sample.[20,48] There is general agreement that ionic motion is involved in the formation of the nonlinearity. A collaboration between a group at Kyushu University, Japan and the University of Southhampton reported on the effect of impurities on thermal poling.[49] They concluded from measurement of OH and Na levels as well as the electrical current level during the poling process, that Na impurities play a key role. Once the ionic impurities have moved, a dc electric field, E_{dc}, must exist from Poisson's equation. The second-order nonlinearity can then exist through an effective $\chi^{(2)}$ through the relationship $\chi_{eff}^{(2)} = 3\chi^{(3)} E_{dc}$, where $\chi^{(3)}$ is the inherent third-order nonlinearity in the glass. Our group also proposed that the nonlinearity might be caused by orientation of dipoles instead of or in addition to the $\chi^{(3)} E_{dc}$ effect.[20,50] In the case of dipole orientation, the $\chi^{(2)}$ is also proportional to E_{dc}. Kazansky and Russell argued that $\chi^{(3)} E_{dc}$ appeared sufficient to explain the level of nonlinearity, but that dipole orientation cannot be ruled out.[48] Liu et al.[51] from Stanford University measured the DC Kerr $\chi^{(3)}$ in a SiO_2-GeO_2 channel waveguide finding $\chi_{1111}^{(3)} = 2.44 \times 10^{-22}$ m^2/V^2, as well as a ratio of $\chi_{1111}^{(3)} = 1.1\chi_{1122}^{(3)}$. They reasoned that only in the best possible poling scenario could the magnitude of the $\chi^{(3)}$ explain the measured values in Ge-doped silica glass of $\chi^{(2)}$ through the relationship $\chi^{(2)} = 3\chi^{(3)}E_{dc}$. They also reasoned that this was not likely.

Kazansky and Russell[48] also measured the sign of charge layer at the anodic surface and found that for samples poled at temperatures below 230 °C, the surface was negatively charged, whereas the anodic surface of samples poled at 280 °C were electrically neutral. They suggested that high-field ionization occurs in the large electric field, neutralizing the negative charge region near the surface. The Brazilian group also

showed that HF etch rates in glass can be affected by applied electric fields.[52] They

proposed that the etch rates of ref. [40] could be explained by orientation of HF

molecules in the liquid etchant from the high frozen-in electric field at the poled glass

surface.

Based on the observation of dynamic behaviors not described by a single ionic

carrier/space charge theory, our group has recently proposed adjusting the theory to

include ion exchange of hydrogen at the surface; allowing an additional slow charge

carrier to move into the space charge region.[53-55] This model will be covered in detail in

chapter 5. At the University of Southhampton, Takebe et al.[56] showed that the poling

atmosphere, as well as poling history, has a significant effect on the level of SH signal

observed in treated samples.

Other types of silicate glass besides "natural" fused silica (fused quartz) have been

shown to develop a second-order nonlinearity when thermally poled. A Japanese group

showed that Ti-doped and Ga-doped silica glasses could produce a second-order

nonlinearity through thermal poling.[57,58] The Brazilian group recently showed that "soft"

glasses, i.e. those rich in alkali ions such as soda-lime glass or borosilicate glass, can also

be thermally poled.[59] The disadvantage of soft glasses is that the nonlinearity decays by

an order of magnitude in times as short as an hour.

Investigations of thermal poling of "synthetic" fused silica have been reported.

Synthetic fused silica is formed from either flame-fusing ("wet"- large OH concentration)

or plasma-fusing ("dry"- low OH concentration) $SiCl_4$, forming a fused silica with low

impurity levels. A Japanese group found that a small nonlinearity ($\chi^{(2)} \sim 0.02$ pm/V) can

be produced in "wet" (high OH) synthetic fused silica from thermal poling and that a dose of γ-rays from ^{60}Co prior to thermal poling can double the nonlinearity through the creation of defects.[60] The nonlinearity thickness used for $\chi^{(2)}$ calculation was not given. A collaboration between groups at Miyazaki University, Japan and the University of Toronto, Canada showed that creation of defects from x-rays could also enhance the nonlinearity in both wet and dry synthetic fused silicas.[61] No signal was observed in unirradiated samples, but estimates for the nonlinear susceptibilities were $\chi^{(2)} \sim 0.24$ pm/V for the wet synthetic fused silica and ~ 0.11 pm/V for the dry synthetic fused silica. The assumed thickness of the nonlinear region used in the estimate was 22 μm, because no fringes were observed in a Maker fringe experiment and 22 μm was the assumed coherence length. A shorter estimate (e.g. 7-10 μm) of the nonlinear depth would boost the $\chi^{(2)}$ values by 2 to 3. Our group found that the SH signal in "wet" synthetic fused silica (Suprasil) is about 10 % that in natural fused silica.[20] However, after heating a sample to 800 °C, then cooling it to room temperature, followed by standard thermal poling, the SH signal was equivalent to that of natural fused silica.[36] A measurement of photoluminescence (PL) at 1.9 eV (associated with non-bridging oxygen hole centers) showed a large increase as a result of the heat treatment.[41]

Different types of silica films have been studied. A Japanese group at Shizuoka University showed that a sol-gel derived glass film as well as rf-sputtered germanosilicate films on silica substrate can be thermally poled.[62-64] Adding large concentrations of GeO_2 or TiO_2 enhanced the nonlinearity. A 0.1-μm thick sol-gel film with a large GeO_2 concentration (30 wt%) was reported to have a $\chi_{33}^{(2)}$ as high as 15 x $\chi_{11}^{(2)}$ for quartz

$(\chi^{(2)}_{11} = 0.8$ pm/V). This put the $\chi^{(2)}$ at 12 pm/V! However, a subsequent report[64] revises

this estimate to a still relatively large 3.4 pm/V. This $\chi^{(2)}_{33}$ value was for a film on a pyrex

substrate, which subsequently decayed to 10% of its value after 100 h. When the thin

film was on a silica glass substrate, the value of the nonlinearity was reported as high as

$\chi^{(2)} \sim 0.4$ pm/V, with a lifetime estimate of 1-2 years. For the rf sputtered germanosilicate

films, an average value of $\chi^{(2)}_{33}$ over a 1.53 µm thick film was given as 1.6 pm/V and the

exponential lifetime of the nonlinearity was extrapolated to be 310 years for a sample

with a silica substrate (The article contains a contradiction about which substrate

corresponds to this lifetime measurement. In the text it says pyrex and in a figure it says

silica. After checking a cited reference[21] in the article it becomes clear that the long

lifetime corresponds to the silica substrate). They also reported by etching the film that

the $\chi^{(2)}$ peaked at a value of 6.8 pm/V approximately 0.3 µm under the surface and

diminished deeper into the material. They concluded that the interface plays a large role

in forming a space charge region and affects the nonlinearity. If the substrate used for

thin films was pyrex or a microscope slide (soda-lime glass), a depletion layer would

form in the substrate at the interface and enhance the nonlinearity in the films. Note that

Horinouchi et al.[23] also reported that the nonlinearity was located at the interface between

a corona-poled thin film and its pyrex substrate. A disadvantage of using these pyrex or

soda-lime substrates is their limited lifetimes.

Thermal poling of Ge-doped flame-hydrolysis SiO_2 films deposited on Si was

studied by our group.[65] The effect of hydrogen loading on the films was also studied and

was shown to increase the SH signal under certain conditions.[66] A $\chi^{(2)} \sim 0.4$ pm/V was measured in several films, while others required a high temperature heat treatment in an H_2 ambient before producing a nonlinearity. In a Ge-doped thin film waveguide stack a nonlinearity was measured and was found to be in the lower cladding layer and core, peaking in the lower cladding layer, with the interface between layers acting as charge trapping sites, similar to the conlusion reached by the Shizuoka University group. Another interesting observation made with the waveguide stack was that the optimum poling temperature was ~ 150 °C, which is ~ 100 °C less than the best poling temperature for bulk fused silica. Based on temporal studies on the thin films, Myers[41] concluded that the process of formation in the films was different than that in the bulk. Because of an assumed lack of a depletion layer, he reasoned that fast SHG responses to turning on and off the applied field were due a $\chi^{(3)}E_{dc}$ mechanism alone and slow SHG responses were possibly due to a dipole orientation mechanism. He found that the slow SHG response became more prevalent with increased hydrogen loading, thus increasing the contribution of dipole orientation to the nonlinearity.

Fibers and fiber preforms were thermally poled and investigated by Kazansky *et al.*[67] They found that Ge-doping, in combination with OH doping, enhanced the nonlinearity and that the SH signal in the core of the preform followed the Ge concentration. The value of 0.2 pm/V was given for the $\chi^{(2)}$ for the core of the preform.

1.2.3.2 Applications of thermal poling

Presently there are two main directions regarding device applications of the second-order nonlinearity in fused silica: quasi-phase matched (QPM) frequency doubling and the electrooptic effect.

The application of an external field through periodic electrodes to induce QPM second harmonic light has been studied in various ways. By using interdigitated electrodes to pole germanosilicate fibers, electric field-induced quasi-phase matching was reported as early as 1989 by Kashyap.[68] Weitsman et al.[69] demonstrated quasi-phase matching in planar germanosilicate waveguides. The electric field poling from both of these studies were not at elevated temperatures. The first demonstration of quasi-phase matching by periodic *thermal* poling was reported by Kashyap et al.[70] in bulk fused silica. A low effective nonlinearity was estimated at $\chi_{11}^{(2)}$/200 of quartz, due to a non-optimized grating with small modulation and a small induced nonlinearity amplitude. Germanosilicate glass waveguides were thermally poled with removable interdigitated electrodes and quasi-phase matched second harmonic light was produced by Statman and Georges.[71] Exponential decay on the order of minutes was observed upon removal of electrodes after cooling. The group at the University of Southampton has performed several studies on the periodic poling of fibers.[72-76] Fibers were periodically poled by applying a high voltage at an elevated temperature to deposited electrodes on the flat side of a D-shaped fiber. The poling was accomplished *in vacuo* to minimize the unwanted spreading of the electric field. The nonlinearity was shown to be approximately 1.4 pm/V, however the structure of the grating that forms was nonuniform leading to a small

conversion efficiency (average of ~0.22%) when ~ 422 nm second harmonic light was generated. By far the most efficient frequency doubling to date in a thermally poled fiber was that done by Pruneri et al.[76] at the University of Southampton. Using $\lambda = 1.5 \ \mu m$ femtosecond laser pulses in a D fiber having a 4-cm long grating with a period of 57.15 μm, an average conversion efficiency of ~1.2% was obtained using thermal poling in a high vacuum at 5 kV and 275 °C. The effective nonlinearity was still 5-10 times below the theoretical value estimated from measurements on uniformly poled fibers indicating continuing problems with uniformity.

Measurements of the piezoelectric effect and electro-optic effect caused by the second-order nonlinearity in thermally poled fused silica were first reported by our group in 1994.[65,77,78] In bulk fused silica, the linear electrooptic coefficient r_{33} was found to be 0.3 pm/V. This corresponds to a $\chi^{(2)} \sim 0.8$ pm/V $(r = 2 \ \chi^{(2)} / n^4)$, assuming that the effect is due solely to electronic motion. In a segment of fiber poled on a bulk silica substrate the electrooptic coefficient was found to be $r \sim 0.05$ pm/V. Kazansky et al. found similar results in thermally poled optical fibers.[79,80] Liu et al.[81] from Stanford University demonstrated the electrooptic effect in a thermally poled channel waveguide observing a 32 mrad phase shift in a waveguide 4.8-mm long. With changes to the fiber poling arrangement, our group showed an improved electrooptic coefficient of r ~ 0.3 pm/V.[82] An electrooptic switch was demonstrated by Abe et al.[83] in a germanium doped silica-based waveguide on Si with an estimated electrooptic coefficient of 0.02 pm/V. The switch was based on a Mach-Zehnder interferometer structure and operation of the switch required a drive voltage of 1700 V. Carvalho et al.[84] reported a procedure to pole

microfibers (to exploit the electro-optic effect) which involves etching an optical fiber to its core before poling. Electrooptic modulation was observed, but quantitative measurements have not yet been published. Further improvements of fiber poling by our group led to a measurement of a π phase shift over a 12 cm active fiber region using a drive voltage of only 75 V.[85] The poled fiber showed good thermal stability, with no decay for over 4 months at room temperature and less than a 10% decay when heated to 90 °C for 1000 hours (3 months). This is in contrast to a ~ 280 day 1/e decay at 15 °C reported[35] for UV poled germanosilicate glass as mentioned in section 1.2.2.

1.3 Present work and outline

This dissertation presents work on the physics of the formation of the space-charge region that gives rise to the second-order nonlinearity in bulk fused silica. It is hoped that a better understanding of processes in bulk glass will help our understanding of the nonlinearity in thin films and fibers as well, so that better engineering of devices based on silica materials will result.

There are 5 chapters including the present one. Chapter one gives an introduction and survey of the literature. Because the field is still relatively small, I attempted to include all the relevant literature of which I am aware on the topic of electric-field induced $\chi^{(2)}$ in silica glass. The second chapter provides a background on nonlinear optics and the second-order nonlinearity, as well as relevant background information on silica glass, such as types, impurities and defects, conduction and poling, etc. Chapter three presents experimental data. It includes measurements of second-harmonic

generation and conductivity in bulk fused silica as the nonlinearity and its associated space-charge region forms. Two microscopic probe techniques are presented that indicate the extent of the nonlinearity in the glass. Hydroflouric acid etching was used to etch the cross-section of thin samples. Secondary ion mass spectrometry (SIMS) was used to probe impurity distribution levels under the two electrode surface of poled samples. These are the first microscopic measurements of the frequency-doubling space charge region in fused silica. The fourth chapter discusses our present model and theory on how the space-charge region forms, and how it is supported by the experimental data. Modeling is shown via numerical simulation. This model provides the first explanation of experimental observations such as different response times, an incubation period on field reversal or initial poling, and a second harmonic signal at the cathode. These more complex behaviors were not predicted by the earlier single-carrier model. Finally, Chapter five summarizes the previous chapters and gives suggested future directions.

1.4 References

[1] N. Bloembergen, *Nonlinear Optics*, 4th ed. (World Scientific Publishing, Singapore, 1996).

[2] U. Osterberg and W. Margulis, "Dye laser pumped by Nd:YAG laser pulses frequency doubled in glass optical fiber," Opt. Lett. **11**, 516 (1986).

[3] R.H. Stolen and H.W.K. Tom, "Self-organized harmonic generation in optical fibers," Opt. Lett. **12**, 585 (1987).

[4] B.Ya. Zel'dovich and A.N. Chudinov, "Interference of fields with frequencies ω and 2ω in external photoelectric effect," JETP Lett. **50**, 439 (1989).

[5] E.M. Dianov, P.G. Kazansky, and D.Yu. Steponov, "Problem of the photoinduced second harmonic generation," Sov. J. Quantum Electron. **19**, 575 (1989).

[6] E.V. Anoikin, E.M. Dianov, P.G. Kazansky, and D.Yu. Stepanov, "Photoinduced second harmonic generation in gamma-ray-irradiated optical fibers," Opt. Lett. **15**, 834 (1990).

[7] D. Anderson, V. Mizrahi, and J.E. Sipe, "Model for second-harmonic generation in glass optical fibers based on asymmetric photoelectron emission from defect sites," Opt. Lett. **16**, 796 (1991).

[8] D.M. Krol and J.R. Simpson, "Photoinduced second-harmonic generation in rare-earth-doped aluminosilicate fibers," Opt. Lett. **16**, 1650 (1991).

[9] T.E. Tsai, M.A. Saifi, E.J. Friebele, D.L. Griscom, and U. Osterberg, "Correlation of defect centers with second-harmonic generation in Ge-doped and Ge-P doped silica-core single-mode fibers," Opt. Lett. **14**, 1023 (1989).

[10] F. Ouellette, K.O. Hill, and D.C. Johnson, "Enhancement of second-harmonic generation in optical fibers by a hydrogen and heat treatment," Appl. Phys. Lett. **54**, 1086 (1989).

[11] V.B. Neustruev, "Colour centres in germanosilicate glass and optical fibers," J. Phys.: Condens. Matter **6**, 6901 (1994).

[12] Yu. V. Glushchenko and V.B. Smirnov, "Photoinduced second-harmonic generation in glass-fiber lightguides: a review," Opt. Spectrosc. **72**, 538 (1992).

[13] R. Kashyap, B.J. Ainslie, and G.D. Maxwell, "Second harmonic generation in GeO_2 ridge waveguide," Electron. Lett. **25**, 206 (1989)

[14] J.J. Kester, P.J. Wolf, and W.R. White, "Second-harmonic generation in planar waveguides of doped silica," Opt. Lett. **17**, 1779 (1992).

[15] V. Dominic and J. Feinberg, "Spatial shape of the dc electric field produced by intense light in glass," Opt. Lett. **18**, 784 (1993).

[16] W. Margulis, I.C.S. Carvalho, P.M.P. Gouvea, and B. Lesche, "Heat scan: a simple technique to study gratings in fibers," Opt. Lett. **18**, 1016 (1993).

[17] W. Margulis, F. Laurell, and B. Lesche, "Imaging the nonlinear grating in frequency-doubling glass fibers," Nature **348**, 699 (1995).

[18] P.M. Ranon, I. Dajani, J.J. Kester, and T.G. Alley, "All-optical programmable AND gate implementation in a germanium-doped silica planar waveguide," Appl. Phys. Lett. **67**, 3532 (1995).

[19] P.M. Ranon, I. Dajani, D.C. Kopf, T.G. Alley, W.R. White, and J.J. Kester, "Planar geometry thin-film all-optical programmable switch," Appl. Opt. **35**, 6390 (1996).

[20] R.A. Myers, N. Mukherjee and S.R.J. Brueck, "Large second-order nonlinearity in poled fused silica," Opt. Lett., **16**, 1732 (1991).

[21] A. Okada, K. Ishii, K. Mito, and K. Sasaki, "Phase-matched second-harmonic generation in novel corona poled glass waveguides," Appl. Phys. Lett. **60**, 2853 (1992).

[22] A. Okada, K. Ishii, K. Mito, and K. Sasaki, "Second-order nonlinearity in corona-poled glass films," J. Appl. Phys. **74**, 531 (1993).

[23] S. Horinouchi, H. Imai, G.J. Zhang, K. Mito, and K. Sasaki, "Optical quadratic nonlinearity in multilayer corona-poled glass films," Appl. Phys. Lett. **68**, 3552 (1996).

[24] H. Imai, S. Horinouchi, Y. Uchida, H. Yamasaki, K. Fukao, G. Zhang, T. Kinoshita, K. Mito, H. Hirashima, and K. Sasaki, "Time-dependent decay of quadratic non-linearity in corona-poled silicate glass films," J. Non-Cryst. Solids **196**, 63 (1996).

[25] P.G. Kazansky, A. Kamal, and P.St.J. Russell, "High second-order nonlinearities induced in lead silicate glass by electron-beam irradiation," Opt. Lett. **18**, 693 (1993).

[26] P.St.J. Russell, P.G. Kazansky, and A. Kamal, "Electron implantation - A new technique for creation and modification of second-order susceptibility in glasses," in *Photosensitivity and Self-organization in Optical Fibres and Waveguides*, F. Oullette ed., Proc. SPIE **2044**, 192 (1993).

[27] P.G. Kazansky, A. Kamal, and P.St.J. Russell, "Erasure of thermally poled second order nonlinearity in fused silica by electron implantation," Opt. Lett. **18**, 1141 (1993).

[28] L.J. Henry, B.V. McGrath, T.G. Alley, and J.J. Kester, "Optical nonlinearity in fused silica by proton implantation," J. Opt. Soc. Am. B **13**, 827 (1996).

[29] T. Fujiwara, D. Wong, Y. Zhao, S. Fleming, S. Poole, and M. Sceats, "Electro-optic modulation in germanosilicate fiber with UV-excited poling," Electron. Lett. **31**, 573 (1995).

[30] T. Fujiwara, D. Wong, Y. Zhao, S. Fleming, V. Grishina, and S. Poole,"UV-excited poling and electrically tunable bragg gratings in a germanosilicate fiber," *Technical Digest of OFC*, San Diego, CA, paper PD-6 (1995).

[31] P.G. Kazansky and V. Pruneri, "Electrically stimulated light-induced second-harmonic generation in glass: Evidence of coherent photoconductivity," Phys. Rev. Lett. **78**, 2956 (1997).

[32] T. Fujiwara, M. Takahashi, and A.J. Ikushima, "Second-harmonic generation in germanosilicate glass poled with ArF laser irradiation," Appl. Phys. Lett. **71**, 1032 (1997).

[33] M. Takahashi, T. Fujiwara, T. Kawachi, and A.J. Ikushima, "Defect formation in GeO_2-SiO_2 glass by poling with ArF laser excitation," Appl. Phys. Lett. **71**, 993 (1997).

[34] M. Eich, A. Sen, H. Looser, G.C. Bjorklund, J.D. Swalen, R. Twieg, and D.Y. Yoon, "Corona poling and real-time second-harmonic generation study of a novel covalently functionalized amorphous nonlinear optical polymer," J. Appl. Phys. **66**, 6 (1989).

[35] T. Fujiwara, M. Takahashi, and A.J. Ikushima, "Decay behaviour of second-order nonlinearity in GeO_2-SiO_2 glass poled with UV-irradiation," Electron. Lett. **33**, 980 (1997).

[36] R.A. Myers, X. Long, and S.R.J. Brueck, "Recent advances in the second-order nonlinear optical properties of amorphous silica materials," in *Doped Fiber Devices and Systems*, Proc. M.J.F. Digonnet, ed., SPIE **2289**, 185 (1994).

[37] P.G. Kazansky, P.St.J. Russell, and H. Takebe, "Glass fiber poling and applications," J. Lightwave Tech. **15**, 1484 (1997).

[38] P.G. Kazansky, A. Kamal and P.St.J. Russell, "Erasure of thermally poled second-order nonlinearity in fused silica by electron implantation," Optics Lett., **18**, 1141 (1993).

[39] P.G. Kazansky, A.R. Smith, P.St.J. Russell, G.M. Yang, and G.M. Sessler, "Thermally poled silica glass: Laser-induced pressure pulse probe of charge-distribution," Appl. Phys. Lett. **68**, 269 (1996).

[40] W. Margulis and F. Laurell, "Interferometric study of poled glass under etching," Opt. Lett **21**, 1786 (1996).

[41] R.A. Myers, *Large Second-Order Nonlinearity in Amorphous SiO_2 Using Temperature/Electric-Field Poling*, Ph.D. Dissertation, University of New Mexico (1995).

[42] D. Pureur, A.C. Liu, M.J.F. Digonnet, and G.S. Kino, "Absolute prism-assisted maker fringe measurements of the nonlinear profile in thermally poled silica," in *Bragg Gratings, Photosensitivity, and Poling in Glass Fibers and Waveguides: Applications and Fundamentals*, OSA Technical Digest Series Vol. **17**, 299 (1997).

[43] A.C. Liu, D. Pureur, M.J.F. Digonnet, G.S. Kino, and E.J. Knystautas, "Improving the nonlinearity of silica at higher temperatures and voltage," in *Bragg Gratings, Photosensitivity, and Poling in Glass Fibers and Waveguides: Applications and Fundamentals*, OSA Technical Digest Series Vol. **17**, 302 (1997).

[44] H. Nasu, H. Okamoto, A. Mito, J. Matsuoka, and K. Kamiya, "Influence of the OH content on second harmonic generation from electrically polarized SiO_2 glasses," Jpn. J. Appl. Phys. **32**, L406, (1993).

25

[45] L.J. Henry, A.D. DeVilbiss, and T.E. Tsai, "Effect of preannealing on the level of second-harmonic generation and defect sites achieved in poled low-water fused silica," J. Opt. Soc. Am. B **12**, 2037, (1995).

[46] J. Xu, X. Lu, H. Chen, L. Liu, W. Wang, C. Zhu, and F. Gan, "Second harmonic generation investigation on electric poling effects in fused silica," Opt. Materials **8**, 243 (1997).

[47] A. Le Calvez, E. Freysz, and A. Ducasse, "Experimental study of the origin of the second-order nonlinearities induced in thermally-poled fused silica," Opt. Lett. **22**, 1547 (1997).

[48] P.G. Kazansky and P.St.J. Russell, "Thermally poled glass: frozen-in electric field or oriented dipoles?," Opt. Commun. **110**, 611 (1994).

[49] N. Wada, K. Morinaga, H. Takebe, V. Pruneri, and P.G. Kazansky, "Effect of minority species on thermal poling of fused silica glasses," in *Bragg Gratings, Photosensitivity, and Poling in Glass Fibers and Waveguides: Applications and Fundamentals*, OSA Technical Digest Series Vol. **17**, 296 (1997).

[50] N. Mukherjee, R.A. Myers and S.R.J. Brueck, "Dynamics of second harmonic generation in fused silica," J. Opt. Soc. Am. B **11**, 665 (1994).

[51] A.C. Liu, M.J.F. Digonnet, and G.S. Kino, "A DC Kerr measurement in a silica channel waveguide," in: *Doped Fiber Devices*, M.J.F. Digonnet and F. Ouellette, eds., SPIE Proc. Vol. **2841**, 209 (1996).

[52] B. Lesche, F.C. Garcia, E.N. Hering, W. Margulis, I.C.S. Carvalho, and F. Laurell, "Etching of silica glass under electric fields," Phys. Rev. Lett. **78**, 2172 (1997).

[53] T.G. Alley, R.A. Myers and S.R.J. Brueck, "Temporal response of the second-order nonlinearity in poled bulk-fused silica under field reversal," in: *Doped Fiber Devices*, M.J.F. Digonnet and F. Ouellette, eds., SPIE Proc. Vol. **2841**, 202 (1996).

[54] T.G. Alley, S.R.J. Brueck and R.A. Myers, "An ion exchange model for extended-duration thermal poling of bulk fused silica," in: *Bragg Gratings, Photosensitivity, and Poling in Glass Fibers and Waveguides: Applications and Fundamentals*, OSA Technical Digest Series Vol. **17**, 293 (1997).

[55] T.G. Alley, S.R.J. Brueck, and R.A. Myers, "Thermal poling and space charge dynamics including surface hydrogen injection in fused silica," submitted to J. Non-Cryst. Solids

[56] H. Takebe, P.G. Kazansky, P.St.J. Russell, and K. Morinaga, "Effect of poling conditions on second-harmonic generation in fused silica," Opt. Lett. **21**, 468 (1996).

[57] K. Tanaka, K. Kashima, K. Hirao, N. Soga, S. Yamagata, A. Mito, and H. Nasu, "Highly efficient optical second harmonic generation in poled Ti-doped silica glasses," Jpn. J. Appl. Phys **34**, 175 (1995).

[58] M. Miyata, H. Nasu, A. Mito, T. Hashimoto, and K. Kamiya, "Second-order optical nonlinearity in electrically poled silicate glass containing Ga_2O_3," Jpn. J. Appl. Phys. **36**, L865 (1997).

[59] W. Margulis, F.C. Garcia, E.N. Hering, I.C.S. Carvalho, B. Lesche, and F. Laurell, "Creating a second-order nonlinearity and a waveguide in soft glasses by poling," in *Bragg Gratings, Photosensitivity, and Poling in Glass Fibers and Waveguides: Applications and Fundamentals*, OSA Technical Digest Series Vol. **17**, 310 (1997).

[60] K. Tanaka, K. Kashima, K. Hirao, N. Soga, S. Yamagata, A. Mito, and H. Nasu, "Effect of γ-irradiation on optical second harmonic intensity of electrically poled silica glass," Jpn. J. Appl. Phys. **34**, 173, (1995).

[61] A. Kameyama, E. Muroi, A. Yokotani, K. Kurosawa, and P.R. Herman, "X-ray radiation effects on second-harmonic generation in thermally poled silica glass," J. Opt. Soc. Am. B **14**, 1088 (1997).

[62] T. Hirama, H. Muto, O. Sugihara, and N. Okamoto, "Highly-active second-order nonlinearity from sol-gel processed poled silica and germanosilicate thin-film," Opt. Rev. 3, 17 (1996).

[63] O. Sugihara, T. Hirama, H. Fujimura, and N. Okamoto, "Second-order nonlinear optical properties from poled silicate channel-waveguide," Opt. Rev. 3, 150 (1996).

[64] O. Sugihara, M. Nakanishi, H. Fujimura, C. Egami, and N. Okamoto, "Thermally poled silicate thin films with large second-harmonic generation," J. Opt. Soc. Am. B **15**, 421 (1998).

[65] R.A. Myers, S.R.J. Brueck, and R.P. Tumminelli, "Stable second-order nonlinearity in SiO2-based waveguides on Si using temperature/electric field poling," in: *Doped Fiber Devices and Systems*, Proc. M.J.F. Digonnet, ed., SPIE **2289**, 98 (1994).

[66] R.A. Myers, X.-C. Long, S.R.J. Brueck, and R.P. Tumminelli, "Effect of hydrogen loading on temperature/electric-field poling of SiO_2-based thin films on Si," Electron. Lett. **31**, 1604 (1995).

[67] P.G. Kazansky, L. Dong, and P.St.J. Russell, "High second-order nonlinearities in poled silicate fibers," Opt. Lett. **19**, 701 (1994).

[68] R. Kashyap, "Phase-matched periodic electric-field-induced second-harmonic generation in optical fibers," J. Opt. Soc. Am. B **6**, 313 (1989).

[69] P.S. Weitsman, J.J. Kester and U. Osterberg, "Electric field induced second harmonic generation in germanium doped silica planar waveguides," Electron. Lett. **30**, 697 (1994).

[70] R. Kashyap, G.J. Veldhuis, D.C. Rogers, and P.F. Mckee, "Phase-matched second-harmonic generation by periodic poling of fused silica," Appl. Phys. Lett. **64**, 1332 (1993).

[71] D. Statman and J.A. Georges III, "Charge dynamics and poling in glass waveguides," J. Appl. Phys. **80**, 654 (1996).

[72] P.G. Kazansky, V. Pruneri, and P.St.J. Russell, "Blue-light generation by quasiphase-matched frequency doubling in thermally poled optical fibers," Opt. Lett. **20**, 843 (1995).

[73] V. Pruneri and P.G. Kazansky, "Frequency doubling of picosecond pulses in periodically poled D-shape silica fibre," Electron. Lett. **33**, 318 (1997).

[74] V. Pruneri and P.G. Kazansky, "Electric-field thermally poled optical fibers for quasi-phase-matched second-harmonic generation," IEEE Photon. Tech. Lett. **9**, 185 (1997).

[75] P.G. Kazansky and V. Pruneri, "Electric-field poling of quasi-phase-matched optical fibers," J. Opt. Soc. Am. B **14**, 2170 (1997).

[76] V. Pruneri, G. Bonfrate, P.G. Kazansky, C. Simonneau, P. Vidakovic, and J.A. Levenson, "Efficient frequency doubling of 1.5 mm femtosecond laser pulses in quasi-phase-matched optical fibers," Appl. Phys. Lett. **72**, 1007 (1998).

[77] X.C. Long, R.A. Myers, and S.R.J. Brueck, "Measurement of the linear electro-optic coefficient in poled amorphous silica," Opt. Lett. **19**, 1819 (1994).

[78] X.C. Long, R.A. Myers, and S.R.J. Brueck, "Measurement of the linear electro-optic coefficient in temperature/electric-field poled optical fibers," Electron. Lett. **30**, 2162 (1994).

[79] P.G. Kazansky, P.St.J. Russell, and C.N. Pannell, "Optical fiber electrets: Observation of electro-acoustic-optic transduction," Electron. Lett. **30**, 1436 (1994).

[80] P.G. Kazansky, P.St.J. Russell, L. Dong and C.N. Pannell, "Pockels effect in thermally poled optical fibers," Electron. Lett. **31**, 62 (1995).

[81] A.C. Liu, M.J.F. Digonnet, and G.S. Kino, "Electro-optic phase modulation in silica channel waveguide," Opt. Lett. **19**, 466 (1994).

[82] X.C. Long, R.A. Myers, and S.R.J. Brueck, "A poled electrooptic fiber," IEEE Photon. Tech. Lett. **8**, 227 (1996).

[83]M. Abe, T. Kitagawa, K. Hattori, A. Himeno, and Y. Ohmori, "Electro-optic switch constructed with a poled silica-based waveguide on a Si substrate," Electron. Lett. **32**, 893 (1996).

[84]I.C.S. Carvalho, C.M.B. Cordeiro, L.C. Guedes Valente, E.N. Hering, W. Margulis, F. Laurell, and R. Stubbe, "Electro-thermal poling of microfibers," in: *Bragg Gratings, Photosensitivity, and Poling in Glass Fibers and Waveguides: Applications and Fundamentals*, OSA Technical Digest Series Vol. **17**, 313 (1997).

[85] X.C. Long and S.R.J. Brueck, "Large-signal phase retardation with a poled electrooptic fiber," IEEE Photon. Tech. Lett. **9**, 767 (1997).

Chapter 2. Background

2.1 Nonlinear Optics and Second-Harmonic Generation

2.1.1 Polarization and Susceptibility

When light is incident on a material, the constituent electrons, atoms and molecules interact with the light and respond according to the light's intensity and frequency. The material response is typically given through its polarization response *P(t)*. The polarization is directly dependent on the field strength *E(t)* through the susceptibility:

$$P(t) = \chi E(t) \tag{2.1}$$

This is the response expected when dealing with linear optics. When the field is strong, there may be a response that is not linear. For example, if the polarization is expanded in a power series in *E(t)*,

$$P(t) = \chi^{(1)} E(t) + \chi^{(2)} E^2(t) + \chi^{(3)} E^3(t) + ... \tag{2.2}$$

one has susceptibility terms associated with each power in *E(t)*. $\chi^{(1)}$ is the linear susceptibility, $\chi^{(2)}$ is the second-order susceptibility, $\chi^{(3)}$ is the third-order susceptibility, and so on. Each additive term can respectively be described as a linear polarization, a second-order polarization, a third-order polarization, etc. When one talks of a second-order nonlinearity or third-order nonlinearity, it is in context of this polarization and susceptibility expansion.

2.1.2 Second-order nonlinearity

The second-harmonic (SH) signal originates from the second-order polarization. To see how one can generate the second-harmonic through this polarization, suppose that an incident electromagnetic wave has a single frequency and is given by:

$$E(t) = Ae^{-i(\omega t - \phi)} + c.c. \tag{2.3}$$

$$= 2A\cos(\omega t + \phi)$$

If one considers the second-order term only, the nonlinear polarization is given by

$$P^{(2)}(t) = \chi^{(2)} E^2(t) = \chi^{(2)} 4A^2 \cos^2(\omega t + \phi) \tag{2.4}$$

Since ϕ is arbitrary, one can set it to zero, and the equation can be written

$$P^{(2)}(t) = \chi^{(2)} 2A^2 (1 + \cos 2\omega t) \tag{2.5}$$

$$= \chi^{(2)} 2A^2 + \chi^{(2)} 2A^2 \cos 2\omega t$$

We now can see that due to the squared electric field term, the second-order polarization has a response at zero frequency (the first term on the left hand side) and a frequency doubled response at 2ω (the second term). The zero frequency term is known as optical rectification and results in a static electric field within the material. The frequency doubled term is the SH.

To consider more generally the effect of the second-order polarization, suppose the incident electric field is given by two frequencies:

$$E(t) = E_1 e^{-i(\omega_1 t)} + E_2 e^{-i(\omega_2 t)} + c.c. \tag{2.6}$$

31

The second-order polarization becomes

$$P^{(2)}(t) = \chi^{(2)}[E_1^2 e^{-i2\omega_1 t} + E_2^2 e^{-i2\omega_2 t} + 2E_1 E_2 e^{-i(\omega_1 + \omega_2)t} \qquad (2.7)$$

$$+ 2E_1 E_2^* e^{-i(\omega_1 - \omega_2)t} + c.c.] + 2\chi^{(2)}[E_1 E_1^* + E_2 E_2^*]$$

The five terms on the right-hand side can be classified as different nonlinear effects.

SHG at $2\omega_1$ and $2\omega_2$ is given by the $\chi^{(2)}E_1^2$ and $\chi^{(2)}E_2^2$ terms. Sum frequency

generation at $\omega_1 + \omega_2$ is given by $2\chi^{(2)}E_1 E_2$, difference frequency generation at

$\omega_1 - \omega_2$ is given by $2\chi^{(2)}E_1 E_2^*$ and optical rectification at zero frequency is given by

$2\chi^{(2)}\left[E_1 E_1^* + E_2 E_2^*\right]$.

2.1.3 Wave propagation analysis of second-order interaction

2.1.3.1 The nonlinear wave equation

In order to describe the interaction of electromagnetic waves in nonlinear media,

one starts with Maxwell's equations:

$$\nabla \times \mathbf{H} = \mathbf{J} + \frac{\partial \mathbf{D}}{\partial t} \qquad \nabla \cdot \mathbf{D} = \rho \qquad (2.8)$$

$$\nabla \times \mathbf{E} = -\frac{\partial \mathbf{B}}{\partial t} \qquad \nabla \cdot \mathbf{B} = 0$$

Using $\mathbf{B} = \mu_0 \mathbf{H}$ (μ_0 is the permeability of free space), and assuming no free charges or

currents ($\rho = 0$, $\mathbf{J} = 0$), the wave equation is obtained from the two curl equations from

(2.8):

$$\nabla \times \nabla \times \mathbf{E} = -\mu_0 \frac{\partial^2 \mathbf{D}}{\partial^2 t} \qquad (2.9)$$

32

With $\mathbf{D} = \varepsilon_0 \mathbf{E} + \mathbf{P}$, substitution in equation (2.9) gives

$$\nabla \times \nabla \times \mathbf{E} + \mu_0 \varepsilon_0 \frac{\partial^2 \mathbf{E}}{\partial^2 t} = -\mu_0 \frac{\partial^2 \mathbf{P}}{\partial^2 t} \tag{2.10}$$

ε_0 is the permitivity of free space. The following identity can be used to rewrite equation (2.10):

$$\nabla \times \nabla \times \mathbf{E} = \nabla(\nabla \cdot \mathbf{E}) - \nabla^2 \mathbf{E} \tag{2.11}$$

The $\nabla \cdot \mathbf{E}$ term is typically small (equals zero if there are no free charges), so the wave equation can be approximated as:

$$\nabla^2 \mathbf{E} + \mu_0 \varepsilon_0 \frac{\partial^2 \mathbf{E}}{\partial^2 t} = -\mu_0 \frac{\partial^2 \mathbf{P}}{\partial^2 t} \tag{2.12}$$

where the polarization has both linear and nonlinear terms, $\mathbf{P} = \mathbf{P}_l + \mathbf{P}_{nl}$, so the equation becomes

$$\nabla^2 \mathbf{E} + \mu_0 \varepsilon_0 \frac{\partial^2 \mathbf{E}}{\partial^2 t} = -\mu_0 \frac{\partial^2 (\mathbf{P}_l + \mathbf{P}_{nl})}{\partial^2 t} \tag{2.13}$$

The linear polarization term can be written in terms of a linear susceptibility, $\mathbf{P}_l = \varepsilon_0 \chi_l \mathbf{E}$, where the linear susceptibility is related to a linear dielectric constant by $\varepsilon = \varepsilon_0 (1 + \chi_l)$. Using this, the wave equation can be rewritten in terms of the dielectric constant and the nonlinear polarization:

$$\nabla^2 \mathbf{E} + \mu_0 \varepsilon \frac{\partial^2 \mathbf{E}}{\partial^2 t} = -\mu_0 \frac{\partial^2 \mathbf{P}_{nl}}{\partial^2 t} \tag{2.14}$$

This is the nonlinear optical wave equation for source free media. It can be written in scalar notation for the simple case of $\mathbf{P}_{nl}$ parallel to $\mathbf{E}$ as:

$$\nabla^2 E + \mu_0 \varepsilon \frac{\partial^2 E}{\partial^2 t} = -\mu_0 \frac{\partial^2 P_{nl}}{\partial^2 t} \tag{2.15}$$

2.1.3.2 Three-wave interaction

The nonlinear optical wave equation specifies the behavior of interacting waves in a nonlinear medium. Second-order nonlinearities involve the interaction of three waves. The three waves can be represented as follows (similar to the development done by Yariv[1]), considering propagation in one dimension with plane waves consisting of three frequencies:

$$E^{(\omega_1)}(z,t) = \frac{1}{2}\left[E_1(z)e^{i(\omega_1 t - k_1 z)} + c.c.\right] \quad (2.16)$$

$$E^{(\omega_2)}(z,t) = \frac{1}{2}\left[E_2(z)e^{i(\omega_2 t - k_2 z)} + c.c.\right] \quad (2.17)$$

$$E^{(\omega_3)}(z,t) = \frac{1}{2}\left[E_3(z)e^{i(\omega_3 t - k_3 z)} + c.c.\right] \quad (2.18)$$

The subscripts 1, 2, and 3 refer to frequencies. For the case of $\omega_3 = \omega_1 + \omega_2$ the nonlinear polarization is of the form:

$$\left[P_{nl}^{(\omega_3)}(z,t)\right] = \frac{1}{2}\chi^{(2)}E_1(z)E_2(z)e^{i[(\omega_1+\omega_2)t-(k_1+k_2)z]} + c.c. \quad (2.19)$$

Equations (2.16) - (2.18) can be used with equation (2.14). We see that when eqn. (2.18) is used with eqn. (2.14) assuming plane wave propagation, we get:

$$\nabla^2 E^{(\omega_3)}(z,t) = \frac{1}{2}\frac{\partial^2}{\partial z^2}\left[E_3(z)e^{i(\omega_3 t - k_3 z)} + c.c.\right] \quad (2.20)$$

A slowly varying envelope approximation (SVEA) is used to approximate the fact E does not vary much over an optical wavelength (~ 1 μm). SVEA assumes

$$\frac{dE_3}{dz}k_1 >> \frac{d^2 E_3}{dz^2} \quad (2.21)$$

34

With this approximation equation (2.20) becomes:

$$\nabla^2 E^{(\omega_3)}(z,t) = -\frac{1}{2}\left[k_3^2 E_3(z) + 2ik_3\frac{dE_3(z)}{dz}\right]e^{i(\omega_3 t - k_3 z)} + c.c. \qquad (2.22)$$

Similar expressions exist for the other two frequencies. If eqn. (2.22) is substituted into eqn. (2.15), and using $\frac{\partial}{\partial t} = i\omega$, the wave equation becomes:

$$-\frac{1}{2}\left[k_3^2 E_3(z) + 2ik_3\frac{dE_3(z)}{dz}\right]e^{i(\omega_3 t - k_3 z)} + c.c.$$

$$= -\omega_3^2\mu_0\varepsilon_3\left[\frac{E_3(z)}{2}e^{i(\omega_3 t - k_3 z)}\right] + c.c. - \left[\frac{\omega_3^2\mu_0\chi^{(2)}}{2}E_1(z)E_2(z)e^{i[\omega_3 t - (k_1 + k_2)z]} + c.c.\right] \qquad (2.23)$$

All terms are then multiplied by $\frac{i}{k_3}e^{-i(\omega_3 t - k_3 z)}$ and recognizing that $k_3^2 = \omega_3^2\mu_0\varepsilon_3$, eqn. (2.23) becomes

$$\frac{dE_3}{dz} = -\frac{i\omega_3}{2}\sqrt{\frac{\mu_0}{\varepsilon_3}}\chi^{(2)}E_1 E_2 e^{-i(k_1 + k_2 - k_3)z} \qquad (2.24)$$

Similarly,

$$\frac{dE_2^*}{dz} = +\frac{i\omega_2}{2}\sqrt{\frac{\mu_0}{\varepsilon_2}}\chi^{(2)}E_1 E_3^* e^{-i(k_1 - k_3 + k_2)z} \qquad (2.25)$$

$$\frac{dE_1}{dz} = -\frac{i\omega_1}{2}\sqrt{\frac{\mu_0}{\varepsilon_1}}\chi^{(2)}E_3 E_2^* e^{-i(k_3 - k_2 - k_1)z} \qquad (2.26)$$

These are the coupled wave equations that describe second-order three-wave interactions.

2.1.4 Second Harmonic Generation(SHG)

In 1961, not long after the development of the laser, Franken et al.[2] demonstrated for the first time the ability of a nonlinear optical (NLO) material, in this case quartz, to produce frequency-doubled light. In the first demonstration, fundamental light of a ruby laser at 694 nm was converted to the second harmonic at 347 nm.

35

SHG can be described through the coupled wave equations developed above. In the case of SHG, two of the waves have the same frequency $\omega_1 = \omega_2 = \omega$, such that the third wave has $\omega_3 = \omega_1 + \omega_2 = 2\omega$. Therefore, eqn. (2.24) becomes:

$$\frac{dE^{(2\omega)}}{dz} = -\frac{i\omega}{2}\sqrt{\frac{\mu_0}{\varepsilon}}\chi^{(2)}\left[E^{(\omega)}(z)\right]^2 e^{i(\Delta k)z} \tag{2.27}$$

where the wavenumber mismatch is given by

$$\Delta k = k_3 - 2k_1 = k^{(2\omega)} - 2k^{(\omega)} \tag{2.28}$$

Eqn. (2.27) can be integrated to give the field amplitude after passing through a NLO material of length L. If the depletion of the fundamental wave at ω is assumed to be negligible as it is converted to 2ω, the integration gives

$$E^{(2\omega)}(L) = -\frac{i\omega}{2}\sqrt{\frac{\mu_0}{\varepsilon}}\chi^{(2)}[E^{(\omega)}]^2 \frac{e^{i\Delta kL}-1}{i\Delta k} \tag{2.29}$$

The output power is then found from EE^*:

$$E^{(2\omega)}(L)E^{(2\omega)*}(L) = \left(\frac{\mu_0}{\varepsilon_0}\right)\frac{\omega^2[\chi^{(2)}]^2}{n^2(\omega)}L^2[E^{(\omega)}]^4 \frac{\sin^2\left(\frac{\Delta kL}{2}\right)}{\left(\frac{\Delta kL}{2}\right)^2} \tag{2.30}$$

where the relation $\frac{\varepsilon}{\varepsilon_0} = n^2$ has been used. The power per unit area is the intensity and is related to the field by

$$I_{2\omega} = \frac{P_{2\omega}}{A} = \frac{1}{2}\sqrt{\frac{\varepsilon^{(2\omega)}}{\mu_0}}\left|E^{(2\omega)}\right|^2 \tag{2.31}$$

The second harmonic intensity can therefore be written as

$$I_{2\omega} = \left[2\left(\frac{\mu_0}{\varepsilon_0}\right)^{3/2}\frac{[\chi^{(2)}]^2 L^2\omega^2}{n^2(\omega)n(2\omega)}\right]\left[\frac{\left(P^{(\omega)}\right)^2}{A^2}\right]\left[\frac{\sin^2\left(\frac{\Delta kL}{2}\right)}{\left(\frac{\Delta kL}{2}\right)^2}\right] \tag{2.32}$$

36

2.1.5 Phase Matching

Note that the intensity in eqn (2.32) has a spatial interference pattern which is a squared sinc function of a phase mismatch factor, $\Delta k L/2$. This factor has its largest maximum at $\Delta k L/2 = 0$, and has zeros when $\Delta k L/2 = m\pi$ $(m = 1,2,3...)$. A coherence length can be defined by the distance between the maximum peak and the first minima as

$$l_c = \frac{\pi}{\Delta k} \tag{2.33}$$

Others find it useful to define the coherence length as $L_c = \frac{2}{\Delta k}$, so that the squared sinc function can be written as $\mathrm{sinc}^2(L/L_c)$.[3] The coherence length is essentially a measure of the maximum useful crystal length.

In 1962, Armstrong et al.[4] solved the coupled wave equations, allowing for depletion of the fundamental wave. The derivation won't be given here, however the solution for the case of $\Delta k = 0$ (perfect phase matching) is shown in figure (2.1). The field amplitudes are given by

$$E^{(\omega)}\left(\tfrac{z}{l_c}\right) = \mathrm{sech}\left(\tfrac{z}{l_c}\right)$$
$$E^{(2\omega)}\left(\tfrac{z}{l_c}\right) = \tanh\left(\tfrac{z}{l_c}\right) \tag{2.34}$$

where z is the propagation distance through the nonlinear medium, and l_c is the coherence length or characteristic distance over which the fields exchange energy.

Next, consider the case of arbitrary Δk, where the phase matching is no longer perfect. To simplify matters, depletion of the fundamental pump beam will considered to be negligible. This is valid when conversion efficiencies are low. The second harmonic intensity is given by equation (2.32). Note that the intensity is proportional to a squared
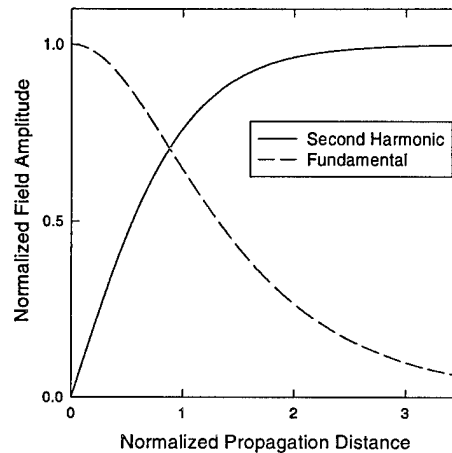
Figure 2.1 Variation of the fundamental and second-harmonic fields as a function of propagation distance in the nonlinear medium for the case of perfect phase matching.

sinc function. At lengths less than one coherence length, the intensity grows, as is seen in the curve labeled "no phase matching" in figure (2.2). After a coherence length, the intensity previously generated through constructive nonlinear wave interaction decreases to zero from destructive interaction. The second harmonic intensity will continue to rise and fall as it passes through additional coherence lengths.

The lack of significant growth in the second-harmonic can be rectified by various methods of phase matching. Usually, collinear phase matching (depicted in figure 2.3 (a)), does not take place due to frequency dispersion in the optical material. Traditional phase matching methods involve birefringent angle-tuning or temperature-tuning a nonlinear crystal such that two wave vectors (k_1 and k_2) of the second harmonic vectorally add to

38

equal one fundamental wave vector (k_3) as seen in figure 2.3 (b). When this occurs, $\Delta k = 0$, and we have perfect phase matching. The growth of phase matched SHG is also shown in figure (2.2) for the case of a nondepleted pump.
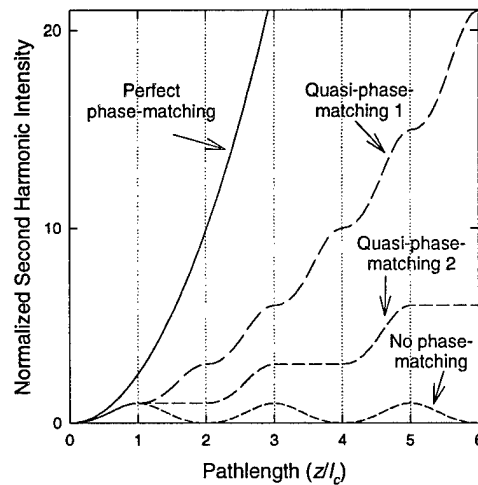
Figure 2.2 Effects of various types of phase-matching for second harmonic generation. Assumes a non-depleted pump.
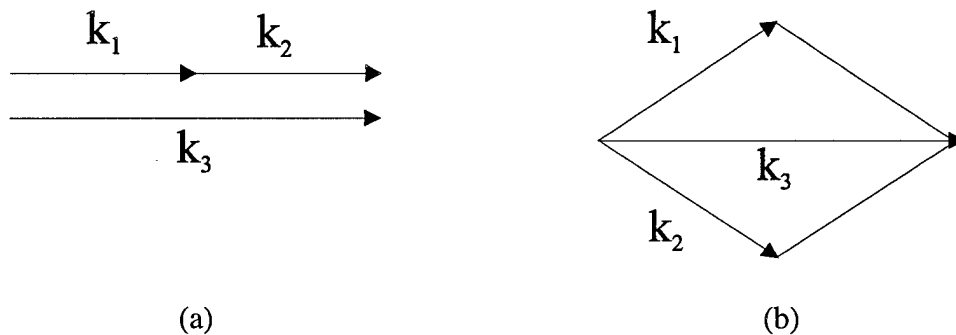
Figure 2.3 Collinear phase matching (a) and vector phase matching (b).

Another way to get significant second-harmonic growth is to use quasi-phase matching (QPM). The idea of QPM is to modulate the nonlinear susceptibility with a period that matches the coherence length in the nonlinear medium. The idea surfaced as early as 1962 with the theoretical work of Armstrong et al.[4] In more recent years, the

ability to fabricate and control micro-patterned electrodes has caused widespread use of periodically-poled lithium niobate (PPLN) for second-order nonlinear optical studies.[5] PPLN makes use of QPM by reversing the nonlinear polarization every coherence length. The polarization direction is reversed by alternating the polarity of the patterned electrodes which are made to match the coherence length, thus causing polarization domain reversal in the material. The effect of this periodic poling is seen in the curve marked "quasi-phase-matching 1" in figure (2.2). After second harmonic light grows in the first coherence length, the reversed polarization in the second coherence length allows the intensity to continue to grow. Each subsequent coherence length continues the trend.

This type of phase matching also occurs when second harmonic light is generated through the photoinduced second-order nonlinearity observed in fibers.[6,7] The effect is self-organized and is believed to result from a periodic variation of electric field and asymmetric photocurrent.[8-11] Even though the second-order nonlinearity is low ($\chi^{(2)}$ ~ 10^{-3} to 10^{-4} pm/V), the self-organized quasi-phase-matching allows the second harmonic power to build to efficient levels. Osterberg and Margulis[6] reported conversion efficiencies as high as ~ 5 %.

Another type of phase matching that can occur is shown in the curve marked "quasi-phase-matching 2" in figure (2.2). This is representative of the phase-matching that can be achieved through periodic poling in glass. Because thermal poling causes a thin nonlinear region to form near the anode, reversing adjacent polarization domains is not feasible. Instead, an adjacent coherence length can be skipped and not poled at all, leaving it with no second-order nonlinearity. When this is done, regions which would

have diminished the intensity are skipped, and every other coherence length contributes constructively to building the second harmonic intensity as seen in figure (2.2). This second type of QPM has been demonstrated by periodic poling of bulk fused silica, waveguides and fibers.[12-17] The periodic poling achieved in fibers by the University of Southampton group involves depositing a patterned aluminum electrode with a period matching two effective coherence lengths on the flat side of a D-shaped optical fiber. The electrode is connected to a high voltage while the other side of the fiber is connected to a ground electrode.

2.1.6 The susceptibility tensor and spatial symmetry

In order to take into account the asymmetries that can exist in a nonlinear medium, the nonlinear polarization should be written with its cartesian components and different frequencies explicitly expressed. The second-order susceptibility becomes the tensor $\chi_{ijk}^{(2)}$, where each letter i, j, and k can take on any of the spatial coordinates x, y, and z. The factor of ε_0 is now included in the tensor $\chi_{ijk}^{(2)}$. The sum frequency polarization is thus written

$$P_i^{(\omega_n + \omega_m)} = \sum_{jk(nm)} \chi_{ijk}^{(2)}(\omega_n + \omega_m; \omega_n, \omega_m) E_j^{(\omega_n)} E_k^{(\omega_m)} \tag{2.35}$$

for different frequencies ω_n and ω_m. For second harmonic generation we have

$$P_i^{(2\omega)} = \sum_{jk} \chi_{ijk}^{(2)}(2\omega, \omega, \omega) E_j^{(\omega)} E_k^{(\omega)}. \tag{2.36}$$

There are several symmetries and restrictions that reduce the number of tensor components that need to be specified. I will not elaborate on these symmetries and

41

restrictions; they are more fully described in ref. (3). The symmetries and restrictions include intrinsic permutation symmetry, the full permutation symmetry for lossless media, the restrictions that the fields must be real, as well as that the components of the tensor must be real for lossless media. Kleinman's symmetry, which allows one to treat the frequencies as indistinguishable, can be invoked for frequencies much smaller than the lowest resonance frequency. Because the frequencies we consider are in the optical domain, we can consider the material to be far from resonance and the dispersion to be negligible. This leads to a reduction in the number of components that are necessary for a general description of the nonlinear susceptibility tensor. The tensor is usually expressed in the "d" notation, where

$$d_{ijk} = \tfrac{1}{2}\chi^{(2)}_{ijk}.$$

(2.37)

The jk specification in the d matrix can be contracted to a single component l such that only a 3 x 6 matrix is left. l is prescribed by the following method:

l:	1	2	3	4	5	6
jk:	11	22	33	23,32	31,13	12,21

The polarization for second harmonic generation can then be described through d_{il} by the following equation:

$$
\begin{bmatrix} P_x^{(2\omega)} \\ P_y^{(2\omega)} \\ P_z^{(2\omega)} \end{bmatrix} = 2 \begin{bmatrix} d_{11} & d_{12} & d_{13} & d_{14} & d_{15} & d_{16} \\ d_{21} & d_{22} & d_{23} & d_{24} & d_{25} & d_{26} \\ d_{31} & d_{32} & d_{33} & d_{34} & d_{35} & d_{36} \end{bmatrix} \begin{bmatrix} \left(E_x^{(\omega)}\right)^2 \\ \left(E_y^{(\omega)}\right)^2 \\ \left(E_z^{(\omega)}\right)^2 \\ 2E_y^{(\omega)}E_z^{(\omega)} \\ 2E_x^{(\omega)}E_z^{(\omega)} \\ 2E_x^{(\omega)}E_y^{(\omega)} \end{bmatrix}.
$$

(2.38)

42

The quantities in the d matrix will be determined by the type of nonlinear crystal or medium being used. For material that is optically uniaxial with a single axis of symmetry designated by the z-axis and two disordered and indistinguishable axes x and y, the symmetry is designated as a ∞mm point group. The d matrix is given by[18,19]:

$$d_{il} = \begin{bmatrix} 0 & 0 & 0 & 0 & d_{31} & 0 \\ 0 & 0 & 0 & d_{31} & 0 & 0 \\ d_{31} & d_{31} & d_{33} & 0 & 0 & 0 \end{bmatrix}. \tag{2.39}$$

so that the nonlinear polarization becomes:

$$\begin{bmatrix} P_x^{(2\omega)} \\ P_y^{(2\omega)} \\ P_z^{(2\omega)} \end{bmatrix} = 2 \begin{bmatrix} 2d_{31}E_x^{(\omega)}E_z^{(\omega)} \\ 2d_{31}E_y^{(\omega)}E_z^{(\omega)} \\ d_{31}E_x^2 + d_{31}E_y^2 + d_{33}E_z^2 \end{bmatrix}. \tag{2.40}$$

This relationship applies to thermally poled fused silica because it becomes a ∞mm crystal class material with a single axis of symmetry in the poling process. The single axis of symmetry (z-axis) is the same as the direction of the applied electric field and the resultant frozen-in electric field.

2.1.7 Possible origins of the $\chi^{(2)}$

There are two mechanisms that have been proposed as possible origins of the second-order nonlinearity in fused silica. Both mechanisms rely on the establishment of a "frozen-in" electric field E_{dc} in the glass. The first is an "effective $\chi^{(2)}$"[20] which originates through the third-order susceptibility inherent in the glass as in

$$\chi_{eff}^{(2)} = 3\chi^{(3)}E_{dc} \tag{2.41}$$

where the factor of three comes from degeneracy considerations.[21]

The second-order nonlinear coefficients, χ_{33} and χ_{31}, in this case, are expected to be related by $3\chi_{31}^{(2)} = \chi_{33}^{(2)}$ due to Kleinman's symmetry.[22] (In terms of a full third-order susceptibility tensor, this means $\chi_{1111}^{(3)} = 3\chi_{1122}^{(3)} = 3\chi_{1212}^{(3)} = 3\chi_{1221}^{(3)}$ when the source of the nonlinearity is in the optical Kerr effect[23]). The third-order optical Kerr susceptibility ($\chi_{1111}^{(3)}$) in Ge-doped silica fiber is reported[24] to be ~ 2 x 10^{-22} m^2/V^2 and for fused silica, the third-order optical Kerr[25,26] and DC Kerr[27] ($\chi_{1111}^{(3)} - \chi_{1122}^{(3)}$) susceptibilities are also reported to be ~ 0.5-2 x 10^{-22} m^2/V^2. The $\chi^{(2)}$ in thermally poled fused silica is on the order of 1 pm/V. Using reported $\chi^{(3)}$ values, the average electric field required to create the $\chi^{(2)}$ through $\chi^{(3)}E$ would be ~1.5 x 10^7 V/cm. This is a very large field, given that the inter-atomic field is ~10^8 V/cm and the breakdown field reported[28] by a glass-manufacturer in fused silica is ~ 3 x 10^7 V/cm.

The other mechanism, which could be in place of or in addition to $\chi^{(3)}E$, comes through possible orientation of bonds in the field.[29] In this case the nonlinearity is related to the polarizability of the bonds or dipoles, and when expressed in terms of the d coefficients is given by:[18]

$$
\begin{aligned}
d_{33} &= N\beta f^{\omega} f^{\omega} f^{2\omega} f^0 \left\langle \cos^3 \theta \right\rangle \\
d_{31} &= \tfrac{1}{2} N\beta f^{\omega} f^{\omega} f^{2\omega} f^0 \left(\left\langle \cos\theta \right\rangle - \left\langle \cos^3 \theta \right\rangle \right)
\end{aligned}
\tag{2.42}
$$

Here, N is the number of orientable moieties, β is the hyperpolarizability, f^{ω}, $f^{2\omega}$, and f^0 are local field factors, and θ is the angle between E_{dc} and the axis of the bond or dipole.

The $\left\langle \cos^3 \theta \right\rangle$ and $\left\langle \cos\theta \right\rangle$ terms represent orientation averages. In a low-field

approximation, the coefficients are given by:[30]

$$
\begin{aligned}
d_{33} &= N\beta f^{\omega} f^{\omega} f^{2\omega} f^{0}\left(\mu E_{dc} / 5kT\right) \\
d_{31} &= N\beta f^{\omega} f^{\omega} f^{2\omega} f^{0}\left(\mu E_{dc} / 15kT\right)
\end{aligned}, \tag{2.43}
$$

where T is the temperature ($\sim 275°C$, during thermal poling), and μ is dipole moment.

Once again, one can see that there is a theoretical factor of 3 for the ratio of coefficients

d_{31} to d_{33} (χ_{31} to χ_{33}). The expected value is $3\chi_{31} = \chi_{33}$ for the case of field oriented

dipoles in a low-field approximation. High fields ($E_{dc} > 10kT/\mu$) may lead to variations

in this ratio, depending on the β and μ of the originating dipole and the strength of the

electric field.

The relative value of χ_{31} to χ_{33} in thermally poled fused silica has been measured.

This is done by comparing s and p polarizations of SHG. Myers et al.[20] first reported a

value of $\sim 2\chi_{31} = \chi_{33}$ but Myers later measured and recalculated $2.6\chi_{31} = \chi_{33}$.[31]

Kazansky and Russell[32] also reported a measurement, finding 2.8 to $2.9\chi_{31} = \chi_{33}$. Both

measurements have values close to 3, which is consistent with both the $\chi^{(3)}E$ or the

orientation mechanism.

The strength of $\chi_{33}^{(2)}$ (~ 1 pm/V) in the nonlinear region in fused silica should be

compared to the nonlinear susceptibilities of other materials at $\lambda = 1.06$ μm, such as

LiNbO$_3$ ($\chi_{33}^{(2)} = 55$ pm/V, $\chi_{22}^{(2)} = 5.3$ pm/V), KDP (KH$_2$PO$_4$) ($\chi_{36}^{(2)} = 0.74$ pm/V) and quartz

($\chi_{11}^{(2)} = 0.68$ pm/V).[33] Keep in mind that the nonlinear region in fused silica is small (~ 10

μm) and not distributed uniformly throughout the material as in most second-order nonlinear materials.

It should be noted that a large concentration of defects would be required if the nonlinearity is attributed entirely to an orientation mechanism in the space charge region, and a reasonable hyperpolarizability (e.g. $\beta \sim 10^{-38}$ m^4/V for p-nitroaniline polymer[34]) is assumed. To estimate the number of defects, one can assume that for electric-field oriented polarizable materials, $\chi_{33}^{(2)} = \frac{2N\beta\mu E_{dc}}{5kT}$ (assuming the local field factors are unity), where N is the number of orientable defects, β is the hyperpolarizability, μ is the dipole moment, E_{dc} is the electric field strength, and T is the temperature. A rough estimate can be made using a very large dipole moment ($\mu = 0.5\ e$ nm $= 8 \times 10^{-29}$ C m $= 23.5\ D$), a polymer-level hyperpolarizability $\beta \sim 10^{-38}$ m^4/V, $E_{dc} \sim 1 \times 10^7$ V/cm, $\chi^{(2)} \sim 1$ pm/V and $T \sim 550$ K, which leads to $N \sim 2 \times 10^{21}$ cm^{-3}. This is much larger than the number of defects that would be associated with alkali impurities. A smaller μ or β would make matters worse. Alternatively, using an estimated value of the number of defects $N = 2 \times 10^{17}$ cm^{-3} (10 ppm) leads to $\beta \sim 10^{-34}$ m^4/V, which is much larger than any known molecular hyperpolarizability.

2.2 Fused silica glass

2.2.1 Types

In the broadest terms, a glass is a non-crystalline, amorphous solid-state material. Optical glasses, which are engineered for their linear optical properties, tend to be oxide glasses. Prior to 1880, there were two types of glasses: simple crown and flint glasses.

The crown glass was a soda-lime silicate with a low refractive index and low dispersion while the flint was a lead silicate with high dispersion.[35] Now there are hundreds of optical glasses of various chemical compositions. Those based on SiO_2 network formers are called silicates. They may contain substantial amounts of other oxides. For example, soda-lime silicate glass, which is usually used to make common microscope slides, has up to 35 wt% Na_2O. Fused silica glass is a much purer silicate with only trace amounts of impurities. It is typically $>> 99\%$ SiO_2, with 10 to 100 ppm being other oxides such as Al_2O_3 or Fe_2O_3. OH is often the dominant impurity at levels of 100 to 1200 ppm. Its crystalline counterpart is quartz.

Four types of fused silica glass made from four different manufacturing methods are conventionally labeled as types I, II, III, and IV. Types I and II come from quartz, which is fused to form what's called "natural" fused silica or just "fused quartz". Type I is formed from electrical fusion of quartz, and type II is formed from flame-fusion of quartz. Types III and IV are forms of "synthetic" fused silica. Type III is formed from flame-fusion of $SiCl_4$ and O_2 and type IV is formed from plasma-fusion. Differences occur in purity levels between different types. Types I and II, because they are made from quartz, contain alkali metal and aluminum impurities at the 1 to 50 ppm levels. For types III and IV, these alkali metal and Al impurities are usually less than 1 ppm, or ~ 0.1 ppm. Types II and III are both manufactured through flame-fusion processes which tend to introduce a large hydroxyl concentration due to water-vapor in the preparation environment. The OH concentration typically ranges from ~ 100 to 1200 ppm, with the highest concentrations in type III glasses. Optical absorption through these glasses is in large part determined by

the impurity level. High OH levels produce absorption in the infrared, while high alkali

impurity levels produce absorption in the near-UV.

Table 2.1 lists the basic types, several manufacturers and several of their

traditional brand names.[36]

Manufacturer	Type I	Type II	Type III	Type IV
Thermal Syndicate, Ltd. (Great Britain)	Vitreosil IR	Vitreosil 055, Vitreosil 066	Spectrosil A, Spectrosil B	Spectrosil WF
Heraeus Quarzshmelze (Germany)	Infralux, Infrasil	Heralux, Herasil, Homosil, Ultrasil	Suprasil	Suprasil W
Quartz et Silice (France)	Pursil K Puropsil		Tetrasil	Tetrasil SE
Corning Glass Works (USA)			7940	7943
General Electric (USA)	201, 204, 206, 214, 101, 105, 106	102, 104	151	
Nippon Sekiei Garasu Co. (Japan)	IF	UF, SG		WF
Heraeus-Amersil (USA)		Amersil, Optosil		

Table 2.1 Various types, manufacturers and brand names of fused silica. (After Fanderlik[36])

2.2.2 Fused silica structure

In a pure silica glass SiO_4-tetrahedra are the molecular basis of the structure.

SiO_4-tetrahedra also form the basis of the quartz crystalline structure. The SiO_4-tetrahedra

consist of four oxygen atoms connected to a silicon atom as seen in figure 2.4. In both
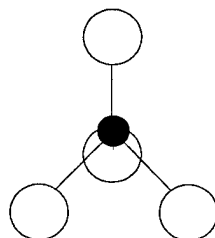
Figure 2.4 SiO_4 tetrahedra. Open circles are oxygen, filled circle is silicon.

the quartz crystal and the glass, each (bridging) oxygen connects to two silicon atoms.

The glass structure, however is a 3-dimensional non-periodic network chain of

intertwined basic units. For example, consider a hypothetical 2-dimensional (2-D) silica

crystal. In the 2-D case the silicon is surrounded by 3 oxygen atoms (for 3-D, 4 O atoms),

and each oxygen has two neighboring silicon atoms. This is seen in figure 2.5 (a).

Though the 2-D depiction shows Si-O-Si angles at 180°, the 3-D Si-O-Si group gives an

average angle around 145° (found by x-ray diffraction). Note the periodic hexagonal

pattern formed in the crystal. The hexagonal pattern also occurs in the true 3-D structure

of quartz when observed along one direction (the z-axis). When pictured in the

transverse direction, the hexagon consists of SiO_4-tetrahedra that form spiral-chains along

(a)   (b)   (c)
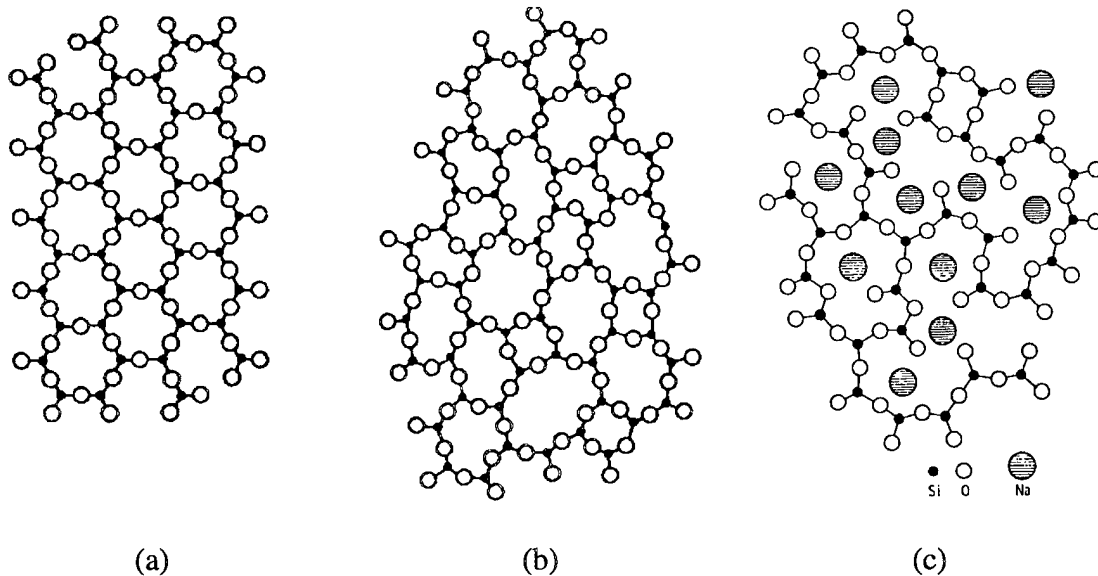
Figure 2.5 2-D representations of (a) crystalline SiO_2 structure, (b) vitreous (pure) SiO_2 glass structure, and (c) sodium-silicate glass. The fourth bond of SiO_4 tetrahedra would be into or out of the paper. (after Zachariasen[37,38]for a and b, after Warren and Biscoe[39] for (c)

the z-axis in either a clockwise or counter-clockwise direction. In figure 2.5 (b) we see a

2-D representation of vitreous (pure) silica glass. In this case a significant number of the

Si-O-Si bond angles are distorted. The distorted bond angles randomize the lattice such

that the periodicity is lost. Rings are no longer required to be 6 pairs of Si and O atoms,

but can consist of a smaller or larger number of pairs. If a network modifier such as

sodium is added to the glass composition as seen in figure 2.5 (c), the result is that some oxygen atoms have a neighbor silicon atom on one side and a sodium atom on the other, and Si-O rings are broken. Electrical conduction in silicate glass is known to be caused by ionic carriers, especially through alkali ions such as sodium.

2.2.3 Impurity and defect structures in glass

Defects resulting from the incorporation of impurities can arise in silica glasses and affect both the electrical and optical properties. There are other defects that are formed during glass manufacture or from irradiation treatment, that can also influence the optical properties of the glass.

2.2.3.1 Alkali impurity structure and non-bridging oxygens

We can represent the basic silica structure with the designation $\equiv$Si-O-Si$\equiv$. In vitreous silica, all O^{2-} ions are bridging oxygens because they are bound to two Si^{4+} ions. If an alkali oxide such as Na_2O is added to the basic structure, a significant change occurs:

$$\equiv\text{Si-O-Si}\equiv + \text{Na-O-Na} \rightarrow \equiv\text{Si-O-Na} + \text{Na-O-Si}\equiv \qquad (2.44)$$

The three parallel lines represent bonds to other oxygen atoms. Because the alkali oxide has now broken open the bridging connection to create O^{2-} ions that are bound to only one Si^{4+} ion, the alkali oxide is known as a network modifier. The SiO⁻ sites are called non-bridging oxygens and each Na^+ ion is associated with a non-bridging oxygen (NBO). The bonding of the alkali ion is mostly ionic, and it is much weaker than the Si-O bond. Besides bonding with a NBO, the alkali ion will also seek to coordinate itself with other oxygens, and as a result its coordination tendency is fulfilled by ions settling in open

50

spaces where adjacent bridging oxygens can participate in the coordination[40]. Note that H$_2$O behaves in a similar fashion; this will be discussed in section 2.2.3.3.

2.2.3.2 Influence of aluminum in SiO$_2$ structure

Aluminum is a common impurity in fused silica. The incorporation of aluminum oxide (Al$_2$O$_3$) can change the structure of silica glass. The Al^{3+} ion can form coordinations with 4 or 6 O^{2-} ions (AlO$_4$ or AlO$_6$). When added to pure SiO$_2$ glass, it is believed to coordinate itself with 6 slightly polarizable O^{2-} ions. If the glass has alkali impurities, however, the Al^{3+} can coordinate with 4 O^{2-} ions to become a AlO$_4$ tetrahedron and take the place of a SiO$_4$ tetrahedron as a "network former". It will form the tetrahedron because it can coordinate much more easily with the non-bridging oxygens that already exist due to the alkali impurity. It should be noted that when an AlO$_4$ takes the place of an SiO$_4$, AlO$_4$ is left negatively charged because the two tetrahedra have different valences. The negative charge can be compensated by a positively charged alkali ion. This can be seen in figure 2.6 where Al$_2$O$_3$ is added to SiO$_2$ with Na$^+$ impurities. Whereas there were two Na$^+$ ions bonded with negatively charged non-bridging oxygens, with the incorporation of aluminum there are two Na$^+$ ions bonded with negatively charged alumina sites. For alkali aluminosilicate glasses with large levels of alumina and alkali, if the alumina/alkali ratio is greater than one, there will not be enough alkali ions to compensate the negatively charged [AlO$_4$]$^-$. In this case the Al^{3+} ions will coordinate with 6 O^{2-} ions to form AlO$_6$ octahedra, becoming a network modifier instead of a network former. Jain and Varshneya[41] argue that in fused silica where alumina and alkali are present at the ppm level, the probability of formation of a

51

$[AlO_4]^-M^+$ complex (where M is an alkali ion) is small, so that AlO_6 modifier formation

may be probable for alumina/alkali ratios less than one. In fact, $[AlO_4]^-$, non-bridging

oxygens (SiO^-), and AlO_6 sites probably coexist over a wide range of alumina/alkali ratios

in fused silica.[41]
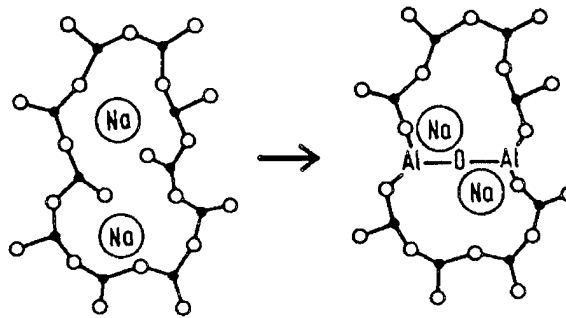
Figure 2.6   2-D schematic of the replacement of 2 SiO_2 by Al_2O_3 when Na^+ ions are present. (After Scholze[40])

2.2.3.3 Effect of water on SiO2 structure

Two of the classifications of fused silica, type II and III, are "wet" silicas, with a

large content of OH, usually present on the order of 100-1000 ppm. This is due to the

flame-fusion manufacturing process that can introduce appreciable amounts of water. It

is also well known that silica surfaces and films can become hydrated when exposed to

water. Fused silica shows an excellent resistance to water, but there is a slight, and

measurable uptake of and solubility in water. Many authors have reported measurements

of water diffusion in silica glass, including studies of diffusion as a function of

temperature and time[42-48]. They have shown that glass surfaces are much more hydrated

than the bulk. The depth of the hydration layer is dependent on temperature, water

pressure, time, and any applied stress. A recent report[49] showed that thick (50-130 μm)

hydrated layers can form under supercritical conditions (400-500 °C and 40-96 MPa

water pressure), and that it also dissolves at a constant rate. Interestingly, the thick hydrated layers were observed to be "optically anisotropic". The concentration ratio of OH/H$_2$O was observed to be 1/3 throughout the concentration profile.

The diffusion process is explained by Doremus[48] to be molecular water diffusing into the glass and then reacting with SiO$_2$ network to make hydroxyl (OH) groups, as in

$$\equiv\text{Si-O-Si}\equiv\ +\ H_2O \rightarrow \equiv\text{Si-O-H} + \text{H-O-Si}\equiv. \tag{2.45}$$
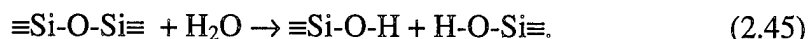
This is followed by structural relaxation. At low temperatures (below 500 °C) the reaction and relaxation are slower than the water diffusion. Others, such as Pederson[50], have proposed that the uptake of water occurs through proton transfer through the hydronium ion (H$_3$O$^+$), or equivalently, through H$_2$O + H$^+$:

$$\equiv\text{Si-O}^-...\text{Si}\equiv\ +\ H_2O + H^+ \rightarrow \equiv\text{Si-O-H} + \text{H-O-Si}\equiv + H^+. \tag{2.46}$$
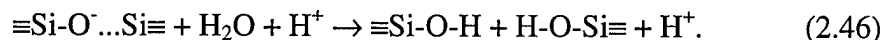
As one can see, the breaking of an O-H bond in H$_2$O is a necessary step for the reaction to proceed. Ion exchange with Na$^+$ (Pederson's observations pertained to the role of water in leaching of sodium in a sodium silicate glass) could then occur as H$^+$ reach Na$^+$ sites. For the exchange with Na$^+$ to continue, reactions such as eqn. (2.46) must continuously reoccur so that H$^+$ will move forward to expose more Na$^+$ sites. The breaking of the O-H bond could well be the velocity determining step. Interstitial molecular water, hydronium, and hydroxyl, are all various ways hydrogen may exist in glass.[48-50]

Yamamoto and Namikawa[51,52] attributed reversible changes in conductivity of both synthetic (type III) and flame fused (type II) silicas on heat treatment to the modification of hydrated surface layers. They postulated that these effects resulted from shifts in the chemical equilibrium between the water content and the silicon-oxygen bonds of the glass.

Once hydroxyl groups are formed, they can be considered free or bound to the SiO$_2$ network, depending on the presence of non-bridging oxygens. The H in OH groups can form a hydrogen bridge to an exposed non-bridging oxygen through hydrogen bonding, to the extent that non-bridging oxygens are present. This can be seen in figure 2.7, where bound and free OH groups are depicted in SiO$_2$ with Na impurities. When aluminum is present, the hydroxyl can also be found as loosely bound ions at reduced SiOAlOH sites, and as tightly bound ions at aluminosilicate sites (SiOH..Al)[53-55].
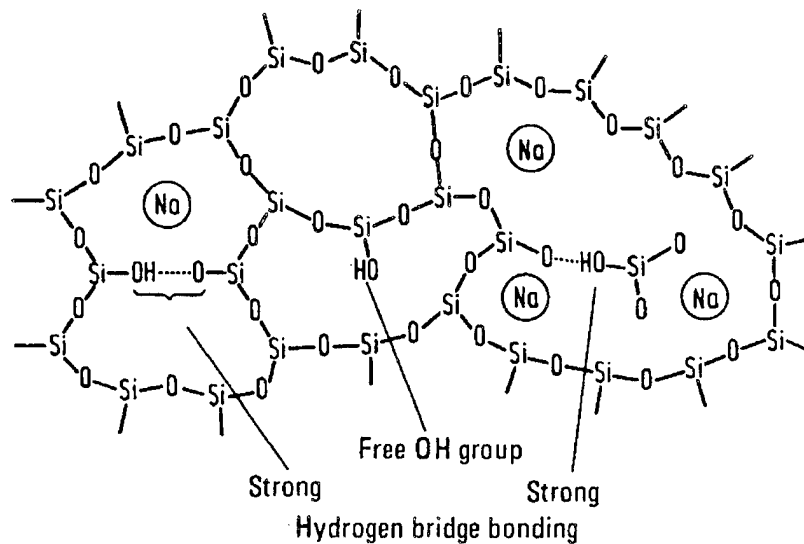
Figure 2.7 2-D schematic of various bonding configurations for OH in SiO$_2$ with Na impurities. (After Scholze[40])

2.2.3.4 Other defect structures

Besides the non-bridging oxygen defect sites which are usually associated with alkali or hydrogen impurities, there are other point defects in the network structure of vitreous SiO$_2$ (v-SiO$_2$) that can influence the optical properties of glass. Typically, v-SiO$_2$ is thought of as an insulator with a band gap of 9 eV (138 nm). Defects create gap states, and often absorption and photoluminescence peaks can be identified that

correspond to those defect states. Types III and IV fused silica are principally used in investigations on defect structures and states due to their high purity. Most information on defect structures comes from electron spin resonance (ESR) measurements. ESR measurements are only useful in detecting paramagnetic defects that have unpaired spins. Ionizing radiation such as UV laser light, x-rays and γ-rays, as well as accelerated particles are used to generate defects in fused silica for study.

The best known paramagnetic defect in vitreous silica is the E' center, and is also known as the paramagnetic oxygen vacancy V_o^+. The E' center is a silicon atom that is only bonded to three oxygen atoms, leaving an unpaired electron, denoted by $\equiv$Si·. An absorption peak at 210-215 nm (~ 5.85 eV) and a luminescence peak at ~ 290 nm (4.3 eV) have been identified with the E' center.[56] There have been diamagnetic (neutral) defect centers that have been identified as precursors of the E' center. One is the oxygen vacancy (V_o^0) given by $\equiv$Si-Si$\equiv$. Oxygen vacancies are generally believed to give rise to absorption bands at ~ 248 nm (5 eV) and at 163 nm (7.6 eV), as well as luminescences in the 282-295 nm (4.2-4.4 eV) range.[57]

The non-bridging oxygen is another commonly observed defect and can occur as a paramagnetic non-bridging oxygen hole center (NBOHC), which is denoted $\equiv$Si-O·. This can result from the breaking of a strained Si-O-Si bond:

$$\equiv\text{Si-O-Si}\equiv \rightarrow \equiv\text{Si-O}\cdot + \cdot\text{Si}\equiv \qquad (2.47)$$
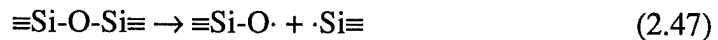
which is now associated with an E' center. The two defects occurring close together would not be detectable to ESR measurements due to dipole-dipole interactions or exchanges between the unpaired spins, so some rearranging must occur for ESR detection. Another production mechanism is the breaking of an OH bond.

$$\equiv\text{Si-OH} \rightarrow \equiv\text{Si-O}\cdot + \cdot\text{H}^0 \qquad\qquad (2.48)$$

Note that these NBOHC's are different than the charged NBO⁻ ($\equiv$Si-O⁻). In a band-gap picture of fused silica, electrons can be excited from the valence band and trapped into the hole state of a NBOHC, leading to the charged NBO⁻.[56] The NBOHC is associated with a red photoluminescence at ~ 650 nm (1.85 eV). Light between 1.9 and 5 eV can excite the photoluminescence.[56] An absorption at ~ 260 nm (4.8 eV) has been associated with the NBOHC, but it has also been associated with the peroxy radical.[57]

The peroxy radical is another oxygen-related hole center given by $\equiv$Si-O-O·, whose precursor is the peroxy bridge or linkage, given by $\equiv$Si-O-O-Si$\equiv$. The 260 nm (4.8 eV) absorption has been associated with the peroxy radical, as well as an absorption at 163 nm (7.6 eV).

2.2.3.5 Defects and SHG

Regarding the second-order nonlinearity in glass and its relation to specific defects in glass, Myers *et al.*[20] first proposed that negatively charged defects sites such as non-bridging oxygens (NBO⁻) will be exposed when sodium is depleted through conduction during the poling process. Myers[31] studied 650-nm photoluminescence (PL) associated with NBOHC's in poled and unpoled fused silica samples. He saw no difference in the PL signal for type II poled and unpoled fused silica samples, but did see a difference between heated (1000 °C) and unheated type III samples, indicating heating produces more NBOHC sites. Poled type III samples without prior heat treatment showed low SHG (~ 0.1 normal levels), while poled samples with prior heat treatment showed normal SHG levels. Other groups have shown that treatment with x-rays and γ-rays can create defects that enhance the nonlinearity in type III and IV fused silicas, with one

group suggesting that NBOHC's play the critical role.[58,59] Henry et al.[60] studied the effects of dry and wet preannealing on nonlinearity formation. They suggested that optically active hydroxyl groups ($\equiv$Si-OH) were causing the nonlinearity. They concluded this is due to the apparent role of water in the suppression of the SHG on both sides of a 600 °C annealing temperature. An increase in SHG for increasing anneal temperatures up to 600 °C was associated with creation of OH, while a decrease in SHG above 600 °C was associated with loss of OH.

It is interesting that in Ge-doped fused silica, UV photosensitivity has been correlated with defects in the glass, especially Ge-oxygen deficient centers (GODC). GODC's are similar to those considered for vitreous silica above, but their absorption in the UV is 2-3 orders greater than the absorption by the v-SiO$_2$ defects.[61]

2.2.4 Electrical properties in Glass

2.2.4.1 DC conductivity, resistivity, and mobility

Because the conductivity of glass plays a vital role in the thermal poling process, it is important to consider it here. Fused silica glass, and most glasses for that matter, are considered insulators. The conductivity of fused silica glass is very low. Nevertheless, there is some conduction. For example, at a temperature of 150°C, a type II silica glass has a typical conductivity of $\sim 10^{-17}$ Ω^{-1}cm^{-1}, whereas at 320°C, the conductivity is $\sim 10^{-11}$ Ω^{-1}cm^{-1}.[62] In glasses with large amounts of alkali oxides, the alkali ion is the mobile charge carrier with a single positive charge (cation). Indeed, when the glass contains only trace amounts of the alkali impurity, it is still believed to be the primary charge carrier.[63,64] In the study of Owen and Douglas,[63] a wide variety of fused silicas

were used with varied impurity concentrations, from sodium or potassium silicate glasses (10's of wt% impurities) to fused silica with ppm or sub-ppm sodium impurity levels. Owen and Douglas showed an approximately linear relationship between the logarithm of the resistivity and the activation energy for dc conductivity, suggesting that the conduction mechanism is the same for all silicate glasses.

The basic theory of ionic conductivity begins with an ion in a potential well and examining the probability of overcoming the potential barrier in a given thermal environment and applied field. This theory of ionic conductivity was originally applied to ionic crystals, but has subsequently been applied to glass as well, despite the lack of periodicity.[37,65,66]

Consider a one dimensional periodic well structure in which ions can move from one well to another once given enough energy. Assuming a Boltzmann distribution of energy, the probability that the ion will move to the a neighboring well is given by:

$$P = \nu e^{\varepsilon_A / kT}, \qquad (2.49)$$

where ν represents the vibrational frequency of the ion in its well, T is the temperature, and ε_A is the activation energy. Once a field is applied, the effect of the field is to lower the barrier on one side and raise it on the other. The potential well is depicted in figure 2.6, with and without field applied. If b is the distance between wells, the well will be lowered by an amount $1/2ebE$, where eE is the force on the ion. For those ions able to make it over the barrier, positive ionic movement will be to the left. The probability of
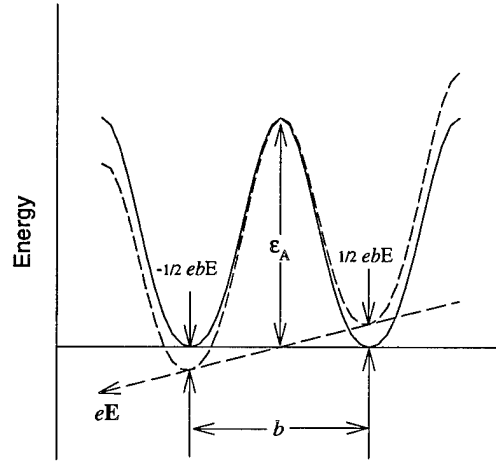
Figure 2.6 Potential well energy in glass. Solid line represents potential well without applied field. Dashed lines represent the well with an applied field.

moving to the left and right, respectively, is then:

$$P_+ = \nu\, e^{(\varepsilon_A + ebE/2)/kT}$$
$$P_- = \nu\, e^{(\varepsilon_A - ebE/2)/kT}$$

(2.50)

The net effect is that it is more probable for a positive ion to make a transition to the well

on the left. The mean drift velocity is given by

$$\overline{v} = b(P_+ - P_-)$$

(2.51)

$$= \tfrac{1}{2}bP(e^{ebE/2kT} - e^{-ebE/2kT})$$

or

$$\overline{v} = bP \sinh\!\left(\frac{ebE}{2kT}\right).$$

(2.52)

In small fields, $\sinh X = X$, so when $\tfrac{1}{2}ebE \ll kT$, equation (2.52) reduces to

$$\overline{v} = \frac{eb^2 PE}{2kT}$$

(2.53)

59

If b is estimated at ~ 35 nm (based on a 1 ppm impurity level), at a typical thermal poling temperature, 275 °C, this applies up to field strengths of ~ 300 V/cm. The current density, which is proportional to the mean drift velocity, will also be proportional to the field strength in low fields, in agreement with Ohm's law:

$$j = Ne\bar{v} = \frac{Ne^2b^2v\,e^{\mathcal{E}_A/kT}\,E}{2kT} \qquad (2.54)$$

where N is the number density of ions.

On the other hand, in very large field strengths, the exponential nature of the sinh dominates and equation (2.52) becomes

$$\bar{v} = Ce^{ebE/2kT} \qquad (2.55)$$

where C is a constant.

Using equation (2.52) for the mean drift velocity, the current density should be described by

$$j = Nebv\,e^{\mathcal{E}_A/kT}\sinh\frac{ebE}{2kT}. \qquad (2.56)$$

This equation can also be expressed in terms of an electrical conductivity given by $\sigma = j/E$.

$$\sigma = \frac{Nebv}{E}e^{\mathcal{E}_A/kT}\sinh\frac{ebE}{2kT} \qquad (2.57)$$

The exponential nature of this expression in high fields has been confirmed for a number of sodium silicate glasses.[67-69] Its applicability to fused silica, which has many orders of magnitude lower conductivity, is uncertain. I am unaware of any studies to date that have investigated this matter.

Another dependence of the conductivity is found in the Nernst-Einstein equation:

$$\sigma = \frac{Ne^2D}{kT} \qquad (2.58)$$

Here, D is the self-diffusion coefficient of the charge carrier. Investigations into the validity of this equation for glass have shown that only in exceptional cases has the measured conductivity corresponded to what was calculated from D, and that an additional factor f, where $\sigma_{exp} = f\,\sigma_{calc}$, is needed.[40] In general, for sodium silicate glasses, f values of 0.2 to 0.9 have been measured, with most around 0.5. Data gathered on D, however, has shown that the highest D values occur for alkali ions and that they generally determine the conductivity.[40]

ε_A is defined as the activation energy. The resistivity has a general Arrhenius temperature dependence given by:

$$\rho = \rho_0 e^{-\varepsilon_A/kT} \qquad (2.59)$$

Activation energies in fused silica in the range of 1.1 - 1.3 eV have been found for sodium at temperatures less than 400 °C.[63,70] Mukherjee et al.,[71] in their study on thermal poling dynamics, found Arrehenius dependencies and an activation energy for the formation of a second-harmonic signal to be 1.3 eV. Myers,[31] in a "exercised" sample with a history of multiple polings, measured activation energies for the formation to be 1.3 eV, while in an unexercised sample, he found ~ 1.5 ± 0.3 eV, suggesting that the mechanism, on initial poling, might include something other than sodium motion.

As mentioned earlier the conductivity has been shown to rely directly on the sodium impurity content.[63] The presence of other impurities can complicate matters somewhat. The relative conductivities of alkali ion impurities might be expected to be in

the order H>Li>Na>K, due to a stronger resistance to movement because of increasing radii. Besides the size of the ion, another factor determining the mobility of an ion is the strength of the bond of the ions to network sites. In general, the K^+ ion is bound more weakly, Li^+ more strongly, and H^+ with a variety of bond strengths. Therefore, a prediction of relative conductivity based on equivalent concentrations is difficult.

In fused silica glass, a relative mobility relationship was observed by Doremus[72] to be Na>Li>K in a type II and type III glass at 380 °C. The mobility is related to the conductivity by

$$\mu = \frac{\sigma}{Ne}.$$ (2.60)

In the type II (GE 204) glass, $\mu_{Li} = 0.15\mu_{Na}$ and $\mu_K < 0.002\mu_{Na}$, while in the type III (Spectrosil) glass, $\mu_{Li} = 0.03\mu_{Na}$ and $\mu_K = 0.0007\mu_{Na}$. Jain and Varshneya[41] also found a similar relationship (Na>Li>K) in a type I (GE 214) glass for temperatures below 600 °C. The initial alkali impurity content (before electrolysis) was 4 ppm and the Al_2O_3 impurity content was 61 ppm. At approximately 350 °C, they reported resistivity measurements where $\rho_{Li} \sim 13 \, \rho_{Na}$ ($\mu_{Li} \sim 0.075\mu_{Na}$) and $\rho_K \sim 2700 \, \rho_{Na}$ ($\mu_K \sim 0.0004\mu_{Na}$).

Jain and Varshneya[41] also observed a conductivity dependence on the alumina/alkali ion impurity ratio in fused silica. They pointed out that the binding energy of alkali ions to $[AlO_4]^-$ sites is significantly lower than that for non-bridging oxygen (SiO^-) sites. They measured an increase in conductivity for alumina/alkali ratios up to 8, after which there was a slight decrease, indicating the alumina had been incorporated at the majority of SiO^- sites. This is unlike alkali aluminosilicate glasses in which SiO^- sites

would disappear at an alumina/alkali ratio of 1. They also attributed a nonlinearity in

Arrhenius temperature behavior to the combined presence of SiO^- and $[AlO_4]^-$ sites.

Reported values for sodium ion mobility in different glasses, including fused

silica, vary greatly. Stagg[73] measured a sodium mobility of 5×10^{-7} $cm^2V^{-1}s^{-1}$ in SiO_2 films

at 250°C. Page et al.[74] gave a mobility of 2.1×10^{-9} $cm^2V^{-1}s^{-1}$ in soda-lime glass. Schaeffer

et al.[75] reported on the mobility of sodium ions in several types of fused silica by

examining the diffusivity of sodium in the glass. They found that the diffusivity was

lowest for high OH-containing SiO_2. Interpolating data gathered from Drury and

Roberts[76] leads to a value at 400°C of approximately 3×10^{-11} $cm^2V^{-1}s^{-1}$ for fused silica

with 150 ppm OH (e.g. Herasil) and 3×10^{-9} $cm^2V^{-1}s^{-1}$ for fused silica with 10 ppm OH

(e.g. Infrasil). By examining the rise time of the SH signal, Myers calculated an effective

Na mobility in fused silica (Optosil) of approximately 10^{-10} $cm^2V^{-1}s^{-1}$ at a temperature of

250°C, assuming a space charge density of 10^{16} ions/cm^3.[31] Shin and Tomozawa have

recently made an extensive measurement of conductivities in fused silica.[55] Interpolating

to 270°C from their data for type II fused silica, and assuming a 1 ppm carrier

concentration, we find a mobility of approximately 5×10^{-10} $cm^2V^{-1}s^{-1}$. Our recent

measurements, again assuming a constant 1-ppm ionic carrier concentration, have shown

a sample-dependent range of total mobilities on initial poling from 10^{-11} to 5×10^{-9}

$cm^2V^{-1}s^{-1}$. This range could be due to variations in either ionic or total impurity

concentrations.

It should be pointed out the introduction of water can affect the alkali ion

conductivity. Shin and Tomozawa[55] argued that alkali ions (M^+) adjacent to $[AlO_4]^-$ sites

are displaced by hydrogen. They proposed that the appropriate measure for the number

of $[AlO_4]^-M^+$ complexes is given by $R = Al/(Na+H)$. When $R < 1$, the probability for conduction through $[AlO_4]^-$ sites increases with increasing R, due to decreasing hydrogen occupation of those sites. For R > 1, the conductivity reaches a maximum and levels off or decreases. In their study, using the OH content as a measure of the amount of H, they found the expected trend, but the conductivity maximum was at R ~ 10^{-3}, instead of at unity. They suggested that this may be due to the fact that only a small fraction of the OH in glass provides H that replace alkali ions at $[AlO_4]^-$ sites. This effect of water on the alkali ion conductivity could be argued from the standpoint of a "mixed-alkali" or "mixed mobile ion" effect which will be described in section 2.2.4.4.

A study on SiO_2 films by Hofstein[77] showed interesting phenomena regarding hydrogen and sodium transport. Hofstein used capacitance experiments to study the drift/recovery of charge carriers in SiO_2 films grown on Si. Contaminants such as sodium-water and ethanol, were introduced on the film surface to measure distributions after charging. Sodium was tagged using neutron activation analysis and hydrogen motion was tagged using tritium. Although no true "bulk" values for sodium mobility in the thin film were obtained, he found that there were two general time scales that were distinguishable. First, there was a slow time scale involving the forward drift of sodium-water (hydrogen and sodium motion was indistinguishable). Ethanol contamination was used such that the interaction of ethanol with sodium in the lattice caused release of the sodium. A slow time scale was measured that included sodium recovery motion during ethanol contamimation. A fast time scale was also measured using the ethanol contamination. The fast time scale involved interface-limited hydrogen recovery and also a time component tagged as a fast sodium recovery. The hydrogen mobility was given as

64

$\mu = 40e^{(-\varepsilon_A/kT)} \, cm^2 \, V^{-1} s^{-1}$, with $\varepsilon_A \sim 0.73$ eV. This translates into a fast mobility of ~ 8 x $10^{-6} \, cm^2 \, V^{-1} s^{-1}$ for a temperature of 275 °C. It's noteworthy that recently a memory device (a non-volatile field-effect-transistor) has been demonstrated that is based on these very mobile protons in SiO_2 thin films.[78] A similar activation energy, $\varepsilon_A \sim 0.8$ eV, was found for the ionic mobility.

The reported ionic mobility of hydrogen in bulk fused silica glass varies, depending on the bonding configuration and the presence of aluminum impurities. Abe *et al.*[79] claim that hydrogen in glasses is divided into two groups of mobile and immobile hydrogen according to the strength of XOH...OX hydrogen bonding, and the mobility increases with the strength of the hydrogen bonding.

Slow hydrogen movement has been measured in bulk silica under electric fields. Slow H^+ movement could well be associated with the hydrolysis described in section 2.2.3.3. The breaking of an O-H bond in H_2O may be the rate-determining step of the hydrolysis. Hetherington *et.al.* observed high temperature (800° to 1300°C) electrolysis in fused silica and concluded that protons were injected through atmospheric moisture present at Pt electrodes.[80] Attempts at excluding water from the experiment with a dry nitrogen atmosphere only reduced injected hydrogen to one quarter of the level in normal atmosphere. The movement of hydrogen was much slower than sodium. Hetherington *et al.* extrapolated available literature data and gave the mobility ratio M between hydrogen and sodium in fused silica as $M = \mu_H / \mu_{Na} \approx 10^{-4}$. Lanford *et al.*[81] found that the best fit to data taken on diffusion (without field-assistance) of hydrogen and sodium in soda-lime

glass at 90°C is $D_H/D_{Na} = 10^{-3}$. The Nernst-Einstein relation $\mu = (eD/kT)$ implies the same ratio for the mobilities.

Carlson also studied proton injection and presented electrical-conduction and IR absorption data in soda-lime silicate glass.[82] He observed field-assisted ion exchange of protons and an ion-depletion region in the conducting glass. Abou el Leil and Snitzer investigated field-assisted ion exchange in type III fused silica using alkali-containing electrodes and concluded that the exchange they observed was protons or a hydrogenated species exchanged for alkali ions.[83] Ernsberger emphasized that hydrogen is diffused and transported into glass only as an oxygenated species such as molecular water or hydronium (H_3O^+), and not as a bare proton ion.[84,85] Lanford $et\ al.$ showed a three for one replacement of hydrogen atoms for sodium atoms in soda-lime glass, implying that hydronium was the mobile species.[81] Nogami and Abe found that proton conduction in a "wet" silica (sol-gel) glass is "water-cooperative" with the conduction process described by protons hopping between hydroxyl and water molecules, and the activated state again being H_3O^+.[86] Other observations on proton transport, conduction, and diffusion in vitreous silica have been reported.[87,88]

2.2.4.2 Glass Electrodes

There is another research field dealing with conduction in glass in which proton/hydrogen transport has been recognized as important. This field involves the ion-selective glass electrode widely used in electrochemistry. The idea that an electrical potential difference can occur between glass and a solution in contact with the glass was first proposed more than a hundred years ago by Nernst in 1892 and later experimentally

verified by Cremer in 1906.[89] A glass electrode consists of an internal reference electrode within a 50-100 μm thick glass bulb membrane containing a reactive liquid such as hydrochloric acid.[90] The glass bulb, which is commonly a lithium silicate or a lithium aluminosilicate glass, is placed in contact with an aqueous solution. The thin walls of the glass electrode act as if they were permeable to H^+ ions, although this is not strictly true. The glass surface becomes hydrated. As water diffuses into the glass, H^+ ions compete with Na^+ or Li^+ impurities in the glass for the negatively charged defect sites. Therefore, if the concentration or "activity" of hydrogen increases in the outer solution, more hydrogen enters the glass and alkali ions are displaced, causing a slight current and potential difference. The measured potential difference of the glass electrode is thus a measure of the pH of a solution.

There has been some debate over the mechanism behind the glass electrode response. There is discussion on whether or not H^+ ions really do cross the glass membrane, or if there really are mobile protons in glass. Part of the controversy is due to work by Hammond[91] who concluded that glass is not permeable to hydrogen ions from experimentation on the transfer of tritium from a tritium-marked acid solution. Baucke[89] performed migration experiments followed by concentration profiling, and found that the lithium silicate glasses could be alkali ion, proton, and mixed alkali ion-proton conductors. Field-driven ion exchange of protons for lithium ions as well as sodium for lithium was shown, depending on the pH of the solution. Abe *et al.*[92], claimed hydrogen ions are mobile, and also argues that if hydrogen ions aren't mobile, the glass will not show any pH-response.

2.2.4.3 Field-assisted ion exchange

Ion exchange is a standard method of making optical waveguides in glasses.[93,94] The process consists of immersing a glass substrate in a molten salt bath at an elevated temperature, resulting in the salt ions in the bath diffusing into the glass and exchanging with existing ionic constituents of the glass. This ion exchange can be used to increase the index of refraction of the glass in the exchanged region, forming optical waveguides. An alternative approach to ion exchange, dubbed field-assisted ion exchange, is carried out by depositing a metallic film on the glass substrate or by molten salt bath immersion along with application of an external electric field to enhance the diffusion of ions into the glass structure. The theory of field-assisted ion exchange has been analyzed in detail by Abou el Leil and Cooper.[95] Their charge exchange model was developed for alkali silicate glasses, typically borosilicates or soda-lime silicates, which typically have much higher concentrations of ionic species (e.g. 10^{21} cm^{-3}) than does fused silica (~ 10^{16} cm^{-3}). The model is based on a quasi-neutral approximation which assumes that the sum of the densities of the two ionic species is constant and independent of position during the exchange process and hence that the applied electric field is uniform across the sample. Oven et al.[96] showed that this quasi-neutrality model was a good approximation even for mobility ratios much less than one and evaluated an example for M = 1/3 (where M represents the mobility ratio of the incoming ion to that of the ion already present). As will be shown in chapter 4, this quasi-neutrality assumption is inappropriate if the mobilities of the exchanged ions are very different as in the case of Na^{+} and H_3O^{+} in

fused silica ($M \sim 10^{-4}$); the model must be modified to include the strong electric fields that form at the boundary region between the two charge carrier concentration fronts.

2.2.4.4 Mixed mobile ion effect

In glasses with high alkali content, the conductivity, or conversely the resistivity, can behave in a complicated manner when several kinds of alkali are present in the glass. In the case of a multi-alkali composition, a "mixed-alkali effect" or "mixed mobile ion (MMI) effect" is observed where the mobility of each of two ions is decreased by the addition of the other. The resistivity of mixed-alkali glasses is highest when there is a mix of two alkali ions and lower when each type of alkali ion is in greater abundance. In other words, the resistivity has a maximum when the molar fraction, x, is in-between 0 and 1, where $x = [R_2O]/([R_2O] + [M_2O])$, and R and M represent two different ions. The peak resistivity is usually around x = 0.5, but depends on glass composition.[40]

Besides alkali ions such as Li, Na, K, Rb, and Cs, H has been shown to exhibit a MMI effect. Tomozawa and Takata[97] showed that when water was dissolved in alkali silicate glasses, the resistance increased. A peak resistance was reached at ~ 0.25 $[H_2O]/([H_2O]+[Na_2O])$. Tomozawa and Takata also estimated a high resistivity layer to occur where the hydrogen and sodium layers intersect. Schaeffer *et al.*[98] reported that the Na diffusivity, as measured using ^{22}Na as a radiotracer, is reduced in fused silica with high OH content and argued that the mixed-alkali effect was responsible. They further argued, based on extrapolated data from Drury and Roberts[99], that the electrical current is carried by H^+ ions in high OH glasses and by Na^+ ions in low OH glasses. This should be contrasted with the results found by Shin and Tomozawa[55], who found changes in water

69

content produced different effects on conductivities of different types of glasses; the conductivity of type I silica glass increased slightly while that of type IV silica glass decreased with increasing water content. They attributed the differing trends to different alumina content as discussed in section 2.2.4.1.

It is interesting to note that even a slight addition of minority ions with low mobility can cause a decrease in the mobility of the host ions.[40,100] For example, replacing one ion can influence the mobility of 50 host ions. Another notable item is that the MMI effect is weakened with decreasing alkali oxide and is believed to disappear with alkali oxide content below 10 mole percent (e.g. for fused silica).[101]

There are many theories and interpretations regarding the mixed-alkali effect, I will not attempt to survey this area. Two early papers that review the mixed alkali effect up to the time that they were written are by Isard[101] and Day[102]. Some more recent introductions into the various theories are given in references 40,100, and 103. Early proposals dealt with linking of ion pairs and limited neighborhoods, but later ideas have taken into consideration transport in pathways, glass structure, and correlated motions. For example, the model proposed by Matusita et al.[104] assumes that an ion can only move in transport paths that have empty spaces where ions of the same kind previously occupied. The replacement of host ions with minority ions dilutes the number of nearby vacant sites of similar ions thus diluting (or "clogging") the number of pathways. In reviewing models, Kahnt[100] says there are two fundamental conditions that arise from a general theoretical statistical mechanics treatment of path probability: (1) transport involves diffusion paths with low connectivity (percolation) and (2) there is an effective

attractive interaction between unlike ions. He says that percolation is generally accepted, but the mechanism behind the attractive interaction is still debated.

Recently, models have been introduced that consider the characteristic environment that exists for one ion type versus another type.[105] If one ion takes over a site originally occupied by the other type, there is a mismatch in energy that the new ion has to overcome through structural relaxation, thus reducing the total energy available and the hopping rate as a consequence. Another approach[100] hypothesizes stronger bonding in configurations with mixed alkali ions on neighboring polar sites than those with single alkali bonding, leading to low mobility and blocked pathways. The stronger bonding is derived from the idea that the presence of different ions on the neighboring polar sites allows an additional degree of freedom which the structure can use to minimize energy, and that identical ions on neighboring sites requires more energy.

2.2.4.5 Dielectric response and ac polarization

Dielectric properties of fused silica are another important area of interest which hold clues to structural behavior. The dielectric response of a glass depends on the short-range motion of charge carriers, and therefore varies with electric field frequency, field strength and other electrical properties. Charge motion can lead to storage of electrical energy and thus to capacitance. The capacitance of a parallel-plate capacitor with a dielectric material between the plates is given from electro-statics as

$$C = Q/V = \frac{\varepsilon(V/d)A}{V} = \frac{\varepsilon A}{d} \qquad (2.61)$$

71

where Q is the charge density on the plates, V is the applied potential difference, A is the area of the plates, d is the distance between the plates, and ε is the permittivity of the material between the plates. When an electric field is applied to the plates, charges are displaced in response to the electric field, resulting in different kinds of polarization. Space-charge or interfacial polarization results from dc conduction of mobile carriers and will be discussed in detail in chapter 5 as the originating source of the second-order nonlinearity in fused silica. Other polarizations can occur as well, such as electronic, atomic, and dipole polarizations. These all involve short-range motion, are frequency dependent, and contribute to the overall linear polarization of the material. In a linear and isotropic medium the electric displacement D is related to the electric field and polarization by

$$D = \varepsilon E = E + 4\pi P \qquad (2.62)$$

In an alternating field, there is generally a phase difference between E and D (or E and P).

$$\begin{aligned} E^* &= E_0\, e^{-i\omega t} \\ D^* &= D_0 e^{-i(\omega t - \delta)} \end{aligned} \qquad (2.63)$$

where δ is the phase difference and ω is the angular frequency. With $D^* = \varepsilon^* E^*$, the permittivity is now complex and given by

$$\varepsilon^* = \varepsilon_{dc}\, e^{i\delta} = \varepsilon_{dc}\cos\delta + i\varepsilon_{dc}\sin\delta = \varepsilon' + i\varepsilon'' \qquad (2.64)$$

ε' (or $k' = \varepsilon'/\varepsilon_0$) is called the dielectric constant and ε'' (or $k'' = \varepsilon''/\varepsilon_0$) is the dielectric loss factor.

The ratio of loss factor to the dielectric constant is

$$\tan\delta = \frac{\varepsilon''}{\varepsilon'} = \frac{k''}{k'} \qquad (2.65)$$

tan δ is sometimes called the loss angle or dissipation factor, and is used as a measure of dielectric loss or absorption.

When the dielectric constant and loss angle are measured as a function of frequency in a dielectric there are often distinct resonances.[66] Resonance at very high frequencies (10^{15} Hz) is due to electron polarization, or the shift of the electron clouds of atoms (a vibrational frequency). The displacement of positive and negative ions (such as in an Si-O bond) with respect to each other is atomic polarization, and occurs at a frequency in the infrared range (10^{12}-10^{13} Hz) at a resonance characteristic of the bond strength.

In the 10^{11}-10^{12} Hz infrared range high frequency dipolar polarization occurs. An example of dipolar polarization is what are termed "Stevels deformational losses" such as the oscillation of a Si-O-Si bond about an equilibrium position (a type of rotational frequency). Most Si-O-Si bonds in the glass network are found to be in a skewed gaussian distribution centered at 144° with a half breadth of 35°.[106] About 10% of the bond angles lie between 175°-180°. It is these nearly collinear bonds that can oscillate. Another example of Stevels deformational loss is the oscillation of an OH⁻ group about an equilibrium position.

Low frequency dipolar polarization in dielectrics can occur in the frequency range of 10^3-10^6 Hz at room temperature. This type of polarization concerns the orientation or alignment of dipoles in an equilibrium position. Orientational polarization occurs as a

result of the motion of charged ions between interstitial positions within the structure of the dielectric. This type of polarization from dipole orientation is a possible contributor to the second-order nonlinearity in fused silica as mentioned in section 2.1.7. An example of orientational polarization of a dipole is shown in figure 2.7. Here a cation that is attached to a non-bridging oxygen moves to a new equilibrium position in an applied field. According to Charles[107], an alkali cation will respond to an electric field with two major types of motion regarding polarization and conduction: (1) the alkali ion will oscillate between equivalent equilibrium positions about the same non-bridging oxygen, leading to ac polarization, and (2) the alkali ion will drift to a new non-bridging oxygen, which involves both ac polarization and dc conduction.
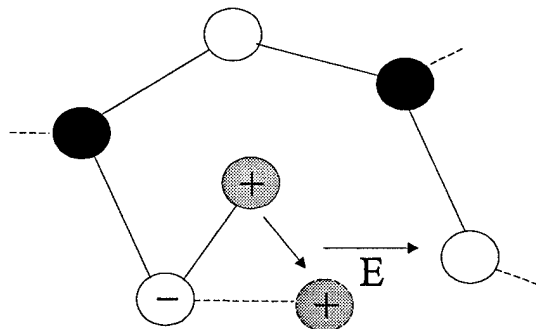
Figure 2.7 Low frequency cation dipole. Black-filled circles are Si, open circles are O, and gray-filled circles are the cation.

Mable and McCammon[108] studied dielectric loss that occurs at audio frequencies at cryogenic temperatures in fused silica, and two loss peaks were observed. One peak is associated with the Si-O-Si Stevels deformational loss which shifts to 10^{11}-10^{12} Hz at room temperature. The other peak can be related to the OH content of the glass. Several different types of fused silica, with OH content ranging from 20 ppm to 1190 ppm were measured, and the peak showed an increase in loss with increasing OH content. The peak is reported to be an oscillating dipole of the type described for the orientation cation

dipole and is evidence that the H^+, acting as a cation and bound to SiO^-, can show dipole

orientation in an applied field.

2.3 References

[1] A. Yariv, *Optical Electronics* (Fourth Edition, Saunders College Publishing, Philadelphia, 1991).

[2] P.A. Franken, A.E. Hill, C.W. Peters, and G. Weinreich, "Generation of optical harmonics," Phys. Rev. Lett. **7**, 118 (1961).

[3] R.W. Boyd, *Nonlinear Optics* (Academic Press, San Diego, 1992).

[4] J.A. Armstrong, N. Bloembergen, J. Ducuing, and P.S. Pershan, "Interactions between light waves in a nonlinear dielectric," Phys. Rev. **127**, 1928 (1962).

[5] M.M. Fejer, G.A. Magel, D.H. Jundt, and R.L. Byer, "Quasi-Phase-Matched Second Harmonic Generation: Tuning and Tolerances," IEEE J. Quan. Electron. **28**, 2631 (1992).

[6] U. Osterberg and W. Margulis, "Dye laser pumped by Nd:YAG laser pulses frequency doubled in glass optical fiber," Opt. Lett. **11**, 516 (1986).

[7] R.H. Stolen and H.W.K. Tom, "Self-organized harmonic generation in optical fibers," Opt. Lett. **12**, 585 (1987).

[8] B.Ya. Zel'dovich and A.N. Chudinov, "Interference of fields with frequencies ω and 2ω in external photoelectric effect," JETP Lett. **50**, 439 (1989).

[9] E.M. Dianov, P.G. Kazansky, and D.Yu. Steponov, "Problem of the photoinduced second harmonic generation," Sov. J. Quantum Electron. **19**, 575 (1989).

[10] E.V. Anoikin, E.M. Dianov, P.G. Kazansky, and D.Yu. Stepanov, "Photoinduced second harmonic generation in gamma-ray-irradiated optical fibers," Opt. Lett. **15**, 834 (1990).

[11] D. Anderson, V. Mizrahi, and J.E. Sipe, "Model for second-harmonic generation in glass optical fibers based on asymmetric photoelectron emission from defect sites," Opt. Lett. **16**, 796 (1991).

[12] R. Kashyap, G.J. Veldhuis, D.C. Rogers, and P.F. Mckee, "Phase-matched second-harmonic generation by periodic poling of fused silica," Appl. Phys. Lett. **64**, 1332 (1993).

[13] D. Statman and J.A. Georges III, "Charge dynamics and poling in glass waveguides," J. Appl. Phys. **80**, 654 (1996).

[14] P.G. Kazansky, V. Pruneri, and P.St.J. Russell, "Blue-light generation by quasiphase-matched frequency doubling in thermally poled optical fibers," Opt. Lett. **20**, 843 (1995).

[15] V. Pruneri and P.G. Kazansky, "Frequency doubling of picosecond pulses in periodically poled D-shape silica fibre," Electron. Lett. **33**, 318 (1997).

[16] V. Pruneri and P.G. Kazansky, "Electric-field thermally poled optical fibers for quasi-phase-matched second-harmonic generation," IEEE Photon. Tech. Lett. **9**, 185 (1997).

[17] V. Pruneri, G. Bonfrate, P.G. Kazansky, C. Simonneau, P. Vidakovic, and J.A. Levenson, "Efficient frequency doubling of 1.5 mm femtosecond laser pulses in quasi-phase-matched optical fibers," Appl. Phys. Lett. **72**, 1007 (1998).

[18] M. Eich, A. Sen, H. Looser, G.C. Bjorklund, J.D. Swalen, R. Twieg, and D.Y. Yoon, "Corona poling and real-time second-harmonic generation study of a novel covalently functionalized amorphous nonlinear optical polymer," J. Appl. Phys. **66**, 6 (1989)

[19] W.L. Bond, "The mathematics of the physical properties of crystals," Bell Sys. Tech. J., **22**, 1 (1943).

[20] R.A. Myers, N. Mukherjee and S.R.J. Brueck, "Large second-order nonlinearity in poled fused silica," Opt. Lett., **16**, 1732 (1991).

[21] P.N. Butcher and D. Cotter, The Elements of Nonlinear Optics (Cambridge University Press, Cambridge, 1990), p. 26

[22] S. Keilich, "Optical second-harmonic generation by electrically polarized isotropic media," IEEE J. Quantum Electron. **QE-5**, 562 (1969).

[23] A.C. Liu, M.J.F. Digonnet, and G.S. Kino, "A DC Kerr measurement in a silica channel waveguide," in: *Doped Fiber Devices*, M.J.F. Digonnet and F. Ouellette, eds., SPIE Proc. Vol. **2841**, 209 (1996).

[24] K.S. Kim, R.H. Stolen, W.A. Reed, and K.W. Quoi, "Measurement of the nonlinear index of silica-core and dispersion-shifted fibers," Opt. Lett. **19**, 257 (1994).

[25] A. Feldman, D. Horowitz, and R.M. Waxler, "Mechanisms for self-focusing in optical glasses," IEEE J. Quantum Electron. **QE-9**, 1054 (1973).

[26] M.D. Levenson, "Feasibility of measuring the nonlinear index of refraction by third-order frequency mixing," IEEE J. Quantum Electron. **QE-10**, 110 (1974).

[27] M. Paillette and D. Vautier, "Mesures de l'effet kerr dans differents verres optiques," Opt. Commun. **4**, 292 (1971).

[28] Quartz glass for optical data and properties, Hereaus Amersil Inc., 3473 Satellite Boulevard, Duluth, GA 30136-5821.

[29] N. Mukherjee, R.A. Myers and S.R.J. Brueck, "Dynamics of second harmonic generation in fused silica," J. Opt. Soc. Am. B **11**, 665 (1994).

[30] K.D. Singer, M.G. Kuzyk, and J.E. Sohn, "Second-order nonlinear-optical processes in orientationally ordered materials: relationship between molecular and macroscopic properties," J. Opt. Soc. Am. B **4**, 968, (1987).

[31] R.A. Myers, *Large Second-Order Nonlinearity in Amorphous SiO₂ Using Temperature/Electric-Field Poling*, Ph.D. Dissertation, University of New Mexico (1995).

[32] P.G. Kazansky and P.St.J. Russell, "Thermally poled glass: frozen-in electric field or oriented dipoles?," Opt. Commun. **110**, 611 (1994).

[33] M.J. Weber, ed., *CRC Handbook of Laser Science and Technology Volume III: Optical materials,* part 1, (CRC Press, New York, 1986).

[34] M. Eich, A. Sen, H. Looser, G.C. Bjorklund, J.D. Swalen, R. Twieg, and D.Y. Yoon, "Corona poling and real-time second-harmonic generation study of a novel covalently functionalized amorphous nonlinear optical polymer," J. Appl. Phys. **66**, 6 (1989).

[35] A.J. Marker III and N. Neuroth, "Overview - optical glass: an engineered material," in *The Properties of Optical Glass,* H. Bach and N. Neuroth eds., 1 (Springer-Verlag, New York, 1995).

[36] I. Fanderlik, ed., *Silica Glass and Its Application,* (Elsevier Science Publishing, New York, 1990).

[37] W.H. Zachariasen, "The atomic arrangement in glass," J. Am. Chem. Soc., 54, 3841 (1932).

[38] A.E. Owen, "Electric conduction and dielectric relaxation in glass," in: *Progress in Ceramic Science Vol.3,* J.E. Burke, ed., 77 (Pergamon Press, Oxford, 1963).

[39] B.E. Warren and J. Biscoe, J. Am. Ceram. Soc. **21**, 259 (1938).

[40] H. Scholze, *Glass: Nature, Structure, and Properties,* (Springer-Verlag, New York, 1990).

[41] V. Jain and A.K. Varshneya, "Ionic conductivity in fused silica: II, Steady-state behavior," J. Am. Ceram. Soc. **73**, 409 (1990).

[42] K.M. Davis and M. Tomozawa, "An infrared spectroscopic study of water-related species in silica glass," J. Non-Cryst. Solids **201**, 177 (1996).

[43] H. Wakabayashi and M. Tomozawa, "Diffusion of water into silica glass at low temperature," J. Am. Ceram. Soc. **72**, 1850 (1989).

[44] A. Agarwal, M. Tomozawa, and W.A. Lanford, "Effect of stress on water diffusion in silica glass at various temperatures," J. Non-Cryst. Solids **167**, 139 (1994).

[45] O. Dersch, A. Zouine, F. Rauch and E. Arai, "Diffusion of water into quartz and silica glass," Mat. Sci. Forum **248-249**, 389 (1997).

[46] D.D. Allred, C.W. White, G.J. Clark, B.R. Appleton, and I.S.T. Tsong, "Measurement of hydrogen profiles in SiO_2 with a nuclear reaction technique," in *The Physics of SiO$_2$ and its Interfaces*, S.T. Pantelides, ed., 210 (Pergamon Press, New York, 1978).

[47] M. Helmich and F. Rauch, "On the mechanism of diffusion of water in silica glass," Glastech. Beriche **66**, 195 (1993).

[48] R.H. Doremus, "Diffusion of water in silica glass," J. Mater. Res. **10**, 2379 (1995).

[49] N. Yanagisawa, K. Fujimoto, S. Nakashima, Y. Kurata, and N. Sanada, "Micro FT-IR study of the hydration layer during dissolution of silica glass," Geochim.Cosmochim. Acta **61**, 1165 (1997).

[50] L.R. Pederson, "Comparison of sodium leaching rates from a Na_2O-SiO_2 glass in H_2O and D_2O," Phys. Chem. Glasses 28, 17 (1987).

[51] K. Yamamoto and H. Namikawa, "The irreversible and reversible changes in silica glasses observed by electrical properties (part I) - synthetic silica glass by flame fusion," J. Ceram. Soc. of Japan (Intl. Ed.) **102**, 656 (1994).

[52] K. Yamamoto and H. Namikawa, "The irreversible and reversible changes in silica glasses observed by electrical properties (part II) - quartz glass by flame fusion," J. Ceram. Soc. of Japan (Intl. Ed.) **103**, 897 (1995).

[53] R.H. Doremus, "Ionic transport in amorphous oxides," J. Electrochem. Soc.: Solid State Science, 181 (1968).

[54] S.R. Hofstein, "Proton and sodium transport in SiO_2 films", IEEE Trans. Elec. Dev., **ED-14**, 749 (1967).

[55] D.W. Shin and M. Tomozawa, "Effects of fictive temperature and water content on electrical conductivity of silica glasses", J. Non-Cryst. Solids **203**, 262 (1996).

[56] E.P. O'Reilly and J. Robertson, "Theory of defects in vitreous silicon dioxide," Phys. Rev. B 27, 3780 (1983).

[57] D.L. Griscom, "Optical properties and structure of defects in silica glass," J. Ceram. Soc. Japan **99**, 10 (1991).

[58] K. Tanaka, K. Kashima, K. Hirao, N. Soga, S. Yamagata, A. Mito, and H. Nasu, "Effect of γ-irradiation on optical second harmonic intensity of electrically poled silica glass," Jpn. J. Appl. Phys. **34**, 173, (1995).

[59] A. Kameyama, E. Muroi, A. Yokotani, K. Kurosawa, and P.R. Herman, "X-ray radiation effects on second-harmonic generation in thermally poled silica glass," J. Opt. Soc. Am. B **14**, 1088 (1997).

[60] L.J. Henry, A.D. DeVilbiss, and T.E. Tsai, "Effect of preannealing on the level of second-harmonic generation and defect sites achieved in poled low-water fused silica," J. Opt. Soc. Am. B **12**, 2037, (1995).

[61] V.B. Neustruev, "Colour centres in germanosilicate glass and optical fibres," J. Phys.: Condens. Matter **6**, 6901 (1994).

[62] D.W. Shin and M. Tomozawa, "Electrical and dielectric relaxation in silica glasses at low temperature," J. Non-Cryst. Solids **211**, 237 (1997).

[63] A.E. Owen and R.W. Douglas, "The electrical properties of vitreous silica," J. Soc. Glass Tech. **43**, 159T (1959).

[64] R.H. Doremus, "Electrical conductivity and electrolysis of alkali ions in silica glass," Phys. Chem. Glasses **10**, 28 (1969).

[65] J.J. O'Dwyer, *The Theory of Electrical Conduction and Breakdown in Solid Dielectrics*, (Clarendon Press, Oxford, 1973).

[66] L.L. Hench and J.K. West, *Principles of Electronic Ceramics* (John Wiley & Sons, New York, 1990).

[67] R.J. Maurer, "Deviations from Ohm's law in soda lime glass," J. Chem. Phys. **9**, 579 (1941).

[68] J. Vermeer, "The electrical conduction of glass at high field strengths," Physica **22**, 1257 (1956).

[69] D.E. Carlson, "Ion depletion at a blocking anode: I, Theory and experimental results for alkali silicate glasses," J. Am. Ceram. Soc. **57**, 291 (1974).

[70] R.H. Doremus, "Electrical conductivity and electrolysis of alkali ions in silica glass," J. Amer. Ceram. Soc. **43**, 173 (1960).

[71] N. Mukherjee, R.A. Myers and S.R.J. Brueck, "Dynamics of second harmonic generation in fused silica," J. Opt. Soc. Am. B **11**, 665 (1994).

[72] R.H. Doremus, "Electrical conductivity and electrolysis of alkali ions in silica glass," Phys. Chem. Glasses **10**, 28 (1969).

[73] J.P.Stagg, "Drift mobilities of Na^+ and K^+ ions in SiO_2 films," Appl. Phys. Lett 31 (1977) 532.

[74] M.C. Page, R. Oven, and D.G. Ashworth, "Scaling rules for glass based planar optical waveguides made by field assisted ion diffusion," Electron. Lett. 27 (1991) 2073.

[75] H.A. Schaeffer, J. Mecha, and J. Steinmann, "Mobility of sodium ions in silica glass of different OH content," J. Am. Ceram. Soc. 62 (1979) 343.

[76] T. Drury and J.P. Roberts, "Diffusion in silica glass following reaction with tritiated water vapour," Phys. Chem. Glasses 4 (1963) 79.

[77] S.R Hofstein, "Proton and sodium transport in SiO_2 films," IEEE Trans. Elect. Dev. **ED14**, 749 (1967).

[78] K. Vanheusden, W.L. Warren, R.A.B. Devine, D.M. Fleetwood, J.R. Schwank, M.R. Shaneyfelt, P.S. Winokur, and Z.J. Lemnios, "Non-volatile memory device based on mobile protons in SiO2 thin films," Nature **386**, 587 (1997).

[79] Y. Abe, H. Hosono, W.H. Lee, and T. Kasuga, "Electrical conduction due to protons and alkali-metal ions in oxide glasses," Phys. Rev B. **48**, 15621 (1993).

[80] G. Hetherington, K.H. Jack and M.W. Ramsay, "High temperature electrolysis of vitreous silica: I," Phys. Chem. Glasses **6**, 6 (1965).

[81] W.A.Lanford, K.Davis, P. Lamarche, T. Laursen, R. Groleau, and R.H. Doremus, "Hydration of soda-lime glass," J. Non-Cryst. Solids **33**, 249 (1979).

[82] D.E. Carlson, "Anodic proton injection in glasses," J. Am. Ceram. Soc. **57**, 461 (1974).

[83] M. Abou el Leil and E. Snitzer, "Field-assisted ion exchange in type III silica," Comm. Am. Ceram. Soc. C-250 (1984).

[84] F.M. Ernsberger, "The role of molecular water in the diffusive transport of protons in glasses," Phys. Chem. Glasses **21**, 146 (1980).

[85] F.M. Ernsberger, "The nonconformist ion," J. Am. Ceram. Soc. **66**, 747 (1983).

[86] M. Nogami and Y. Abe, "Evidence of water-cooperative proton conduction in silica glasses," Phys. Rev. B **55**, 12108 (1997).

[87] V. Garino Canina and M. Priqueler, "Diffusion of protons in $SiO_2 + Al_2O_3$ glass in an electrical field," Phys. Chem. Glasses **3**, 43 (1962).

[88] P.J. Jorgenson and F.J. Norton, "Proton transport during hydrogen permeation in vitreous silica," Phys. Chem. Glasses **10**, 23 (1969).

[89] F.G.K. Bauke, "The modern understanding of the glass electrode response," Fresenius J. Anal. Chem. **349**, 582 (1994).

[90] K.B. Oldham and J.C. Myland, *Fundamentals of Electrochemical Science* (Academic Press, San Diego, 1994).

[91] P.R. Hammond, Chem. Ind. **17**, 311 (1962).

[92] Y. Abe, M. Nogami, and M. Maeda, "Mobile hydrogen ion in glass to enable pH-measurement," J. Non-Cryst. Solids **209**, 204 (1997).

[93] R.V. Ramaswamy and R. Srivastava, "Ion-exchanged glass waveguides: A review," J. Lightwave Tech. **6**, 984 (1988).

[94] M.. Abou el Leil, "Ion exchange in glasses and crystals," Annu. Rev. Mater. Sci. **23**, 255 (1993).

[95] M. Abou el Leil and A.R. Cooper, "Analysis of field-assisted binary ion exchange," J. Am. Ceram. Soc. **62**, 390 (1979).

[96] R. Oven, D.G. Ashworth, and M.C. Page, "On the analysis of field-assisted ion diffusion into glass," J. Phys. Condens. Matter **4**, 4089 (1992).

[97] M. Tomozawa and M. Takata, "Electrical resistivity of glass surface reacted with water," J. Non-Cryst. Solids **45**, 141 (1981).

[98] H.A. Schaeffer, J. Mecha, and J. Steinmann, "Mobility of sodium ions in silica glass of different OH content," J. Am. Ceram. Soc. **62**, 343 (1979).

[99] T. Drury and J.P. Roberts, "Diffusion in silica glass following reaction with tritiated water vapour," Phys. Chem. Glasses **4**, 79 (1963).

[100] H. Kahnt, "Ionic transport in glasses," J. Non-Cryst. Solids **203**, 225 (1996).

[101] J.O. Isard, "The mixed alkali effect in glass," J. Non-Cryst. Solids **1**, 235 (1969).

[102] D.E. Day, "Mixed alkali glasses - their properties and uses," J. Non-Cryst. Solids **21**, 343 (1976).

[103] M.D. Ingram, "Ionic conductivity in glass," Phys. Chem. Glasses **28**, 215 (1987).

[104] K. Matusita, S. Takayama, and S. Sakka, "Electrical conductivities of mixed cation glasses," J. Non-Cryst. Solids **40**, 149 (1980).

[105] J.E. Davidson, M.D. Ingram, A. Bunde, and K. Funke, "Ion hopping processes and structural relaxation in glass materials," J. Non-Cryst. Solids **203**, 246 (1996).

[106] R.L. Mozzi and B.E. Warren, Appl. Cryst. **2**, 164 (1969).

[107] R.J. Charles, "Some structural and electrical properties of lithium silicate glasses," J. Am. Ceram. Soc. **46**, 235.

[108] S.H. Mable and R.D. McCammon, "The dielectric loss of fused silica at low temperatures," Phys. Chem. Glasses **10**, 222 (1969).

Chapter 3. Thermal poling of bulk fused silica

Since 1991, when second-harmonic generation (SHG) from thermally poled fused silica was first reported by Myers *et al.* [1], many groups have continued to make contributions toward understanding this phenomenon. In the first paper, it was shown in bulk fused silica that the second-order nonlinearity occurs in a thin layer under the anode. Various studies have subsequently shown that the peak is buried under the surface, and that the extent of the nonlinear region is ~ 5 to 15 μm. Notwithstanding these observations, no mechanism other than field-driven migration of positively charged sodium ions causing a negative space-charge region has been proposed. There are still unknowns, such as: What is the electric field distribution? What is the charge concentration profile? Does it reach a short-term steady state? Is sodium the only charge carrier? What plays the role of charge carrier in sodium-free glass such as thin films and fibers? Why does the formation of the nonlinearity have multiple time scales depending on poling history as documented below? Does the poling environment or do external contaminants play a role in nonlinearity formation? These are the questions that I will attempt to address by experimental observation recorded in this chapter and through modeling and simulation in chapter 4. These questions and answers will hopefully provide advancement toward the larger question: Is there a way to control and increase the nonlinearity?

The first section of this chapter will review SHG measurements in bulk fused silica. This will cover processing, Maker fringe and peak SH measurement, $\chi^{(2)}$

calculation, *in situ* SHG and electrical current observations. The second section consists of space-charge profiling experiments. The experiments include etching, atomic force microscope (AFM), and secondary ion mass spectroscopy (SIMS) measurements. The third section will address experimental evidence of introduction of water into the space charge region during the poling process. Table 3.1 shows a summary of the various experiments reported in this chapter and the figures associated with those experiments. Glass names and types are also shown.

3.1 SHG & Current measurements

3.1.1 *Ex situ* poling and measurement

Ex situ poling is defined here as the process of applying voltage to heated samples, cooling samples with voltage applied, and then removing the samples for second harmonic measurement. The poling treatment and measurement process described in this section are basically the same as used in earlier work done by our group. The discussion here is provided to start on common ground and set the stage for further experimental work described in later sections.

3.1.1.1 *Poling process and Maker fringe setup*

Our samples of fused silica were commercially available and purchased from glass manufacturers or distributors. They came as ground and polished optically-flat windows or plates and were ordered in various thicknesses from ~ 170 μm to 10 mm. Two types of fused silica were examined: type II, a high-OH natural fused silica and type

Glass Supplier	Name	Type	Thickness (mm)	Ex-situ SH	In-situ dynamic second harmonic (SH) & conductivity (σ)				Nonlinearity Profiling		
				Maker fringe & peak SH (Fig. #)	Initial poling (Fig. #)	Short to Ground (Fig. #)	Repoling (Ground to V) (Fig. #)	Field Reversal (V to -V) (Fig. #)	Etching (Fig. #)	SIMS (Fig. #)	FTIR (Fig. #)
Heraeus	T08	II	~ 0.17	3.3	3.22 (σ)				3.18-21 3.23-24	3.26-30	3.34
Heraeus	Herasil	II	5		3.13(σ)	3.10 (SH&σ)	3.10 (SH&σ)	3.14-16 (SH) 3.17 (SH&σ) 3.13 (σ)			
Esco	G1	II	1.6	3.3						3.35-37 (with D)	
Esco	G1	II	6		3.9 (SH&σ) 3.12 (SH&σ)	3.11(SH&σ)	3.11 (SH&σ) 3.12 (SH&σ)				
Esco	S1-UV	III	~ 0.17	3.3					3.25	3.33	
Corning	Seacor	II	5.9							3.32	

Table 3.1 A tabulated list of figures shown for experiments performed and types of glass used in those experiments.

III, a high-OH synthetic fused silica. Most measurements were made with type II glass such as Herasil or T08 from Heraeus Amersil or G1 from Esco Products.

Samples were simply pressure contacted by two electrodes, which were typically made from aluminum foil. The samples were placed in an oven which was subsequently heated to an appropriate temperature for poling. This is shown schematically in figure 3.1.
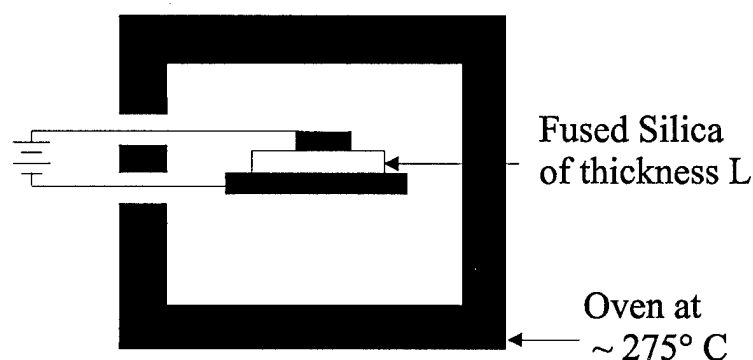

Fused Silica
of thickness L

Oven at
~ 275° C

Figure 3.1 Basic poling setup

This oven temperature was typically close to 275 °C, which was found to be the optimum poling temperature in previous studies done by our group. The poling environment would either be ambient atmosphere for poling in a large oven, or controlled gas flow such as N_2 for a smaller poling chamber. The smaller poling chamber will be described in detail in the next section. A potential difference was then applied across the electrodes. The "top" electrode would act as the active electrode, while the "bottom" electrode was connected to ground. Voltages up to 5 kV could be applied to the top electrode, and could be either positive or negative. For thin (~ 170 μm) cover slip samples, large voltages required insertion of a piece of soda-lime glass (microscope slide) between the sample and the ground electrode to act as a current limiter and avoid dielectric breakdown. Only positive voltages were applied to the top electrode on the

86

cover slips on soda-lime glass to ensure that the positively charged sodium ions traveled away from the top electrode and towards the ground electrode and not into the cover slip. At temperature, the soda-lime glass has a conductivity several orders of magnitude greater than fused silica, causing a negligible voltage drop when placed between ground and the glass sample. After the voltage was switched on, the sample was poled for a set time, and then allowed to cool with the voltage still applied. The cooling in the large oven was accomplished by opening the oven door and turning off the heat, exposing the sample to room temperature ambient. Under this poling environment, samples typically cooled from 275 to 200 °C in one minute, at which point the current through the sample is typically reduced by an order of magnitude or more. In the smaller poling chamber, cooling occurred by turning off the heat and allowing continued gas flow. The cooling rate is slower in the smaller chamber, typically cooling from 275 to 200 °C in ~ 10 minutes. This could be increased somewhat by increasing gas flow to the chamber.

After samples were cooled, the electrodes were removed, and the second harmonic (SH) signal was examined by placing the samples into a Q-switched Nd:YAG laser beam (1.06 μm) and measuring the SH signal at 532 nm. The measurement station was laid out to allow Maker fringe measurement through computer control, or more simply, measurement of the peak SH signal by manual rotation of the sample in the laser beam. Figure 3.2 shows a schematic of this measurement station.
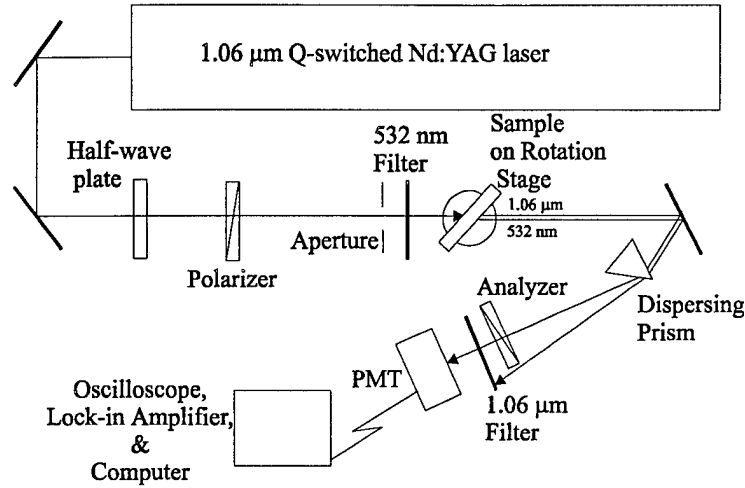
Figure 3.2 Schematic of Maker fringe/SHG peak measurement setup.

3.1.1.2 Maker fringe measurement

By rotating the sample in the laser beam, the SHG as a function of angle can be measured. This is known as a Maker fringe measurement after P.D. Maker[2], and is a valuable diagnostic technique.

Maker fringes can be understood as a combination of two different processes, phase-matching interference and Fresnel surface reflectivity. Recall from eqn. 2.32, the second harmonic intensity is proportional to a phase mismatch factor (assuming a constant $\chi^{(2)}$)

$$I_{2\omega} = f(\theta) \frac{\sin^2 \frac{\Delta k d}{2}}{\Delta k^2} \tag{3.1}$$

d is the nonlinearity thickness and $\Delta k = \pi/l_{coh}$. When a sample is rotated in a laser beam the function $f(\theta)$ includes several factors and can be written as[3]

$$f(\theta) = C \cos(\theta) \sin^2(\theta) T_{in,\omega}^2(\theta) T_{out,2\omega}(\theta) \tag{3.2}$$

where C is a constant. Fresnel coefficients can be used to describe intensity behavior at the air-glass and glass-air interface. These are given as transmission coefficients $T_{in,\omega}(\theta)$ for the incident fundamental beam and $T_{out,2\omega}(\theta)$ for the output interface of the second harmonic. $T_{in,\omega}(\theta)$ is squared in $f(\theta)$ because of the SH's dependence on $(P^{(\omega)})^2$ as seen in eqn. 2.32. $T_{out,2\omega}(\theta)$ represents the glass-air interface that the SH passes through before detection. For p-polarized light , $T(\theta)$ is given by

$$T_p(\theta) = \left(\frac{n_t \cos\theta_t}{n_i \cos\theta_i}\right)\left(\frac{2n_i \cos\theta_i}{n_i \cos\theta_t + n_t \cos\theta_i}\right)^2 \qquad (3.3)$$

where the indices i and t refer to the incident and transmitted index and angles of each interface considered. For s-polarized light $T(\theta)$ is given by

$$T_s(\theta) = \left(\frac{n_t \cos\theta_t}{n_i \cos\theta_i}\right)\left(\frac{2n_i \cos\theta_i}{n_i \cos\theta_i + n_t \cos\theta_t}\right)^2 \qquad (3.4)$$

Because the sample has ∞mm symmetry, with a single axis of symmetry, there is no birefringent walkoff and the second harmonic signal is generated in the same direction as the fundamental beam. When the internal angle is large, the second harmonic should see total internal reflection (TIR) (normal dispersion dictates that TIR will occur for 2ω before ω). This is calculated to occur at $\sim 43.23°$ internal angle (using n(1.06 μm) = 1.45 and n(532 nm) = 1.46)[4], which is associated with $\theta = 83.2°$ external incident angle using Snell's law. A decrease to zero in the Maker fringe scan typically occurs at $\sim 85°$ due to TIR, although this cutoff angle can occur earlier if the edges of the sample clip the laser beam at large incident angles.

The $\sin^2(\theta)$ term in eqn. 3.2 comes from the tensor nature of $\chi^{(2)}$, as was seen in chapter 2 and will be examined more in section 3.1.1.3. As will be seen later, the effective $\chi^{(2)}$ is given by

$$\chi_{eff}^{(2)} \propto \chi_{31}^{(2)} \sin(\theta) \qquad (3.5)$$

and since $I_{2\omega}$ is proportional to $(\chi^{(2)})^2$ (again, see eqn. 2.32), $f(\theta)$ has an additional $\sin^2(\theta)$ dependence. The last factor, $\cos(\theta)$, comes from consideration of the increase in spot size and decrease in power density as the sample is rotated.

The main use of a Maker fringe scan is to detect any destructive interference due to phase mismatch. This dependence is contained in the terms other than $f(\theta)$ in eqn. 3.1. If the nonlinear region is large compared to the coherence length, rotation of the nonlinear sample will reveal multiple modulation fringes that correspond to increases in path length equal to the coherence length. If the region is smaller than the coherence length, multiple fringes will not occur and only two lobes appear on either side of 0 degrees. When only two lobes occur, the peaks can move to smaller angles when path lengths extend beyond the coherence length and destructive interference occurs.

Fused silica samples came as windows or plates and poling electrodes were placed on the broad flat surfaces so that poling occurred across the samples' thin dimension. This poling direction is parallel with the surface normal and was the axis of the frozen-in electric field that broke the centrosymmetry of the glass. This axis is referred to as the z axis. The z axis of the sample was aligned with the propagation direction of the incident laser light when the light was at normal incidence. The incident laser light was from a 10 Hz, ~ 10 ns pulse, 1.06 μm, Q-switched Nd:YAG laser. A half-wave plate along with a

polarizer were used to align the electric field either parallel (*p*-polarization) or perpendicular (*s*-polarization) to the plane of incidence. The aperture allowed reduction of the beam diameter to ~ 2 to 3 mm so that only small areas of the sample were probed. Light was collected from the sample by sending it through a dispersing prism and filtering such that only 532 nm second harmonic light was collected by a photomultiplier tube (PMT). The electronic signal was then sent to an oscilloscope, lock-in amplifier and computer. The lock-in amplifier allowed averaging of signal fluctuations. A full scan consisted of 1000 data points with each data point representing an average of the signal during the last ten seconds. The rotation stage was computer-controllable which allowed slow scans (22.5 - 45 min/180 degrees).

Figure 3.3 shows three example Maker fringe scans. The first two Maker fringe scans show the typical angular dependence observed for thermal poling for two different samples, similar to that observed by most groups. The lopsided nature of individual scans is most likely due to imperfect centering of the rotation axis about the center of the laser beam, or imperfect centering of the aperture in the beam. Peak values tend to be between 50 and 60°. In theory, the peak value angle range of 50-60° is relatively insensitive to the nonlinear region depth, when a uniform nonlinear region is assumed. As can be seen in figure 3.4, the nonlinear region that corresponds to the angle range of 50-60° extends from 10 to 30 μm. Fig. 3.4 shows the evolution of calculated Maker fringe scans with increased nonlinearity depth assuming a uniform nonlinear region and a coherence length of 25 μm. It should be noted, however, that a uniform nonlinear region is not expected as will be discussed in detail in chapter 4. Figure 3.3(a) shows a Heraeus T08 (type II) fused silica cover slip (~ 170 μm thick). Its poling history included being poled for 140 min at

275 °C and 4.3 kV, depoled 1 min at poling temperature and then cooled down. It was

repoled for a second time for a duration that included the warm-up time plus 1 min.

Figure 3.3(b) shows a synthetic fused silica (Esco S1-UV, type III) cover slip that was

(a)

(b)

(c)

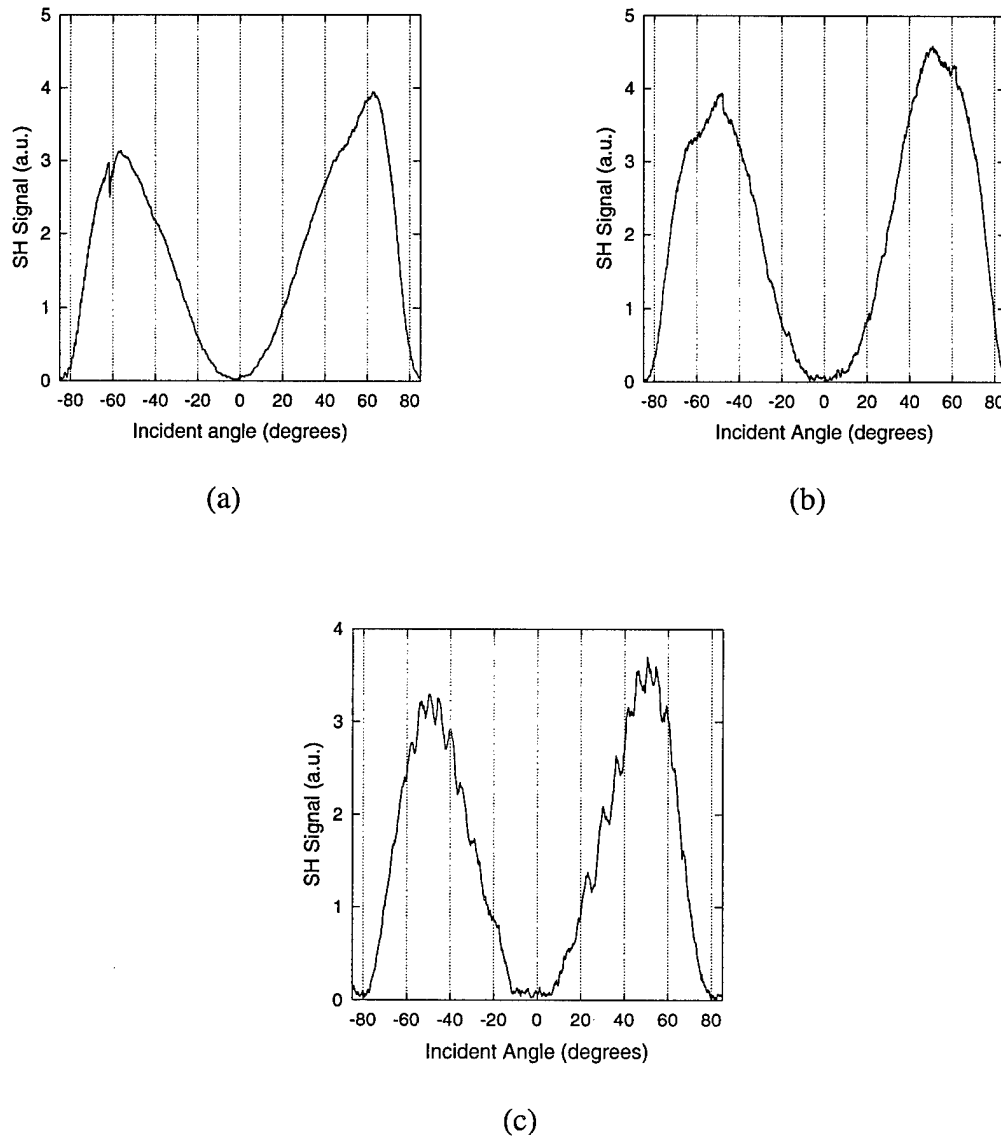Figure 3.3 Maker fringe scans for (a) ~ 170 μm thick type II sample, (b) ~ 170 μm thick type III sample, and (c) 1.6 mm thick type II sample

poled for 10 min at 275 °C and 5 kV. It was interesting to find that a SH signal

comparable to other type II natural fused silica could be generated in these type III cover

slips without special treatment prior to thermal poling. In previous trials with type III

glasses, either high-temperature annealing[1,5] or x-ray treatment[6] has been required to
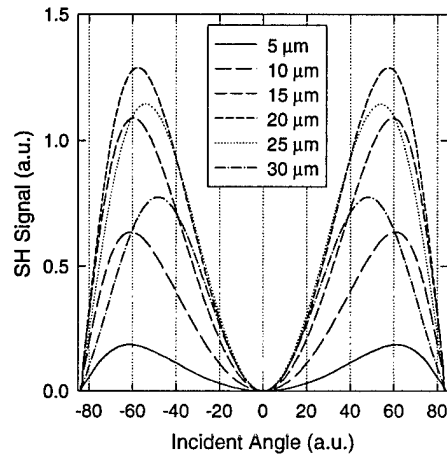generate relatively high SH levels.

Figure 3.4 Calculated evolution of Maker fringe scan with increasing nonlinearity depth, assuming a
coherence length of 25 μm.

The sample in the third Maker fringe scan (figure 3.3(c)) was a 1.6 mm thick

piece of type II natural fused silica (Esco G1). It was poled 30 min at 275 °C and 5 kV.

Note the additional modulation that occurs along with the expected 2-lobed Maker fringe

scan.

The modulation is interesting from the standpoint that the number of fringes

approximately matches what would be expected for a sample 1.6 mm thick that contains a

nonlinearity throughout its bulk, or has two nonlinear regions, one under each surface of

the sample. This can be seen by examining eqn. 3.1. If $d = 1.6$ mm and $l_{coh} \sim 25$ μm,

approximately 11 fringe peaks are calculated between 0 and 80 degrees. This can be seen

in figure 3.5, where the case of a uniform nonlinearity distributed throughout the 1.6 mm,

or equivalently, two uniform regions separated by 1.6 mm, has been calculated. 11 fringe

peaks are also experimentally observed (Fig 3.3 (c)). The small modulation on top of a 2-

lobe fringe scan is similar to what was reported recently by a group in China[7], which is

not as dramatic as the full depth modulation seen by two other groups[8,9]. The small

modulation would indicate that most of the nonlinearity is in one region (assumed to be

under the anode, as shown in other experiments) with the smaller, additional nonlinearity

coming from another region. As will be seen later in this chapter, a smaller nonlinearity

coming from the cathode side has been directly detected under some poling sequences.
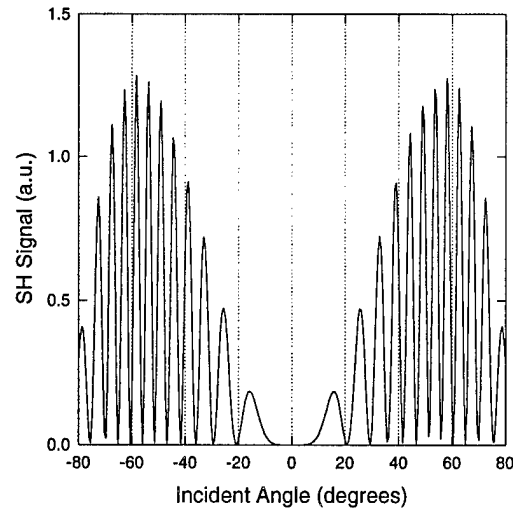

Figure 3.5 Calculated Maker fringe for a nonlinearity distributed uniformly throughout 1.6 mm, or equivalently, two nonlinear regions separated by 1.6 mm. Assumed coherence length was 25 μm.

3.1.1.3 Peak SH and $\chi^{(2)}$ measurement

For quick comparative measurement, a full Maker fringe scan was not needed.

Instead, samples were rotated to the angle at which a peak SH signal was generated. The

SH signal from a reference sample was then measured for comparison. The reference

sample was a piece of poled fused silica labeled EG1A with a relatively high SH signal

level. EG1A was then compared with another nonlinear material whose nonlinearity

level was known. In this case, lithium niobate (LiNbO$_3$) was used for comparison. Table

3.2 shows peak SH intensity levels from Heraeus T08 (type II) cover slips (CS) poled at

4.3 kV with different poling times measured relative to EG1A. There is no clear trend in

the data with poling time and the average intensity ratio (I_{CS}/I_{EG1A}) is 0.85 ± 0.12.

Table 3.2 Peak SHG measurements of T08 cover slips

T08 CS#	1	2	3	4	5	6	7	8	9	10	11
Time (min)	0.5	0.5	1	5	10	15	15	20	22	60	140
I_{CS}/I_{EG1A}	0.67	0.83	1.04	0.75	0.96	0.79	0.79	0.88	1.00	0.92	0.75

Three synthetic fused silica (type III) cover slips were poled and measured as well. These

cover slips were S1-UV from Esco. As mentioned in the previous section, these did not

require additional treatment to show a strong nonlinearity. The results are in table 3.3.

Table 3.3 Peak SHG measurement results for S1-UV cover slips.

S1-UV CS #	1	2	3
Time (min)	10	10	10
Voltage (kV)	4.3	5	5
I_{CS}/I_{EG1A}	0.46	0.83	0.96

In order to find the approximate nonlinearity level measured in pm/V, the EG1A

fused silica reference was compared with z-cut lithium niobate that was 0.5-mm thick. It

is important to use s-polarized light as opposed to p-polarized light for the incident

fundamental beam for both EG1A and LiNbO$_3$ when making this comparison. To see

this, we first need to define axes corresponding to s and p-polarized light. Let the primed

coordinates x', y' and z' correspond to axes in the lab frame, and let z' define the

propagation direction of incident laser light. The sample has unprimed coordinates that

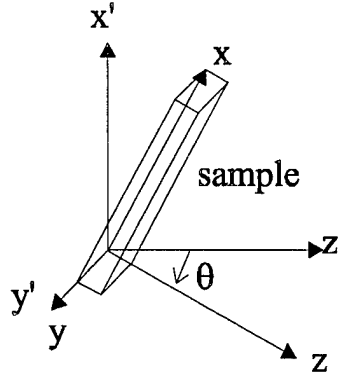define internal axes x, y, and z corresponding to its symmetry, as seen in figure 3.6.

Figure 3.6 Relationship between lab (primed) and sample (unprimed) coordinates.

Rotation of the sample is about the y = y' axis. *P*-polarized light is defined as having its electric field in the direction of x' ($E = E_{x'}$), and y' and z' components are zero. *S*-polarized light is defined as having its electric field in the direction of y' ($E = E_{y'} = E_y$), with x' and z' components equal to zero.

Recall that the nonlinear susceptibility tensor for fused silica was given by eqn. 2.39 as:

$$d_{il} = \begin{bmatrix} 0 & 0 & 0 & 0 & d_{31} & 0 \\ 0 & 0 & 0 & d_{31} & 0 & 0 \\ d_{31} & d_{31} & d_{33} & 0 & 0 & 0 \end{bmatrix} \tag{3.6}$$

and the polarization components were given by 2.40 as:

$$\begin{bmatrix} P_x^{(2\omega)} \\ P_y^{(2\omega)} \\ P_z^{(2\omega)} \end{bmatrix} = \begin{bmatrix} 2d_{31}E_x^{(\omega)}E_z^{(\omega)} \\ 2d_{31}E_y^{(\omega)}E_z^{(\omega)} \\ d_{31}E_x^2 + d_{31}E_y^2 + d_{33}E_z^2 \end{bmatrix} \tag{3.7}$$

If the input beam is *s*-polarized ($E_{x'} = E_{z'} = 0$), then $E_x = E_{x'}\cos\theta + E_{z'}\sin\theta = 0$ and

$E_z = -E_{x'}\sin\theta + E_{z'}\cos\theta = 0$. Therefore, the only surviving term is

$$P_z^{(2\omega)} = d_{31}E_y^2 \tag{3.8}$$

If we rotate this equation into the lab frame, we have

$$P_{x'}^{(2\omega)} = -d_{31}E_y^2 \sin\theta$$
$$P_{z'}^{(2\omega)} = d_{31}E_y^2 \cos\theta$$

(3.9)

Because detection would be made in x' direction, the top equation in eqn. 3.9 applies. The effective d coefficient is thus $d_{eff} = -d_{31}\sin\theta$. We also see with an input s-polarized fundamental beam, the output second harmonic is p-polarized ($E_y^2 = E_{y'}^2$).

The next step is to examine the nonlinear susceptibility tensor for LiNbO$_3$, which has 3m crystal symmetry, and is shown here for Kleinman's symmetry condition[10]:

$$d_{il} = \begin{bmatrix} 0 & 0 & 0 & 0 & d_{31} & -d_{22} \\ -d_{22} & d_{22} & 0 & d_{31} & 0 & 0 \\ d_{31} & d_{31} & d_{33} & 0 & 0 & 0 \end{bmatrix}.$$

(3.10)

Using eqn. 2.38, and assuming input s-polarized light ($E_{y'}$), the result is

$$P_y^{(2\omega)} = P_{y'}^{(2\omega)} = d_{22}E_{y'}^2.$$

(3.11)

Thus a single tensor element is measured with input s-polarization. Because both fused silica and LiNbO$_3$ have second harmonic polarizations that are dependent on a single tensor element, the two can be compared. In order to compare the two, recall that the second harmonic intensity is given by eqn. 2.32. A ratio of the intensity for fused silica to a reference is given by the expression[3]:

$$\frac{I_{fs}^{2\omega}}{I_{ref}^{2\omega}} = \left(\frac{\chi_{fs}^{(2)}}{\chi_{ref}^{(2)}}\right)^2 \frac{(n_\omega^2 n_{2\omega})_{ref}}{(n_\omega^2 n_{2\omega})_{fs}} \left(\frac{\Delta k_{ref}}{\Delta k_{fs}}\right)^2 \left(\frac{A_{ref}}{A_{fs}}\right)^2 \left(\frac{\sin\left(\frac{\Delta k_c L}{2}\right)_{fs}}{\sin\left(\frac{\Delta k_c L}{2}\right)_{ref}}\right)^2 \frac{(T_{in}^2 T_{out})_{fs}}{(T_{in}^2 T_{out})_{ref}}$$

(3.12)

where T_{in} is the Fresnel transmission coefficient of the fundamental beam at the input surface and T_{out} is the Fresnel transmission coefficient of the second harmonic beam at the output surface. Δk is given by $\Delta k = 2\pi\Delta n / \lambda$ for each material. The following physical constants will be needed[4]:

Table 3.4 Physical parameters for $\chi^{(2)}$ measurement of fused silica sample EG1A

Sample	Nonlinear Thickness (μm)	Coherence Length (μm)	$n(\omega)$	$n(2\omega)$	$\Delta k(2\omega)$ $(10^5\ m^{-1})$	$\chi^{(2)}_{eff}$ (pm/V)	SH Signal (a.u.)
SiO$_2$ (EG1A)	5-15	25	1.45	1.46	1.181	?	0.053
LiNbO$_3$	500	3.3	2.232	2.324	10.87	5.26	1

If we assume an incident angle of 50° from the surface normal, the interior angle is 31.9° for fused silica. A beam with a circular area normalized to one at normal incidence has an area of ~1.18 for an ellipse at 32°. The path length through the nonlinearity L is made longer by a factor of $1/\cos(32°) \sim 1.18$ as well. For fused silica, the input Fresnel transmission coefficient for the s-polarized fundamental beam is calculated by eqn 3.3 to be $T_{in} = 0.901$. The output Fresnel coefficient for the p-polarized second harmonic is found to be $T_{out} = 0.998$. LiNbO$_3$ was measured at a peak SH signal approximately at normal incidence so its normalized spot size is approximately unity. The Fresnel coefficients for LiNbO$_3$ are $T_{in} = 0.855$ and $T_{out} = 0.841$. Because the SH signal for LiNbO$_3$ was measured at a peak, it is assumed that for LiNbO$_3$ the phase mismatch is zero. Using eqn. 3.12, we have:

$$\frac{0.053}{1} = \left(\frac{\chi^{(2)}_{31}\sin 32°}{5.26}\right)^2 \frac{\left(2.23^2 2.32\right)}{\left(1.45^2 1.46\right)}\left(\frac{1.09\cdot 10^6}{1.18\cdot 10^5}\right)^2 \left(\frac{1}{1.18}\right)^2 \frac{\sin^2\left(\frac{\pi L_{fs}}{2l_c}\right)}{1}\frac{\left(0.9^2 0.998\right)}{\left(0.86^2 0.84\right)} \quad (3.13)$$

98

Table 3.5 shows the values of $\chi^{(2)}$ calculated using the equation above. The value for $\chi^{(2)}$ for LiNbO$_3$ was taken from a reference source (ref. 4), and is not a fixed standard. It is possible the fused silica calculated values are not quite accurate. Myers[3] compared the SH from a standard quartz reference with a the SH from a LiNbO$_3$ sample, the same LiNbO$_3$ sample source used here as well. He found a factor of ~ 1.25 between observed and calculated results for the quartz and LiNbO$_3$ SH comparison. If the $\chi^{(2)}$ value of LiNbO$_3$ is the source of this difference (i.e. $\chi^{(2)} = 4.7$ pm/V instead of 5.26 pm/V), the fused silica $\chi^{(2)}$ values presented here would be less by the same factor of 1.25.

Table 3.5 Results of $\chi^{(2)}$ measurement of fused silica sample EG1A

L_{fs}	$\chi^{(2)}_{31}$ (pm/V)	$\chi^{(2)}_{33} = 3\chi^{(2)}_{31}$ (pm/V)
15 μm	0.15	0.44
10 μm	0.20	0.59
5 μm	0.36	1.09

These results are larger by a factor of ~ 3 compared to Myers' data[3]. The poled fused silica sample (EG1A) produced a large SH signal, more so than most. However, the comparison with Myers data is indirect, because Myers used standard quartz as his reference, while here nonstandard LiNbO$_3$ was the comparative reference.

3.1.2 *In situ* poling and temporal response of the $\chi^{(2)}$

In this section the formation of the nonlinearity is examined via real-time observation of the SH signal. The dynamics of the growth and decay of the signal are dependent on field polarity, sample history, and ambient environment during heating.

The *in situ* dynamics indicate that under field reversal, there can be a long delay in creating or erasing the nonlinearity.

3.1.2.1 Experiment

Measurements are carried out *in situ* while an electric field is applied to the heated sample as shown in Fig. 3.7 and 3.8. To control the poling atmosphere, the sample is placed in a container with a quartz window. The sample is heated and laser light (a CW mode-locked Nd:YAG laser with $\lambda = 1.06$ μm, ~200 ps pulses, repetition rate 82 MHz, chopped at a 50% duty cycle) is focused onto the top surface of the sample. The focal spot diameter is approximately 50 μm with an average power density of approximately 10 kW/cm^2. The beam makes an angle of ~ 45° with respect to the surface normal, and is *p*-polarized for optimum SH signal. The observations are through a transparent indium-tin-oxide (ITO) electrode (~ 100-nm thick) deposited on the top surface. The sample thickness (5-10 mm) is much greater than the optical depth-of-focus (~ 300 μm) so that only a single surface region of the sample is probed. The optical path includes transmission through the sample, reflection off of a polished Si wafer used as the bottom
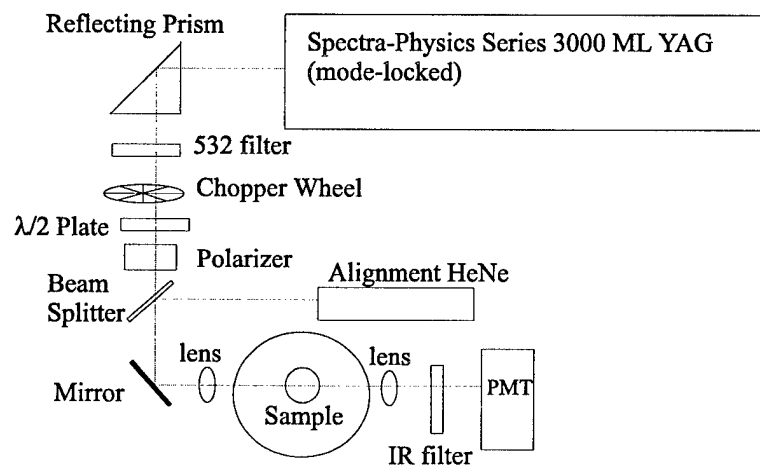

Figure 3.7 Schematic of the experimental layout for *in situ* measurement.
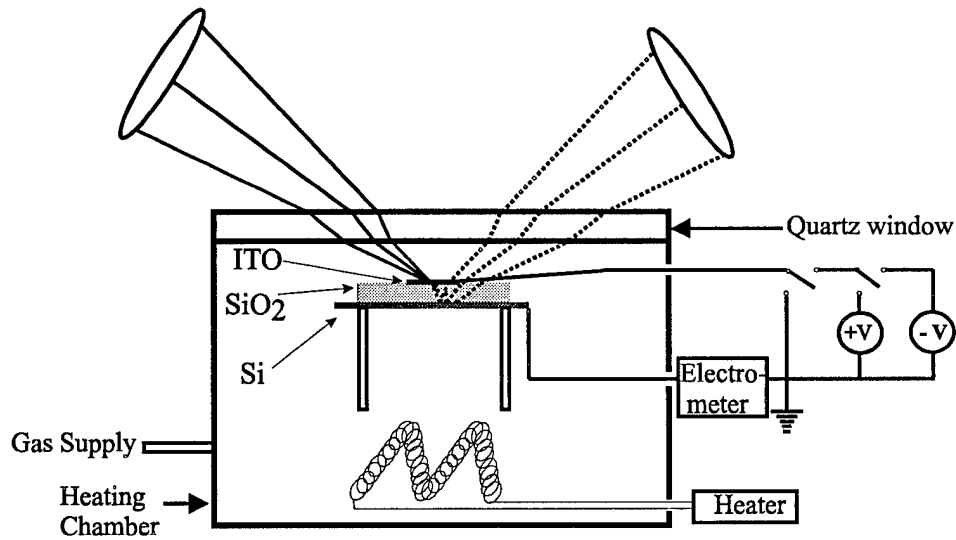
Figure 3.8 Schematic of the heating and poling chamber for *in situ* measurement.

electrode, and retransmission through the sample. After an IR mirror and a 532-nm line

filter are used to filter the SH light, a photomultiplier tube (PMT) is used to detect the SH

light. The PMT is connected to a lock-in amplifier, synchronized with the signal through

a chopper, monitored with an oscilloscope and recorded with a computer. The entire

container is placed on an x-y translation stage, allowing fine control of the sample

position. The voltage applied to the electrodes (ITO and Si wafer) can be switched in

polarity or shorted, on a time scale of ms, using vacuum relay switches. Using a 5-mm

thick fused silica test sample with 13 mm diameter electrodes, the capacitance of the test

sample was measured to be 62 ± 17 pF. Given that the power supplies' internal

impedances are ~1 kΩ, the charging time with the power supply is ~60 ns with the glass

in place. Applied voltages were limited to ±5 kV to avoid electrical breakdown in the

atmospheric pressure ambient. The temperature was monitored using a thermocouple

attached to the sample or a similar piece of glass near the sample. A piece of fused silica cover slip was placed over the thermocouple and Kapton heat resistant tape was used to attach it to the sample and insulate the wires from the ITO electrode.

For concurrent electrical conductivity measurements an electrometer was connected between the bottom electrode and ground to monitor electrical currents through the sample as shown in Fig. 3.8. Current due to surface conduction was minimized by using large samples compared with the ITO electrode dimensions and by careful cleaning of the samples; a guard electrode was not used. The currents observed on switching polarities were much larger than the steady-state currents, suggesting that surface conduction effects were minimal.

3.1.2.2 Initial Poling

Each sample behaves somewhat differently than the next. On the initial poling (5 kV, SHG from the anode side), two general effects are observed: first, there is often a delay before strong SH signal growth, i.e. an incubation period. Second, the growth is a steady slow growth, often taking place over 10's of minutes. A typical observation of an initial poling is shown in Fig. 3.9 for an Esco G1 type II fused silica sample. There is an incubation period of ~ 5 min which occurred before the strong SH signal growth. The incubation period indicates that some process inhibits the nonlinear/space-charge region from forming immediately. Following the incubation period is a slow growth; in this case the SH reaches a peak at about 20 min. after the incubation period.

During the incubation period the conductivity is relatively large and unchanging while there is no observed nonlinearity. As the conductivity decreases over a period of several tens of minutes (as a result of the formation of a blocking space-charge region),

the SH signal grows for this 6-mm thick sample. The fall in conductivity is called the

space-charge conductivity relaxation, or the formation of electrode polarization.

Relatively low conductivity levels occur after space-charge conductivity relaxation. After

the start of space-charge conductivity relaxation, the SH signal grows substantially,

signaling the formation of the nonlinear space-charge region.
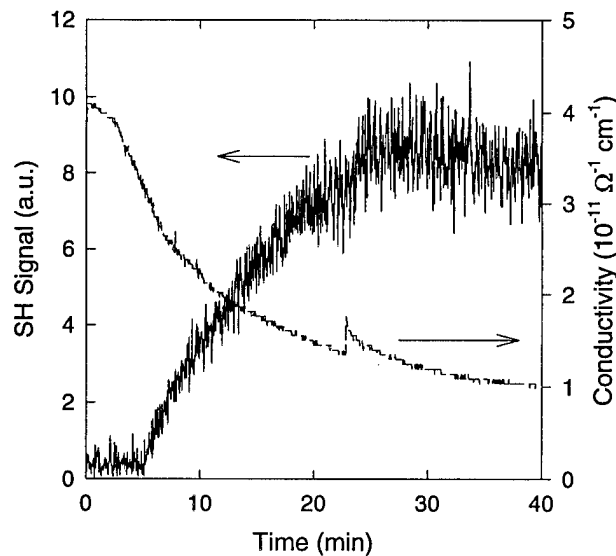

Figure 3.9 Initial poling of Esco G1 sample. Note ~ 5 min delay before growth. (The step in the
conductivity at about 22 min is an artifact and should be ignored.)

3.1.2.3 Shorting and repoling

The effect of shorting the applied voltage to ground and also the effect of

switching from ground to +5 kV was studied. In Fig. 3.10 (a), for 5-mm thick Heraeus

Herasil type II fused silica sample #H11, both the current and the nonlinearity fell rapidly

on a time scale of several seconds rather than 10's of minutes (also see Fig 3.17 for other

measurements on same sample). Fig. 3.10 (b) shows what happened when the sample was

switched from ground to +5 kV. In this case the sample was previously cooled to room

temperature with voltage applied, leaving the space-charge region frozen-in. It was then reheated with no applied voltage to 275°C. Zero time marks this point. Negligible SH signal was detected, yet when the voltage was switched on at t = 15 s, the current fell in ~ 6 seconds (1/e point) and the SH signal rose in 10's of seconds, rather than minutes. The difference in response times seen in Figs. 3.10 (a) and (b), was repeatable for this sample.
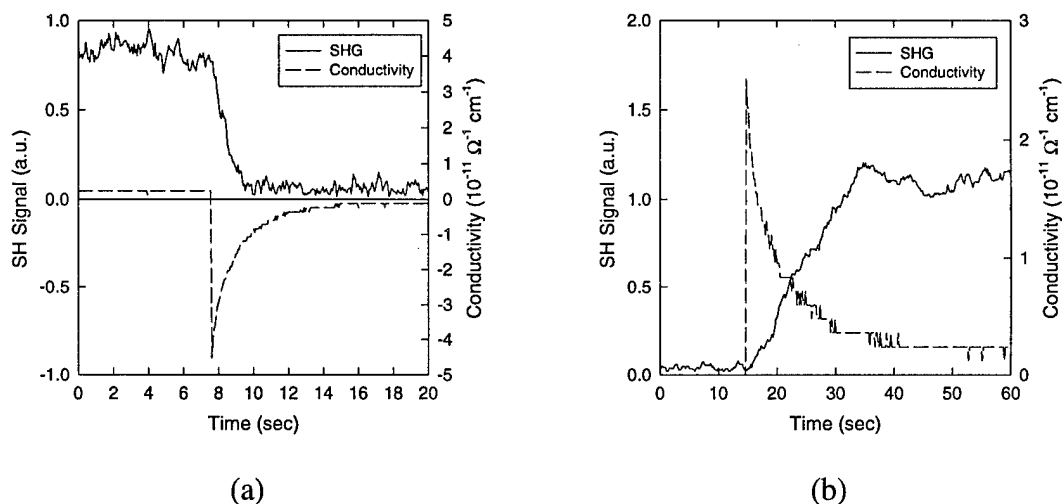

(a)   (b)

Figure 3.10 Effect of switching voltage from +5 to 0 kV (a) and from 0 to +5 kV (b) for Herasil sample #H11. (a) Conductivity falls to 1/e point in ~1.5 s. (b) Conductivity falls to 1/e point in ~5.6 s.

When a sample from a different manufacturer is used, the result of switching voltage from +5 to 0 kV and from 0 to +5 kV gives a longer response time, different from that shown above, showing time scales are sample-dependent. Fig. 3.11 shows Esco G1 sample #EG12 (6-mm thick type II commercial grade fused silica) when switched (also see Figs. 3.9 and 3.12 for measurements on same sample). When switched from positive bias to ground, the conductivity fell to its 1/e value within 25 seconds. The SH signal had a fast decline during the first 1/2 min. coincident with the conductivity relaxation, but then slowly decayed during 4 minutes to a level close to zero. This shows a slow-decaying or transient signal can sometimes exist after grounding. Similarly, when the

104

voltage was switched back on, the conductivity decayed to its 1/e value within 1/2 min while the SH signal quickly rose. After the first half minute, the conductivity slowly decreased and the SH signal slowly increased towards the level attained before shorting to ground.
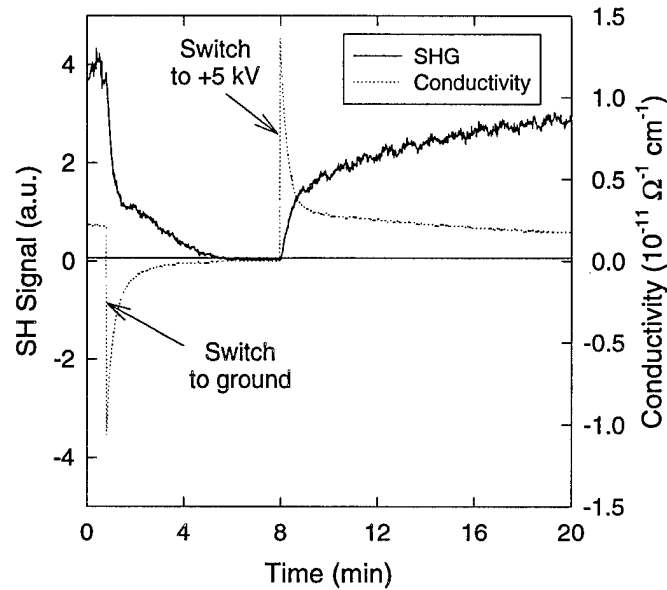

Figure 3.11 Effect of switching voltage from +5 to 0 kV and from 0 to +5 kV for Esco G1 sample #EG12.

In Fig. 3.11, there is a periodic ripple observed on the SH signal. This ripple was frequently, but not always, observed. The cause of the periodic ripple remains undetermined.

3.1.2.4 Comparison of initial poling and repoling

Fig. 3.12 shows a comparison of time scales for the formation of the space charge region for a fixed temperature of 275°C. The electrical current and SHG data show that there are at least two time scales apparent. When the sample is poled for the first time as was also shown in Fig. 3.9, there is first an incubation period of ~ 5 min. and a slow SH

signal growth (~19 min) for this 6-mm thick sample (Esco G1 commercial grade type II silica). (The step in the current at about 22 min is an artifact and should be ignored.) Figure 3.12 also shows the current and SH signals upon reapplying a voltage of the same polarity to the sample, after the sample had been shorted to ground. Both the current and the SHG respond on the same time scale, comparable to the fall times and much faster (~ 29 s) than the original poling. After the rapid response there is a continuing slow rise in the SH signal accompanied by a fall in the current on the original time scale of 10's of minutes.
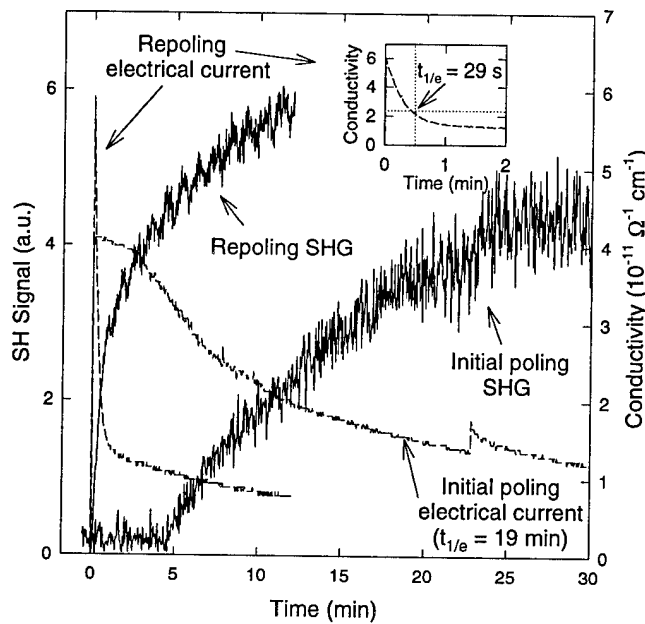

Figure 3.12 Comparison of conductivity and SHG for initial poling and repoling of Esco G1 sample #EG12.

Similarly, the initial poling and repoling after reversing the polarity of the applied field can be compared as seen in Fig. 3.13. In this case Heraeus Herasil samples #H13 and #H14 (5-mm thick, type II fused silica) were poled using "contact" electrodes, so only conductivity data was taken. H13's initial poling was +5 kV; H14 was initially poled at -5

kV. The poling setup was identical for both H13 and H14, except for the type of electrode used corresponding to anode and cathode. For the positive voltage used on H13, the anode was a pressed-on aluminum electrode and the cathode (ground electrode) was a silicon wafer. For the negative voltage used on H14, the cathode was the aluminum electrode and the anode (ground electrode) was the Si wafer. During the initial poling, a slow space charge relaxation was observed with $\tau_{sc} \sim 19$ min. An incubation period of ~ 5 min was observed for H13, while no incubation period was observed for H14. After about 40 min. for H13 and 80 min for H14, the field is reversed. This is done through vacuum relay switches.

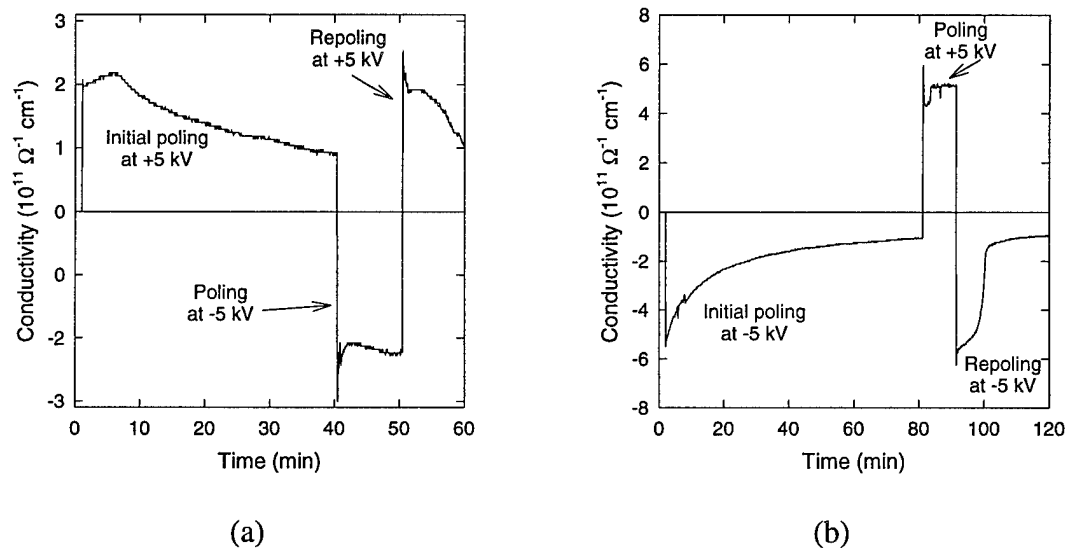(a)   (b)

Figure 3.13 Comparison of conductivity for initial poling and repoling after field reversal of (a) Herasil sample #H13 and (b) Herasil sample #H14.

After ten minutes with the field reversed, the field was again reversed back to the original polarity and a short incubation period was observed for several minutes, followed by space-charge relaxation. The space charge relaxation time was much shorter than for the original poling, with $\tau_{sc} \sim 3$-4 min. After this space-charge relaxation, the current

107

level returned to its previous level before the field reversals, and for H14, appeared to continue to decay at the previous slow rate.

3.1.2.5 Field Reversal

Again, each sample behaved somewhat differently. With multiple polings, the behavior of an individual sample evolved as well. However, some general tendencies were observed by measuring the SH signal and electrical conductivity with time and upon field reversal. Data showing the SH signal will be presented first. Fig. 3.14 shows multiple polings of Heraeus Herasil sample #H1 (5-mm thick, type II fused silica). Each data run consisted of aligning the laser beam and its focus such that a SH signal was observed under the anode while poling at +5 kV and ~ 275 °C. A negative bias voltage is then applied by switching from +5 kV to -5 kV through the vacuum relay switches. The signal (now from the cathode) falls abruptly (< 0.5 min) towards zero. The signal is small for several minutes (Fig 3.14 (a) is flat for ~ 4 min, (b) has a slow fall for ~ 5 min, (c) is flat for ~ 1.5 min, and (d) is flat for ~ 1.5 min), before beginning to slowly rise. In these 4 runs, it took 5 to 13 minutes to rise to a peak which is ~ 1/3 to 1/2 the highest signal level when poled with the positive bias. For sample H1, the SH signal observed with negative bias could persist for very long periods, with a decay that at times appeared somewhat linear in time. For Fig. 3.14 (a), the SH signal decayed to ~ 20% of its peak value after ~ 140 min total negative poling, and ~ 120 min after reaching its peak. Fig. 3.14 (b) shows a sharper, more defined peak that decays a bit more rapidly for ~ 10 min before attaining its slow, approximately linear decay.
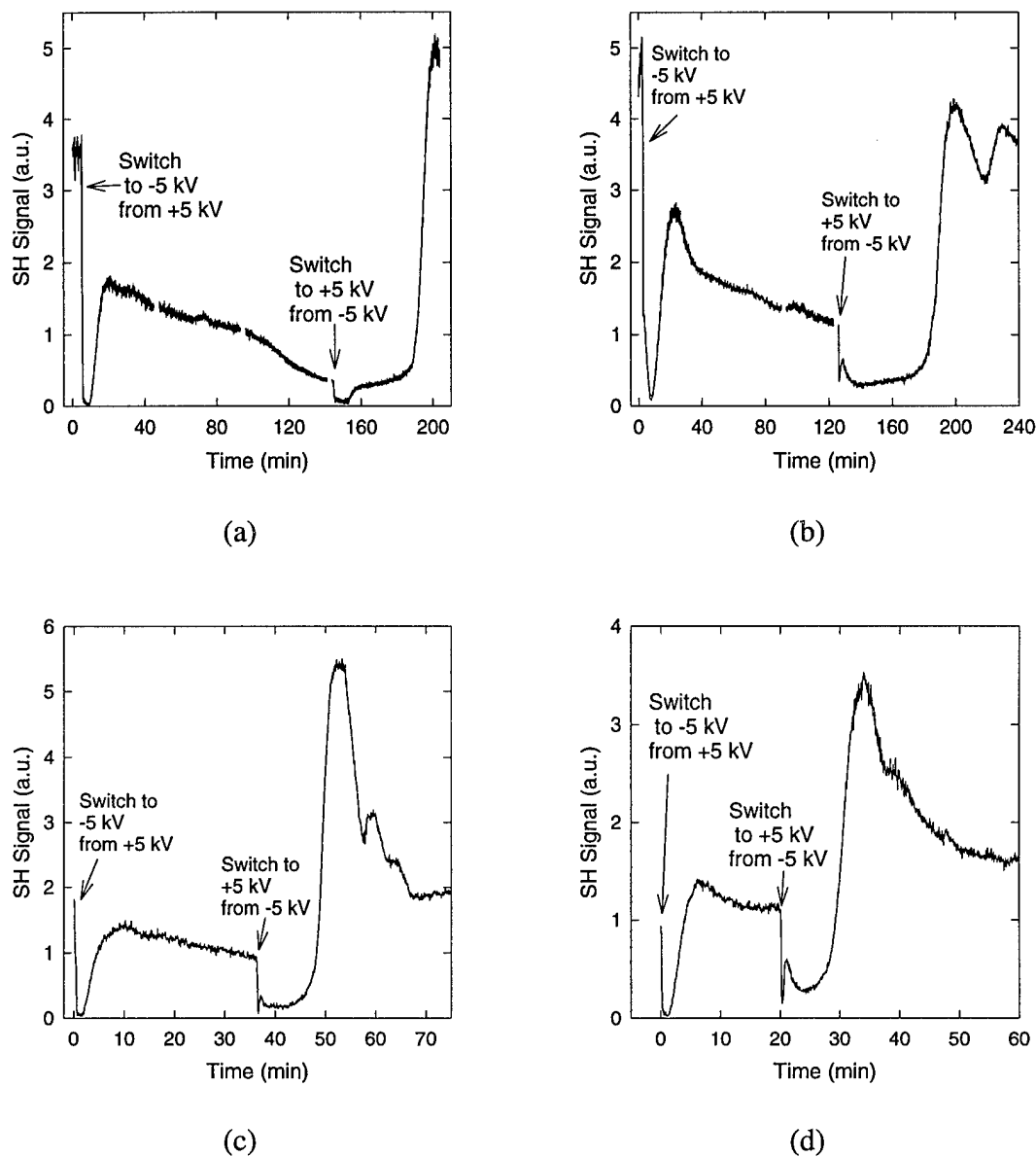
Figure 3.14 Effects of field reversal for Herasil sample #H1. Shows multiple polings in dry nitrogen atmosphere with negative bias for (a) ~ 145 min, (b) ~ 120 min, (c) ~ 38 min, and (d) ~ 20 min. Breaks in curves in (a) & (b) are breaks in data taking. When the sample is switched to -V, SH signal is from the cathode side. When the sample is switched to +V, SH signal is from the anode side.

The *in situ* observation of a SH signal under the cathode is contrary to what has

been most commonly observed through *ex situ* measurement. In the *ex situ* measurement,

the SH signal has commonly been reported to be under the anode. However, the *in situ*

observation of a SH signal on the cathode side, along with the existence of multiple

fringes in several groups' data[7-9], as well as that observed in Fig. 3.3 (c), indicate a smaller cathodic nonlinear region can exist as well.

When the field is again reversed, this time from -5 kV to +5 kV, a fast decay (<0.5 min) and partial recovery (~0.5 to 2.5 min) are first observed in Figs. 3.14 (b)-(d). This is followed by an incubation period. The amount of incubation is roughly dependent on the amount of time the sample was poled at the negative bias, as can be seen in Figs. 3.14 (a) - (d). In graphs (a) and (b) the incubation is ~ 60 min after previous negative bias polings of 140 and 120 min, respectively. In graphs (c) and (d) the incubation is ~ 15 and 12 min after previous negative bias polings of ~ 38 and 20 min, respectively. Also, one can see from graphs (c)-(d) that the SH signal peaks, and then decreases to a substantially lower value. The cause of this decay is not understood, but could be due to the changing overlap of the depth of focus of the laser beam with the nonlinear region. As the nonlinear/space-charge region forms and evolves, the overlap of the focus and the nonlinear region is optimum only during one period of its evolution. Translation of the focus into the sample sometimes improved the SH signal, but not always. Translation of the focus laterally showed that nonuniformity in the SH signal existed across the transparent electrode; some spots had low SH signal levels, while others were high.

Figure 3.15 shows the effect of changing the amount of moisture in the poling atmosphere. The sample used here was Heraeus Herasil sample #H2. When poled in dry nitrogen (Fig. 3.15 (a)), the first thing to notice is the much quicker decay and rise of the SH signal at the switch to -5 kV from +5 kV. The sampling rate (~0.2 Hz in this case) was not fast enough in these graphs to record that the signal decayed close to zero as was visually observed on an oscilloscope. The cathodic SH signal also had a much faster

decay when compared to sample H1 (Fig. 3.14). In less than 10 minutes the SH signal

has decayed to close to zero.
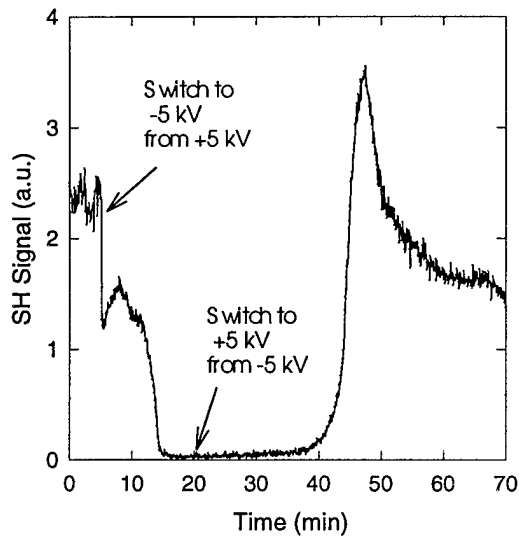
(a)
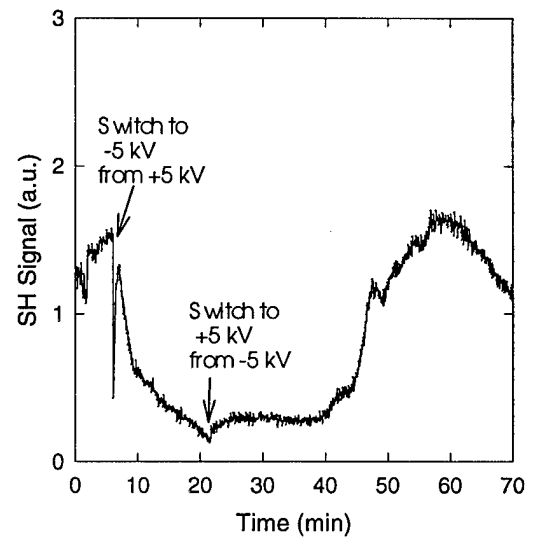
(b)
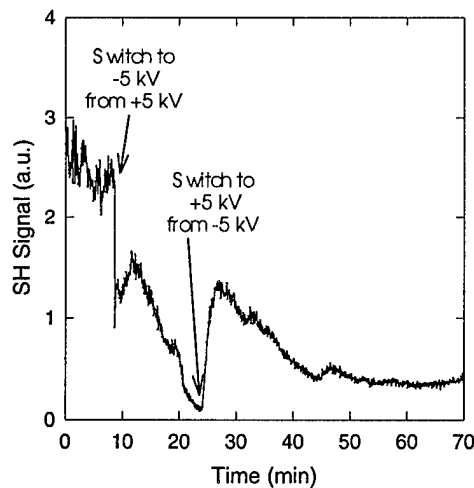
(c)

Figure 3.15 Effects of field reversal on SH signal growth for Herasil sample #H2. (a) Sample is repoled in dry nitrogen atmosphere. (b) Sample is repoled in laboratory ambient. (c) Sample is repoled in an atmosphere of oxygen bubbled through warm water.

The duration of the rise and decay of the cathodic SH signal seems to be sample

dependent. Also, the incubation period is again observed, but this time there is ~25 min

of delay after ~15 min of previous negative bias poling.

111

When the poling in nitrogen is compared to poling in an atmosphere of pumped-in

laboratory air (Fig. 3.15 (b)), the significant differences are a longer decay in the cathodic

signal, a larger SH signal level during the incubation period while under positive bias,

and a later peak in the anodic signal. Yet all these differences may be due to normal

variations during multiple polings.

In order to change the poling atmosphere a bit more dramatically, moisture was

introduced by bubbling oxygen through heated water and sending it into the poling

chamber. The effect on the SH signal dynamics are seen in Fig. 3.15 (c). The most

apparent effect is the elimination of the incubation period. To test if this would occur in a

different sample, Heraeus Herasil sample #H5 was poled under similar conditions as H2.

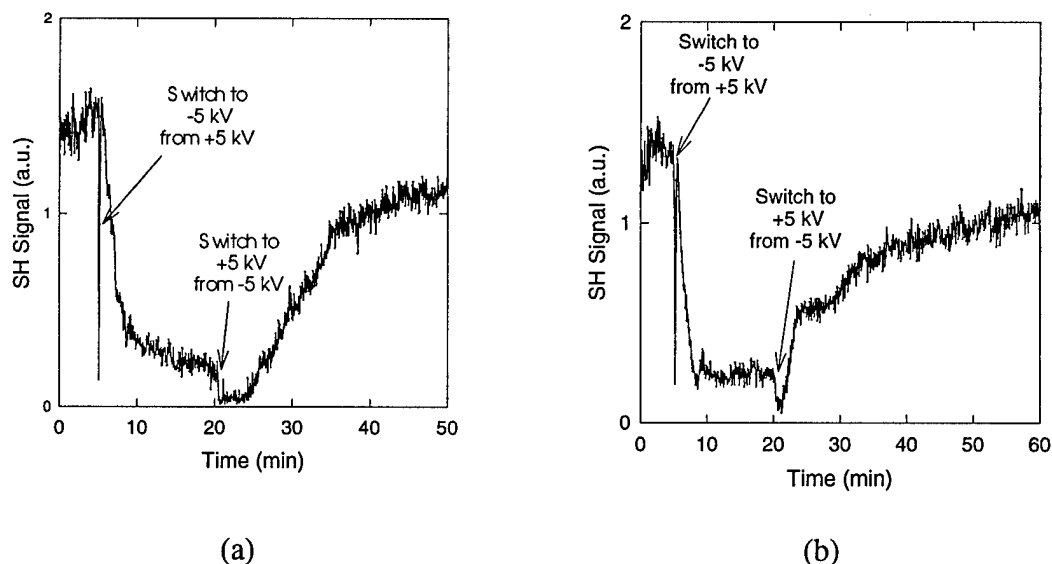The data is seen in Fig. 3.16.

(a)   (b)

Figure 3.16 Effects of field reversal on Herasil sample #H5. (a) Poling in dry nitrogen atmosphere. (b) Poling in an atmosphere of oxygen bubbled through warm water.

Under a dry nitrogen atmosphere (Fig. 3.16 (a)), we again see slightly different,

sample-dependent behavior. When switched from +5 kV to - 5 kV, the SH signal falls

and rises abruptly to a similar level as the initial anodic SH signal level. The cathodic signal then has a fast decay for several minutes, changing into a slow decay after 3 or 4 minutes. When the field is again reversed (from -5 kV to +5 kV), there is a short incubation period of ~ 5 min before a steady rise lasting ~ 10 min to an even slower rise. The observation presented here was stopped before a peak in the anodic SH signal had been attained. When the sample was subsequently poled in the moist atmosphere (Fig. 3.16 (b)), the incubation period was again eliminated and showed a much faster rise.

Myers[3], while making *in situ* measurements, also observed the incubation period. His samples were poled multiple times with a single positive bias. Instead of switching field polarity, he manually turned the samples over to repole. He also observed a small incubation period when a sample was poled for the first time.

Fig. 3.17 shows the effects of field reversal on the conductivity, and helps elucidate the observed behavior of the SHG. Several field reversal cycles are shown for Heraeus Herasil sample #H11 (5-mm thick type II fused silica), poled at + and - 5 kV, at 275-285 °C, with differing durations of negative applied voltage (also see Fig 3.10 for other measurements on same sample). When a strong SH signal has been established, the conductivity or current level is low. When the voltage polarity is switched, the conductivity usually responds with a spike on a short time scale followed by a plateau or slow decay. The spike corresponds to either surface conduction/arcing or to conduction relaxation in the bulk of the glass given by

$$\tau_c = \frac{\varepsilon_0 \varepsilon_\infty}{\sigma_{dc}} \qquad (3.14)$$

where τ_c is the conduction relaxation time, ε_0 is the dielectric constant in vacuum, ε_∞ is

the sample's high frequency relative (in terms of ε_0) dielectric constant, and σ_{dc} is the dc

conductivity.[11] This time is believed to correspond to fast frequency response

mechanisms such as electronic, atomic, or dipole polarization relaxation in the glass.
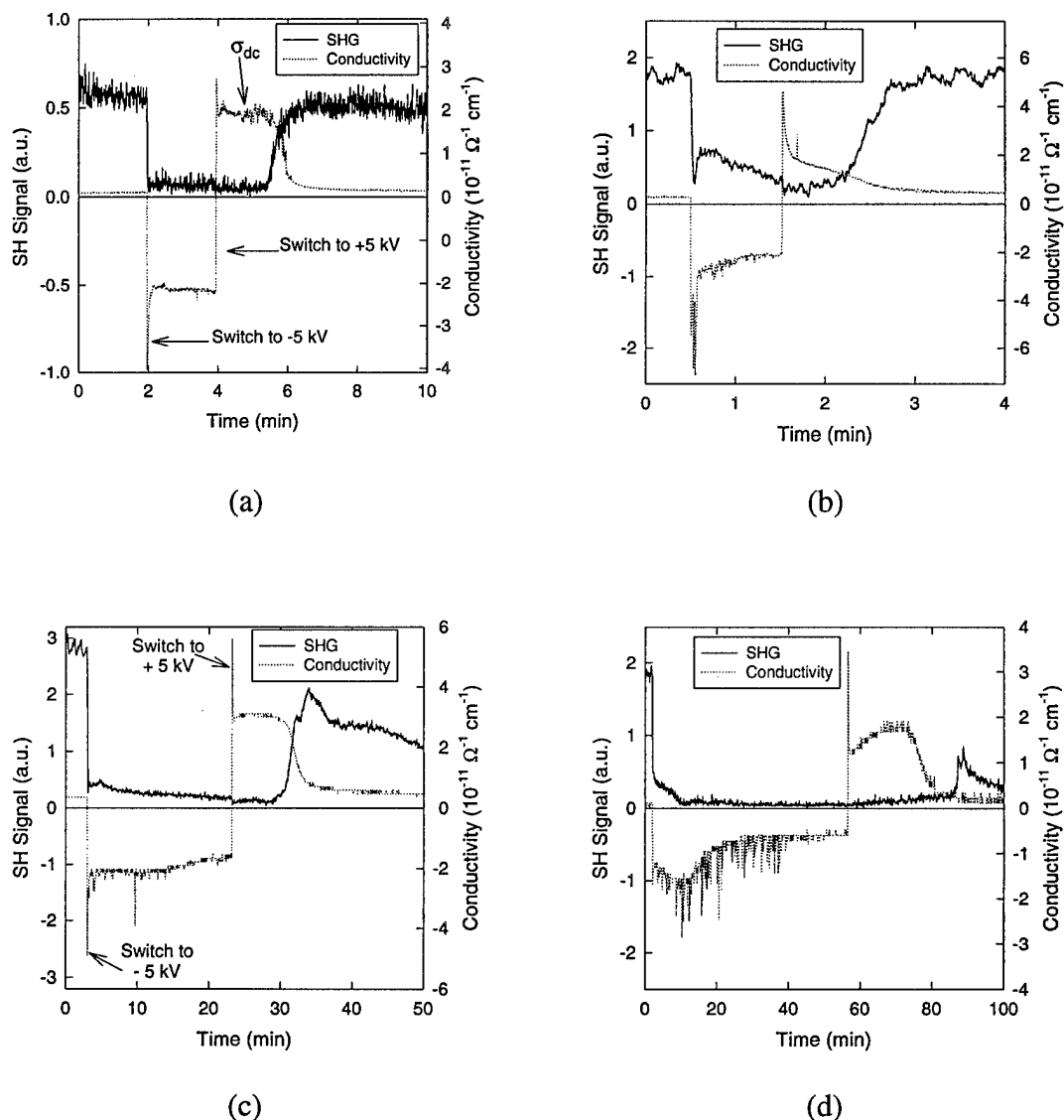

(a)

(b)

(c)

(d)

Figure 3.17 Effect of field reversal on conductivity and SHG for Herasil sample #H11. Various poling times are shown: (a) negative poling for ~ 2 min, (b) negative poling for ~ 1 min, (c) negative poling for ~ 20 min, (d) negative poling for ~ 55 min. Aside from the first spike, spiking such as that shown in (d) is caused by surface arcing and conduction..

The dc conductivity (σ_{dc}) is usually given by the plateau in conductivity before space charge relaxation (e.g. see Fig 3.17a), and for the sample in Fig. 3.17 is $\sim 2\times10^{-11}$ $\Omega^{-1}cm^{-1}$. Using $\varepsilon_0\varepsilon_\infty = 3.8$ ε_0 for fused silica, a conduction relaxation of $\tau_c \sim 0.02$ s is predicted. The conduction relaxation times measured here are longer than predicted by this simple expression (for Fig. 3.17a, $\tau_c \sim 0.06$-0.07 s, for Fig. 3.17c, $\tau_c \sim 0.15$-0.25 s) but they were certainly shorter than the next type of current relaxation that occurred. Take for instance, the conductivity observed in Fig. 3.17 (a) after switching from negative to positive polarity. There is an initial current spike, followed by a dc conductivity plateau, which is followed by the space-charge relaxation. The incubation period in the SH signal is thus linked to the time the sample remains at the high dc conductivity level, before space-charge relaxation. Note that when the sample is poled for long periods with a negative voltage, a space-charge relaxation can also be observed in the conductivity as seen in Fig. 3.17 (c) and (d), although the relaxation is slower, especially in (c). A strong SH signal is not detected because the space-charge region has formed on the opposite side (the new anode side) to that being observed. However, as seen in Fig. 3.17 (b) and (d), a smaller cathodic SH signal can decay and appears to correspond to the dc conductivity level. Note that in Fig. 3.17 (d), the negative and positive conductivities corresponding to incubation periods actually increase slowly before relaxing.

The dc conductivity plateau corresponds to the incubation period observed previously. The incubation period lasts approximately as long as the previous poling at opposite polarity, until it saturates at ~ 10 to 20 min as shown in Fig 3.17 (c) and (d). Once the nonlinear/space charge region formation starts, the space charge conductivity relaxation and the SHG growth both occur on similar time scales. The formation time

scale also appears to be dependent on the length of time for which it was previously poled at the opposite voltage. In Fig 3.17 (a) and (b), the space-charge relaxation time (τ_{sc}) is $\tau_{sc} < 1$ min, whereas in (c) $\tau_{sc} \sim 5$ min, and in (d) $\tau_{sc} \sim 10$ min.

3.1.3 SHG & conductivity measurements summary

The dynamic SHG and conductivity measurements taken from the *in situ* experiment show several important points. 1) There are multiple response times for the same sample. The conductivity and SH signal for an initial poling will respond slower than a repoling after field reversal, which in turn, will respond slower than a repoling after a short to ground. Initial conductivity responses can be as short as ~0.06 s (see Fig. 3.17a) and are believed to be fast electronic, atomic or dipole polarization relaxation. 2) An incubation period for the anodic SH signal (SH signal from under the anode) corresponds to a dc conductivity plateau, while the rise in SH signal corresponds to space-charge conductivity relaxation. 3) A decaying cathodic SH signal can be detected, indicating that the space-charge in this region can persist for several 10's of minutes. The cathodic SH signal appears to correspond to a plateau or slow decrease in the dc conductivity, before and during space-charge formation on the anode side.

These behaviors indicate complex interactions occur in the thermally poled glass. This will be addressed with a model presented in chapter 4.

3.2 Nonlinearity Region Profiling

Two microscopic probe techniques are presented that indicate the extent of the nonlinearity in the glass. Hydroflouric acid etching was used to etch the cross-section of

thin samples. Secondary ion mass spectrometry (SIMS) was used to probe impurity distribution levels under the two electrode surface of poled samples.

3.2.1 Etching & Atomic Force Microscope measurement

Margulis *et al.*[12] imaged photoinduced electric-field gratings in optically-poled SH fibers by exposing fibers to HF acid. After etching into the core, a periodic variation in the remaining thickness corresponding to the quasi-phase-matching inversion of the nonlinearity was observed. More recently, Margulis *et al.*[13] measured the regions of bulk glass affected by the poling process by using an interferometer to continuously monitor HF etch rates. Poled regions etched more slowly than unpoled regions. After etching through the space charge region, the etch rate became comparable to that of the unpoled sample. For a long poling time of 225 min., they found a 5.5-μm deep region which they associated with negative charge, as well as a region out to 34 μm that they associated with a weak excess of positive charge.

Relationships between etch rates and local fields, charges, and structural changes in the glass have been reported. Agarwal and Tomozawa[14] found an increase in etch rate correlated with an increase in the glass fictive temperature (temperature to which the glass is raised before being quenched when manufactured), applied hydrostatic pressure, or compressive stress. They postulated that the increased etch rate corresponds to a decrease in the average Si-O-Si bond angle leading to a higher reactivity. Carlson *et al.*[15] showed that an ionic depletion region in glass was more resistant to HF than the untreated glass. Lesche *et al.*[16] showed that the application of an electric field affects the HF etching rate, and attributed the field dependence to partial orientation of the HF molecules

117

in the electric field. Extrapolating to the strong field in the depletion region in glass, they concluded that the charge that gives rise to the field in Ref. [13] is located at the extremes of the depletion region, with positive charge at the surface and a negative charge layer at ~ 6 μm deep below the anode.

This section describes a study of HF etching transverse to the poling direction to reveal a cross-section of the nonlinear region of thermally poled glass. Cover slips of flame fused Heraeus T08™ fused silica (~ 1 ppm Na, 100 ppm OH) were thermally poled at 275°C and 4.3 kV in an ambient-atmosphere oven. Because the samples were very thin, thermal poling was difficult at high voltages unless the 170- to 180-μm thick cover slips were placed atop soda-lime glass (microscope slide) current limiters with a high-temperature resistivity several orders of magnitude less than that of the fused silica. This helped prevent surface conduction and arcing through the air to the ground electrode. The soda-lime glass was placed atop an aluminum foil electrode contacted to the negative terminal of the voltage supply. Aluminum foil anodes were placed in contact with the top surface of the cover slips. Voltage was applied once heated. Samples were poled for a different amounts of time. At the end of the designated poling period, the oven door was opened and the sample was allowed to cool with the voltage applied. Samples cooled in one minute from 275° to 200°C, by which time the current level typically has decreased at least an order of magnitude. The SH nonlinearity was checked by placing the samples in a Q-switched Nd:YAG 1.06 μm laser beam (the same setup as described in section 3.1.1) and measuring the SH signal at 532 nm. All samples, regardless of poling time, yielded similar levels of SHG within a standard deviation of $\sim$14% due to preparation and

measurement variability. The tabulated results were presented earlier and are in Table 3.1. Poling times do not include any cool down time.

After poling, the samples were broken to expose a cross-section of the nonlinear region. The samples usually broke with a relatively smooth cross-sectional surface, although the side under compression during the break was often marred due to compression fractures and other features. The cathode side was under compression leaving the nonlinear region near the anode side unaffected by the breaking. The samples were then immersed in 49% HF acid for 30 s. After rinsing, samples were viewed using an optical microscope, profiled with the contact mode of a Digital Instruments Nanoscope III atomic force microscope (AFM), or for two samples, observed with a scanning electron microscope (SEM).

When viewed under a 40x optical microscope, a thin stripe was evident, as shown on the left side of Fig. 3.18 (a). The sample in Fig. 3.18 (a) was poled at 4.3 kV, ~ 275°C,

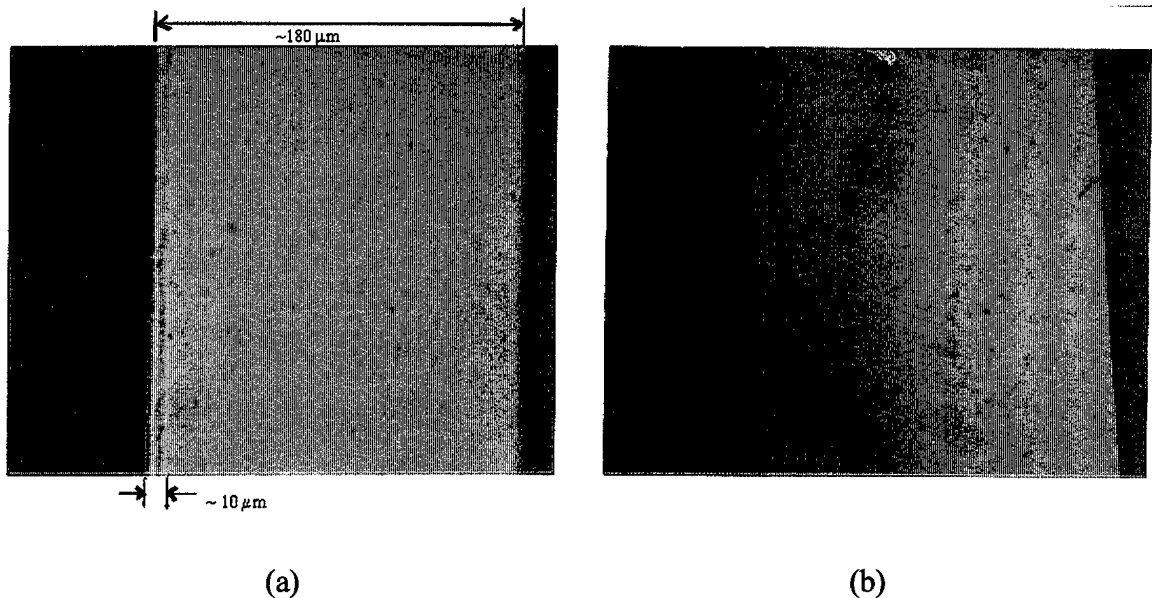(a)   (b)

Figure 3.18 Photographs from optical microscope for (a) cover slip cross section of a sample poled for 1/2 minute and etched in HF acid, (b) cover slip cross section of unpoled sample also etched in HF acid. Spottiness in photographs is due to a dirty lens system in camera. Large marked width is approximately 180 µm, thin marked width is approximately 10 µm.

119

and for 30 s. The striped region is ~ 10 μm wide and the sample is ~ 180 μm thick. The sample in Fig. 3.18 (b) is an unpoled, unheated sample, that was etched under the same conditions as the poled samples. No stripe was identifiable.

The etching profile observed varies somewhat along the sample, but contains some common features which can be seen in AFM images such as Fig. 3.19 (a) (for a sample poled for 30 s): a first ridge very near the surface and a second main ridge ~ 6 μm into the sample. The ridges are indicative of a slower HF etch rate than the rest of the sample and are typically 200- to 300-nm high. The etch rate in 49% HF is ~300- to 400 nm/30 s, indicating that there is a 50-75% decrease in the etch rate at the ridge peaks. The depth into the sample of the first ridge varies significantly from position to position along the cross-section. Figs. 3.19 (b) and (c) show that besides the two main ridges, additional sub-ridges occurred as well.

The position of the second main ridge shows a quite consistent trend with poling time as seen in Figure 3.20. The data points shown in the inset are taken from a single sample on which three ITO electrodes were deposited with a 3-mm interelectrode spacing. The 4.3 kV poling voltage was applied to each electrode for differing time periods. There was a slight current leakage to the other electrodes, but the resultant voltages were small (~100 V) compared to 4.3 kV. The second peak moves deeper into the sample roughly as the logarithm of the poling time. Other samples from a different glass supplier (ESCO G1) showed significantly increased inhomogeneity and a much less well defined behavior, even though the SH signals were comparable for both types of glass.

120
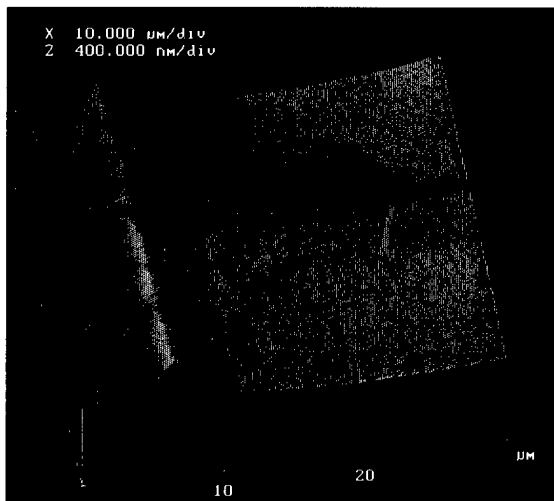
(a)
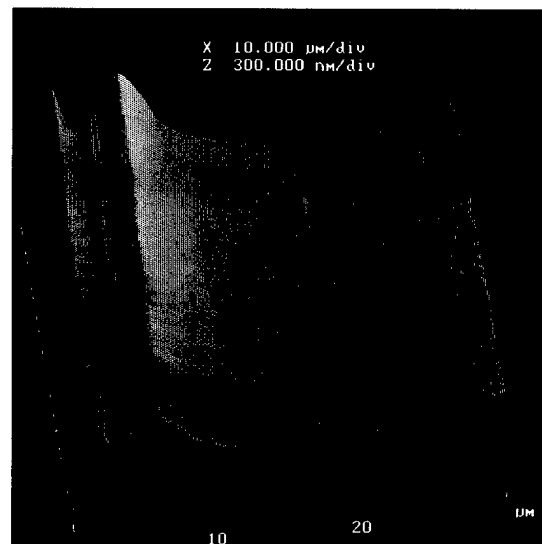
(b)
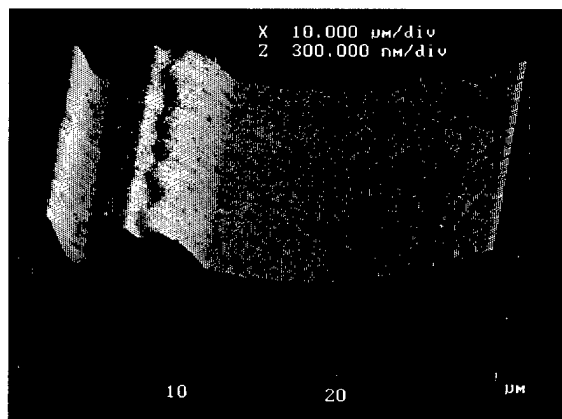
(c)

Figure 3.19 AFM images of etched cross section of sample poled for 30 s. (a)-(c) show three different positions along the cross section. Left edge of each figure is anodic surface. For these three figures the second ridge is located an average 6.2 μm under the surface.

Figure 3.20 shows the same trend for several samples with different poling periods.

Each data point represents an individual sample. The logarithmic trend of ridge depth

with poling time is clear. A straight line fit to the logarithm of the poling time is shown.
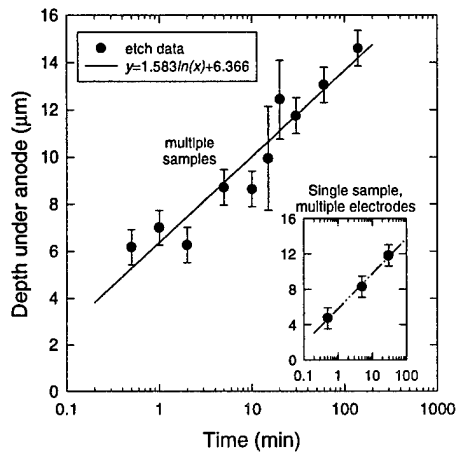

Figure 3.20 Depth of the second ridge below the anode as a function of poling time. Two sets of data are shown. The three points in the inset data correspond to a single sample with varying poling times on isolated electrodes. The main set of points correspond to separate samples poled for varying times. The fit to a simple logarithmic time dependence is shown for both data sets.

Fig. 3.21 shows the AFM images of selected samples that were plotted in Fig. 3.20.

Fig. 3.21 (a) shows an unpoled cover slip which was also etched and ridges were not

observed. As mentioned before, etch rate variations have been associated with the

structural variations of the Si-O-Si bond angle[14] as well as with the local electric field

within the glass[16]. One possibility is that the typical etch profile reflects the high electric

field profile present in the space charge region. It should be cautioned that in the case of

the Ref. [16], the E-field was normal to the etched surface, whereas, in the present case

the E-field was parallel to the etched surface, possibly impacting correlation between the

etch rate and electric field through orientation of the HF molecules. If the etch profile is

122
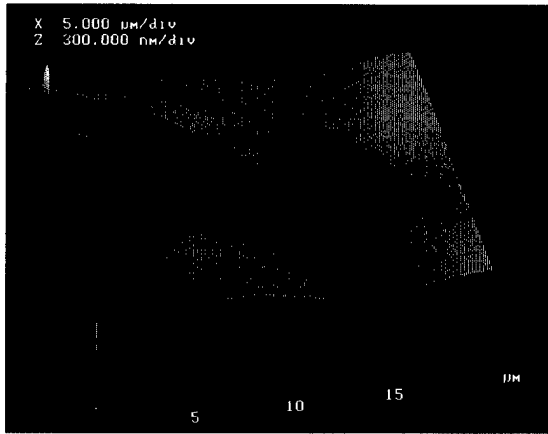
(a) Unpoled
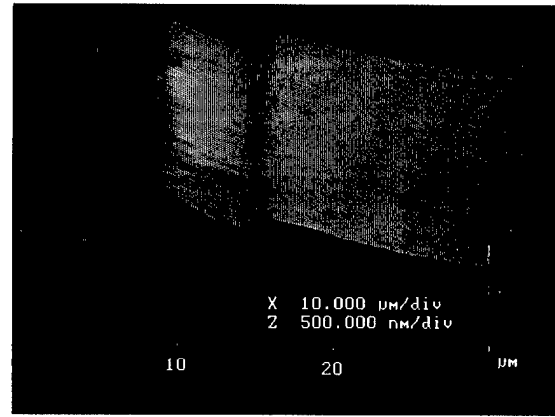
(b) Poled 1 min
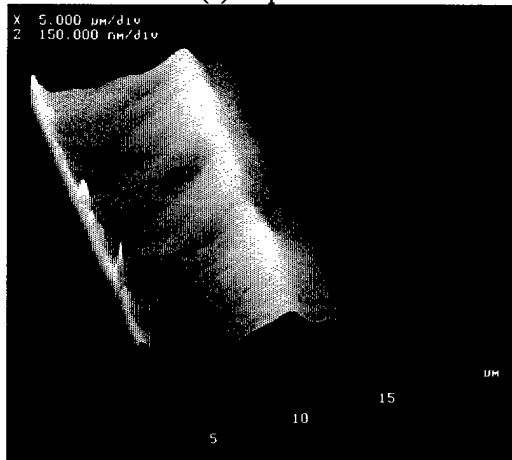
(c) Poled 5 min
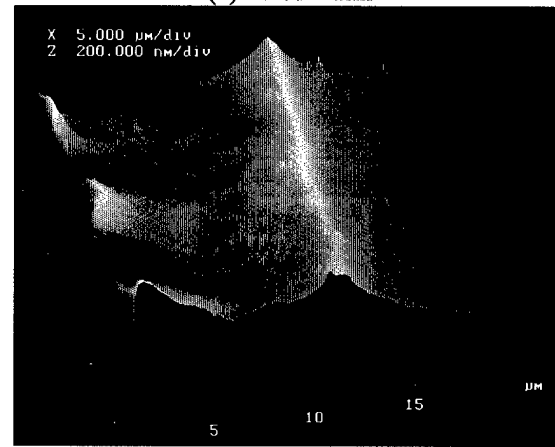
(d) Poled 15 min
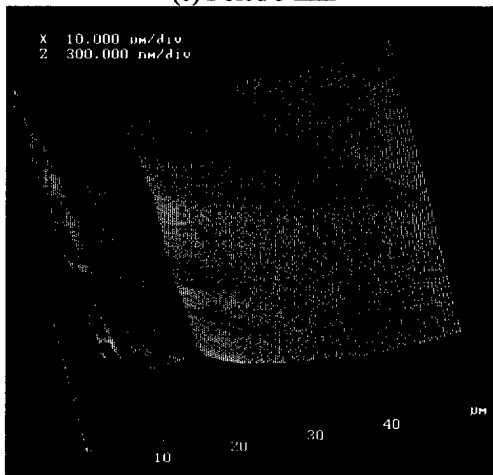
(e) Poled 60 min
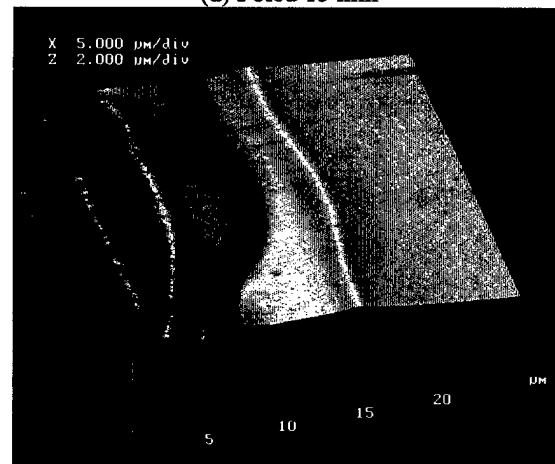
(f) Poled 140 min

Figure 3.21 Separate etched samples poled for varying times. The left edge of each figure is the anodic surface. Each sample cross section was etched in 49% HF for 30 s. Note that the second ridge moves deeper into the sample with poling time. The second ridge depth for these figures is: (b) ~ 6.4 μm, (c) ~ 8.5 μm, (d) ~ 11.4 μm, (e) ~ 12.5 μm and (f) ~ 14.7 μm

123

indicative of the internal field, the presence of two ridges is evidence for two negatively

charged depletion regions, separated by a positively charged or neutral region.

Current measurements were taken on two samples to monitor the space charge

relaxation; Fig. 3.22 shows one result. The increase in current in the first half minute is

similar to the increases or plateaus of the current before space-charge relaxation that are

sometimes observed (see for example Fig. 3.15 (a)). The fact that current measurements

show that the space charge region forms within two minutes, yet the ridge continues to

move deeper into the sample for longer times, is strong evidence that positive charge

injection continues at the anode. Since the SH signals are not changing substantially

during this evolution, the nonlinear susceptibility is clearly varying dramatically.
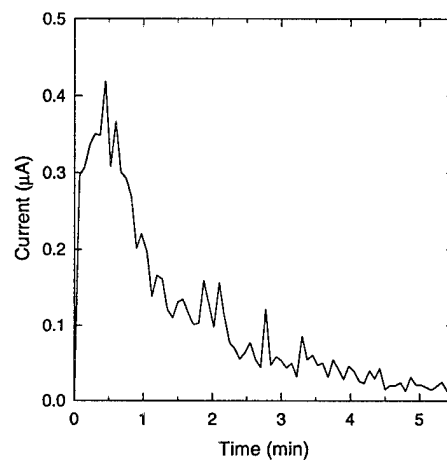
Figure 3.22 Current vs. time, showing depletion region formation time. The spikes result from surface arcing.

There are other significant subfeatures that were observed on various samples poled

for ~ 60 min or longer. As seen in Fig. 3.21 (e) and (f), a deep channel forms, reflecting a

substantially increased etch rate. The channel is always located between the two ridges,

yet its position changes depending where along the sample it is measured. Fig 3.23 (a)

shows in an AFM image how the position of the channel can be located adjacent to the second ridge. Fig. 3.23 (b) shows the extent of the "meandering" of the groove in a SEM image. Thus, a trend with time was not quantifiable. The groove in Fig. 3.21 (f) was found to be ~ 0.75-μm deep when observed using a SEM. Fig. 3.23 (c) and (d) show cross-section SEM images of the channel showing the relatively deep V-shaped groove. The channel seems too narrow to reflect an electric field variation and is more likely indicative of compressive stress[14] or a localized defect accumulation.

In order to investigate whether or not the etching rate is affected by depoling, a Heraeus T08 cover slip sample was poled for a total of ~155 min (the sample poled three times for 140 min, 1 min, and 14 min), 4.3 kV, ~275°C, and subsequently depoled by heating the sample to ~275°C with electrodes shorted to ground. After depoling, the SHG level was measured in the maker fringe setup and an SHG level of 5% or less of its previous poled level was found. The sample was then etched in 49% HF for 30 s to see if appreciable differences in etching occurred. Fig. 3.24 shows how the depoled sample etched in a manner similar to the sample poled for 140 min. The depoling appears not to have significantly affected the etch features, implying that either there is still a significant electric field in the glass (but which integrates to zero voltage giving no SH signal), or the electric field is not responsible for the etch rates. The second ridge was measured from AFM images to be 15.7±0.9 μm under the anodic surface. Given that this sample was poled multiple times and then depoled, and that the other cover slip samples were poled only once, it's not appropriate to include it in Fig. 3.20. If it were to be included, however, it's interesting to note that the data point would lie significantly higher than the logarithmic fit.
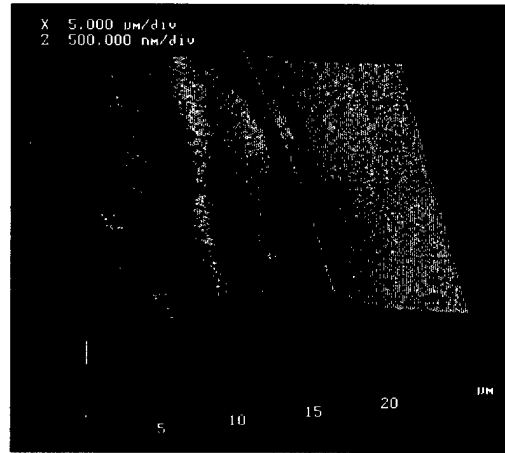
(a)
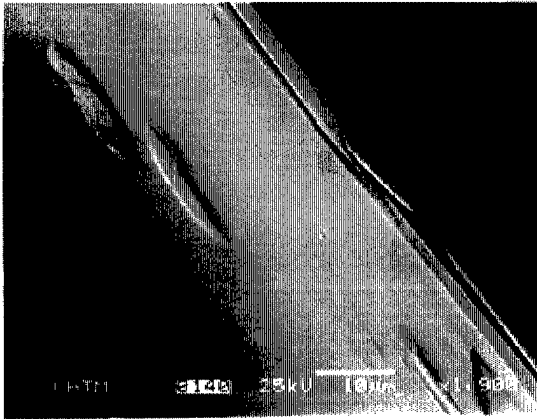
(b)
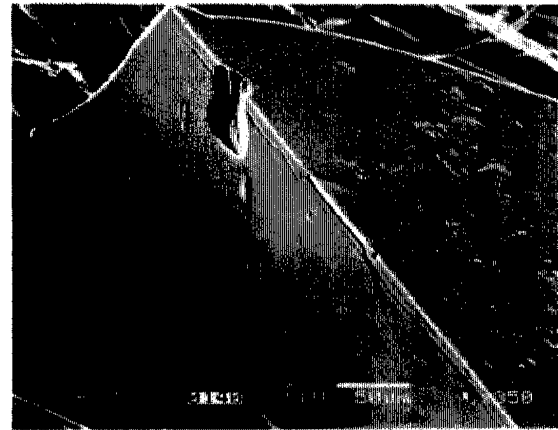
(c)

(d)

(e)

Figure 3.23 Images of the channel formed by an increased etch rate for a sample poled for 140 min. (a) AFM image showing how the channel can move to a postion adjacent to the second ridge. The left side is the anodic surface. (b) and (c) are SEM images showing the extent of variation in position. (b) Shows the etched cross section. Right edge is the anodic surface. Dark "meandering" stripe under the right edge is the channel. Light stripe under the channel is the second ridge. (c) Top and to the right surface is the anodic surface; the surface between parallel edges is the exposed and etched cross section. The dark line just below the edge of the anodic surface is the etched channel. (d) and (e) Close-up SEM images of the V-shaped groove.

126

(a)   (b)
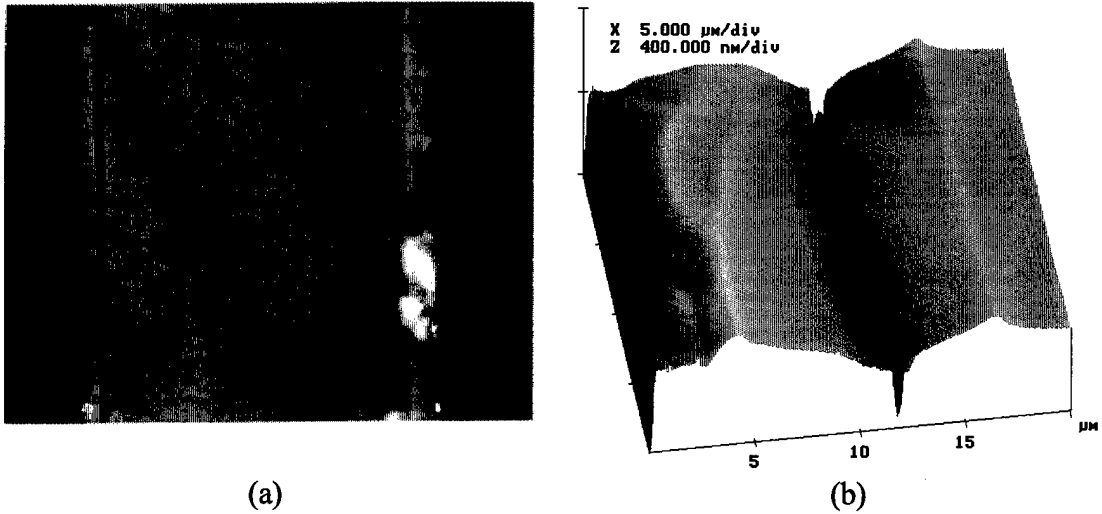
Figure 3.24 Sample poled for a total of 155 min, subsequently depoled, and then etched. (a) Optical microscope photograph showing groove and second ridge. (b) AFM image. Left side of both images is the anodic surface. The stripe on the right side of (a) is not a result of etching, but due to fractures and a compression stress that occurred when sample was broken in two.

(a)   (b)
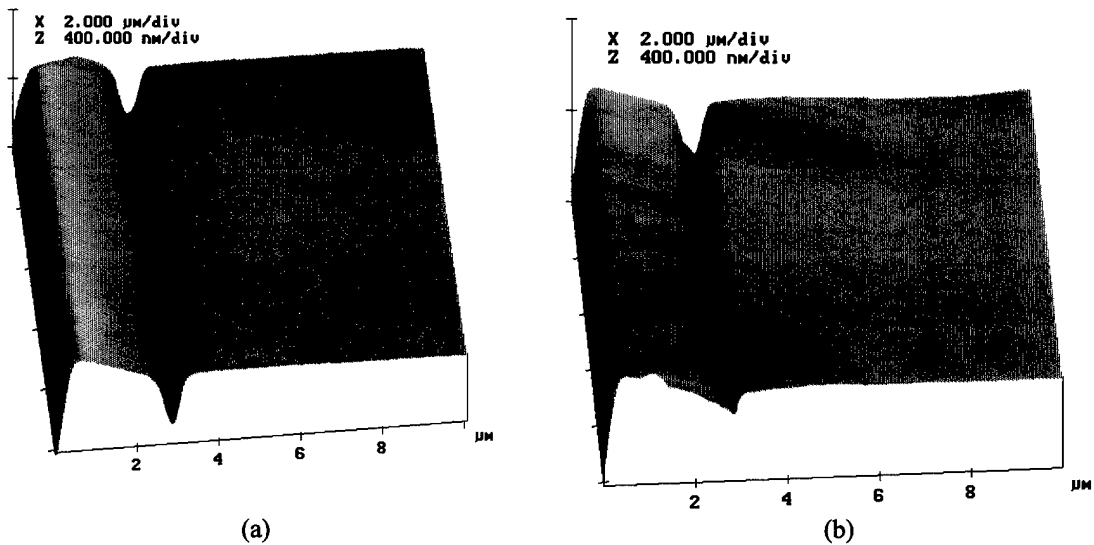
Figure 3.25 Two AFM images of etched type III synthetic fused cover slip, poled for 10 min.

As a final etching experiment, an attempt at etching a poled type III synthetic fused silica (Esco S1-UV) cover slip was made. As mentioned in section 3.1.1.2 and shown in Fig 3.3 (b), these samples did not require prior heat treatment to produce a nonlinearity. Table 3.2 shows the peak SHG measurements of three samples, sample #3 was used for etching. The result of etching a S1-UV cover slip poled for 10 min, 5 kV, ~275°C, is shown in Fig 3.25. A second ridge was not observed, suggesting that the second ridge might be associated with the larger amounts of impurities or impurity structures present in type II fused silica. A channel formed at ~2.6 μm under the anodic surface, showing that the channel can form with less poling time in the type III glass (~10 min) than the type II (~60 min).

This experiment provides, for the first time, a spatially resolved visualization of the nonlinear region in thermally poled fused silica through cross-sectional HF etching. A ridge corresponding to a decreased etch rate moves deeper into the sample logarithmically with poling time. Consideration was given as to whether or not the ridges reflect the electric field profile in the glass, but the fact that the depoling doesn't change etching features, plus the observation of a channel with an increased etching rate for extended poling times suggests that more complicated effects, possibly related to localized structural changes, are occurring. Notably, this is the first measurement that demonstrates that the extent and hence the strength of the second-order nonlinear susceptibility ($\chi^{(2)}$) is varying significantly with poling time even though the SH signals are not. This is consistent with the electric-field induced nonlinearity models that predict that $\chi^{(2)}$ is proportional to E, and thus the SH signal is proportional to $\left[\int E dx \right]^2 \sim V^2$, as long as the nonlinear region is less than a coherence length.

128

3.2.2 Secondary ion mass spectroscopy

3.2.2.1 Background on ion probes and space charge profiling in glasses

Several methods have been identified and used to study glass space-charge regions. For example, Carlson[17] used ion scattering spectrometry (ISS) in combination with ion milling. He found a cation-depleted region in a sodium silicate glass, but could not distinguish ion types. Lepienski *et al*[18] used nuclear techniques to study the space charge region in soda-lime glass. They used nuclear reaction analysis from a proton beam for detection of Na, Rutherford backscattering spectrometry (RBS) from an ionized He beam for detection of Ca, and elastic recoil detection (ERD) from an ionized He beam for detection of hydrogen. Samples were poled with 17 kV/cm at 150°C for varying amounts of time. Depletion layers of Na and Ca were found 0.1 to 0.3 μm deep. Hydrogen accumulation regions were found at the inside edge of the Na depletion for samples with deposited electrodes, while a hydrated layer was found in the Na depletion region for a "press-on" electrode.

Gossink[19] used secondary ion mass spectroscopy (SIMS) to analyze a field-assisted glass to metal seal, which was caused by the formation of a depletion region in a sodium silicate glass after applying 400 V at 500°C in a vacuum. He identified a layer 0.3 to 0.5 μm wide depleted of Na^+, Ca^+, and K^+. He also observed a region 0.1 to 0.2 μm wide depleted of Mn^+ and Mg^+. Gossink[20] also pointed out that conversion of ion count rates into concentrations of the elements is a difficult matter due to differing ionization rates for different elements as well as for the same element in different

matrices (called the matrix effect). Often an external standard close to that being examined is used to identify bulk impurity levels for calibration.

3.2.2.2 SIMS profiling in fused silica

SIMS was used to examine the formation of the space-charge region in thermally poled fused silica. SIMS uses an ion beam to sputter away surface layers in a sample. Most of the atoms sputtered away by the ion beam are uncharged, but a few are ionized in the process. A mass spectrometer separates the ionized atoms according to their charge to mass ratio using electric and magnetic fields. Counts of ionized atoms are made as the ion beam continues to mill into the surface, and ion count rates correspond to variations in individual chemical concentration with depth.

A Camica ion microscope 4F was used to study poled fused silica. A focused $^{16}O^-$ primary ion beam sputtered material from sample surfaces. The primary beam was nominally 12.5 kV and 200 nA, with a typical 100 µm diameter on the sample surface. The beam was rastered over a 50x50 µm area. Secondary ions were accelerated through a nominal 4.5 kV potential to which a 50 V energy offset had been applied. Samples were coated with a ~50 nm gold film to prevent electrical charging during analysis. A 33-µm diameter field aperture was used to collect ions from the center of the sputter crater.

The following species: ^1H, ^7Li, ^{23}Na, ^{24}Mg, ^{27}Al, ^{30}Si, ^{39}K, ^{40}Ca, ^{48}Ti, and ^{56}Fe, were analyzed based on the glass manufacturer's catalog data on trace impurities. Mass separation was achieved using a sector magnet which was stepped through the above mass sequence; each mass station was integrated for 2 s during each of the magnet cycles. Ion detection used a 16 dynode electron multiplier operated in pulse counting mode. The limit of detection of this technique is estimated at <5 ppm. The milling depth is

determined by scanning the sputter crater with a surface profilometer and calibrating the counts measured over time by assuming a constant sputter rate. Depth resolution of the final sputtered crater is limited by a conical shape. At shallow depths the resolution is better than 0.5 μm; at final depths the resolution degrades to ~2 μm.

The ion count rate was analyzed by using a ratio of counts of an individual element to the counts of ^{30}Si detected. This helped normalize some of the sharp changes in counts observed at the surface. Fig. 3.26 shows SIMS analyses for two different unpoled Heraeus T08 fused silica cover slips. The analyses show count ratios sputtered to two different depths. The distribution of each element should only be compared with itself, due to the differences in ionization rates. It is noticed however, that H, Al, and Fe counts are much greater than others. Note that in the unpoled glass there was already a slight depletion in Li and Na in the first few μm's under the surface. This is possibly due to ion exchange, perhaps with H ions. Note also the large H concentration in the first 0.5 μm.

The next figure shows the result of poling a cover slip and its effect on the impurity distributions. Fig. 3.27 shows the both the anodic and cathodic near-surface regions for a Heraeus T08 cover slip poled for 20 min at 4.3 kV and 275°C. Note that on the anode side, a dip in the distribution of Na is evident, indicating depletion from ~ 5 to ~26 μm. Also, a more abrupt depletion in Li occurred out to ~11 μm as well. The only other ion with apparent mobility was K, where a buildup was seen to occur within the first 3 μm's as K is pulled in from the surface (presumably from surface contamination). The accumulation of Na within the first 10 μm's could also be due to surface injection of Na from surface contamination.
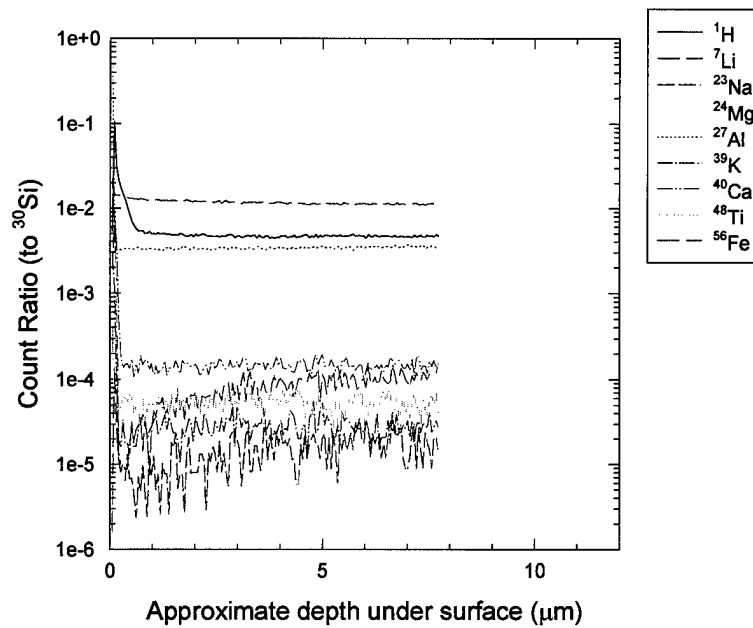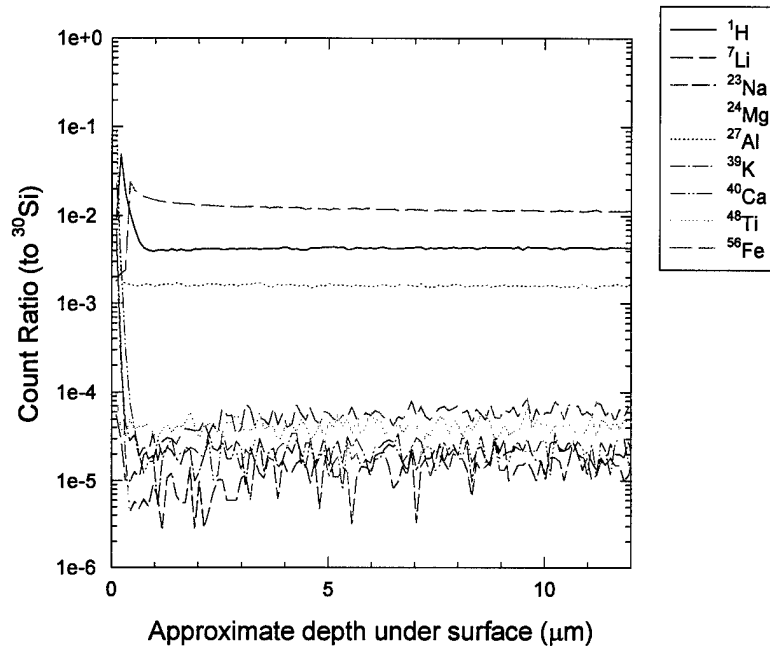
131

Figure 3.26 SIMS analyses of near-surface region of two unpoled type II (Heraeus T08) fused silica cover slips .
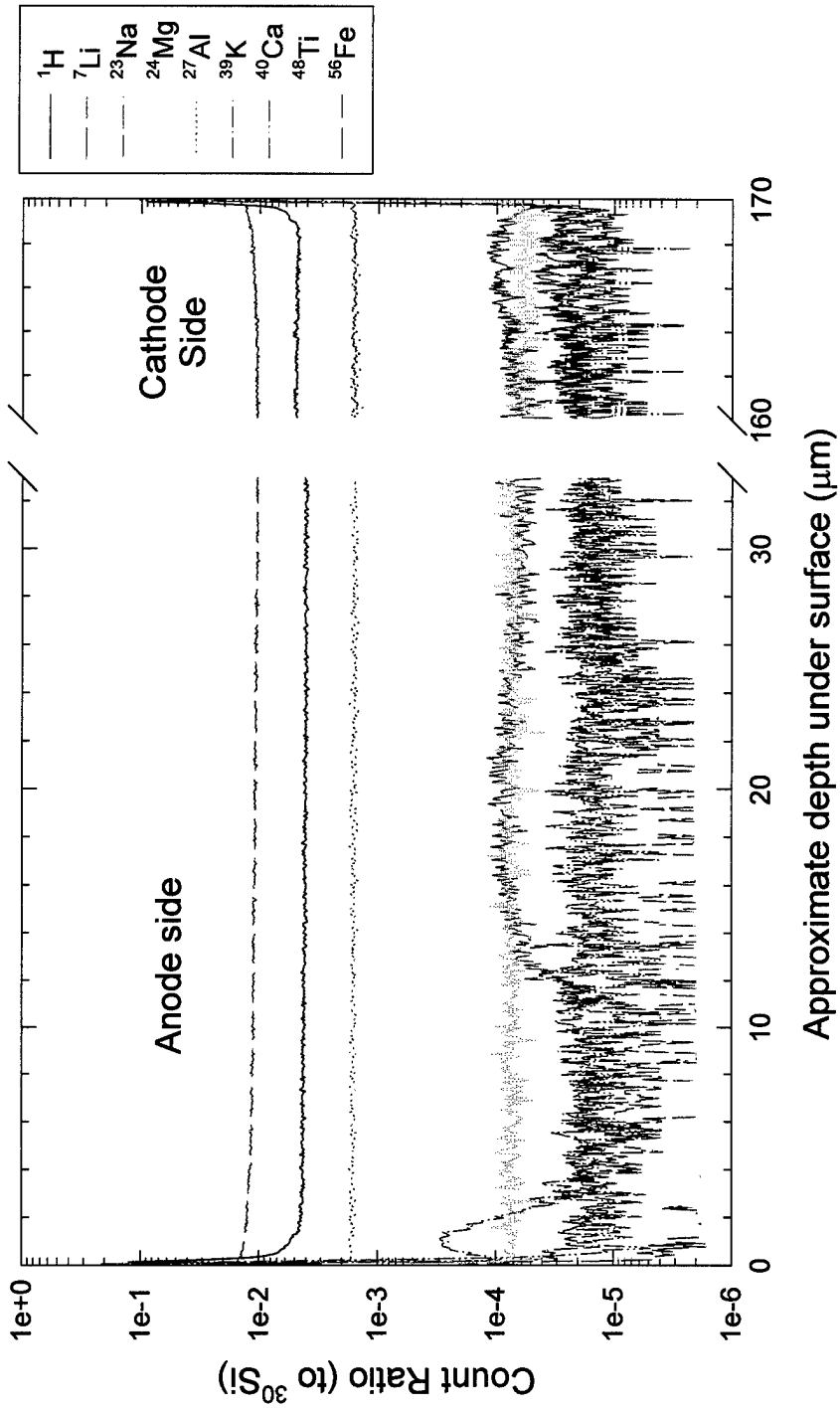
Figure 3.27 SIMS analyses of anode and cathode sides of a type II (Heraeus T08) fused silica cover slip poled for 20 min, at 4.3 kV, and ~275 °C

On the cathode side (Fig. 3.27) there is no depletion region. There is, however, a slight accumulation in Li peaking at 2-3 μm under the cathode surface. There is also a slight accumulation in Na as well peaking at 3-4 μm under the cathode surface.

In order to investigate the trend of the depletion region with poling time, four samples were selected to be analyzed using SIMS. The samples were poled at 4.3 kV, ~275°C and for 0.5, 2, 20, and 140 min, respectively. Pieces from these samples were also used in the etching experiment where the results are plotted in Fig. 3.20. Fig. 3.28 shows the result of SIMS analyses of the near-surface region on the anode side. For the sake of clarity, only H, Li, Na, K, and in graph (d), Ca are plotted. Li, Na, K, and Ca are plotted on a logarithmic scale, while H is plotted on a linear scale to highlight its distribution.

The first thing to notice in Fig. 3.28 is how both the Li edge and Na edge of their respective depletion layers move deeper into the sample with time. Taking a rough measurement of the depletion edges from these graphs, this trend is plotted along with the etching data in Fig. 3.29. The movement with poling time of the Li depletion edge correlates well with the movement of the second etching ridge.

Other features in Fig. 3.28 of which to take notice include the accumulation of Li between its depletion edge and the Na depletion edge. The location of the accumulation implies that extra Li ions are likely filling vacated Na sites. We see that with longer poling times, K appears to have been pulled into the glass from the surface. In graph (c), there was a well developed peak of K moving into the sample. In (d), there was also a peak, although not so well developed, that moved to the Li depletion edge. In (a) and (c), Na seems to have been injected from the surface, due to the gradual decrease extending to

(a) Poled 0.5 min

(b) Poled 2 min

(c) Poled 20 min

(d) Poled 140 min
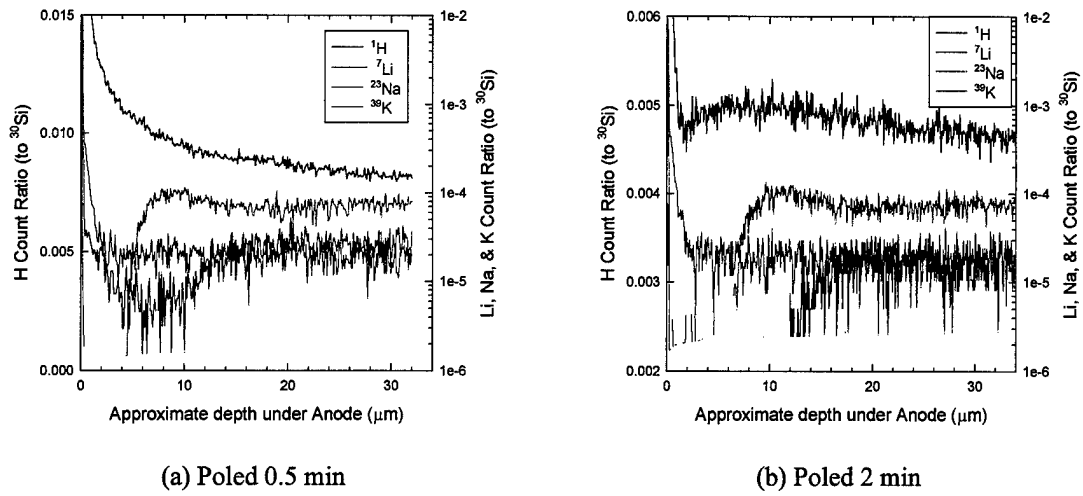
Figure 3.28 SIMS analyses of the anodic surface of samples poled for various times.
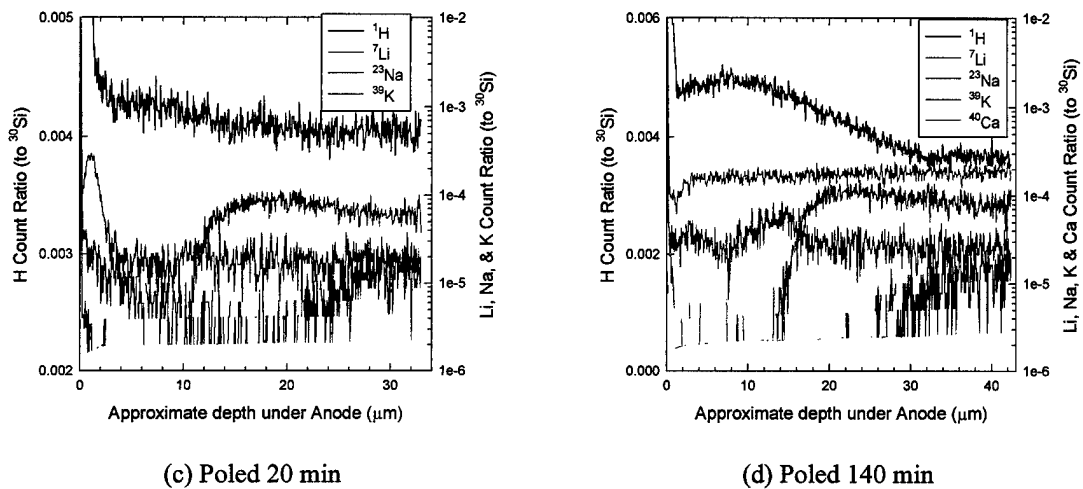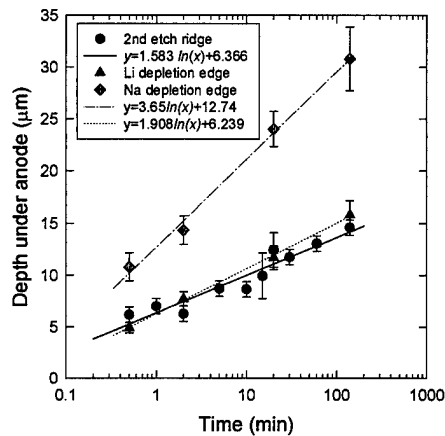

Figure 3.29 Trend with poling time of the depletion edge of Li and Na along with the second etching ridge from section 3.2.1. Also plotted are logarithmic fits for each data set.

the Li depletion edge. It is reasoned that the near-anode Na is injected and moves slowly, possibly due to clogged pathways. A similar near-anode accumulation is observed with a type III sample with much lower Na impurity levels, implying it was introduced at the surface (presented later, see Fig. 3.33). The lack of such a gradual decrease in (b) and (c) could be due to the different handling histories of the glass, leading to less surface contamination of alkali ions. In (d), the distribution of Ca was plotted to show that in this case of a long poling period, a small Ca depletion region began to form. No trend in the distribution of H is clear. In (a) and (c), there was a gradual decrease with depth into the sample to lower bulk values, although (a) had about twice the bulk count rate of H compared with the other samples. In (b) and (d), there was a peak that was ~10 μm into the sample. Interestingly, in (d), the peak of H decreased with depth to a steady level existing at the Na depletion edge; the larger concentration of H seemed to match the Na depletion region. The fact that there was no obvious trend in the H level could stem from the fact that prior to poling, each sample may start with different initial H distributions. Also, H in glass can exist in several forms as discussed in chapter 2. Because ionization rates may be different for one bonding form versus another, SIMS unfortunately does not tell us which ionized form of H, contributes most to the H distribution. The H distribution as detected by SIMS also does not make it clear if ions such as H_3O^+, are contributing to the total space-charge distribution.

A cover slip sample was poled for 5 min at 4.3 kV, ~275°C. After cooling with voltage applied, the sample was manually turned over and reheated with no voltage applied. Once heated to ~275°C, 4.3 kV was applied for 1.5 min before allowing the sample to cool with voltage still applied. Both sides of the sample were examined with

SIMS. The results are in Fig. 3.30. The behavior of the new anode side which is seen in Fig 3.30 was similar to the sample poled for 2 min (Fig 3.28 (b)), except the depletion edges did not move as far. On the new cathode side, we see some very interesting results.
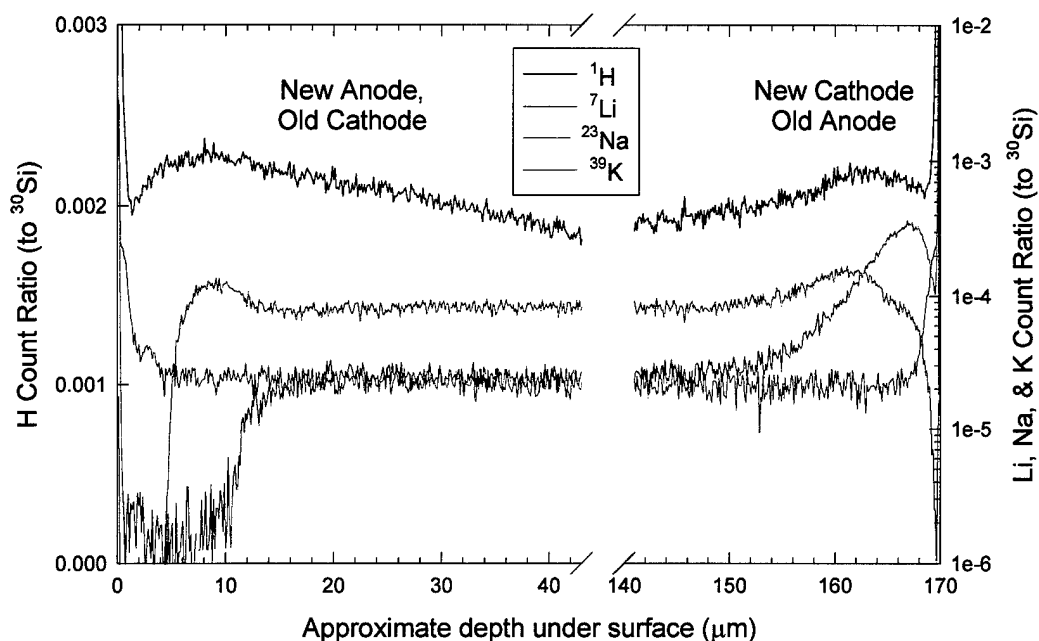
Figure 3.30 Effect of field reversal on cation distributions as measured by SIMS. The left side is the near-surface of the new anode, the right side is the near-surface of the new cathode.

First, it is helpful to remember that before field reversal, the new cathode side was the old anode, so a depletion layer existed in the near-surface region. When the field was reversed, Na ions were able to move through the Li ions, yet unable to push through completely to the outer surface. Na ions piled-up as if they were blocked by a resistive layer. A pile-up was also observed for the Li ions, just behind the pile-up of Na ions. The former depletion edge of Na has moved and disappeared at the surface, but the depletion edge of the Li ions was still evident very near the surface. This shows that Na motion is faster than Li motion. It also shows that Na can move through Li at the

impurity levels present in this glass, yet Na can be blocked by something else, perhaps by K or a hydrogenated species. The shape of the H distribution on the new cathode side is slightly different and the magnitude is slightly less than on the new anode side; it's possible that there is motion of some H species toward the new cathode.

An unetched piece of the sample shown in Fig 3.24 was analyzed with SIMS. This sample had been poled multiple times for a total of 155 min and finally depoled by shorting the sample to ground when heated. Fig. 3.24 showed how the sample still exhibited characteristic etching behavior (ridges and grooves). Fig. 3.31 shows the result from SIMS analysis of the anode side. As can be seen, the size of the Na and Li depletion regions is similar to the sample poled for 140 min (Fig. 3.28 (d)). There is also a wide peak of K, similar to the 140 min sample, but is not buried as deep in the sample. The H
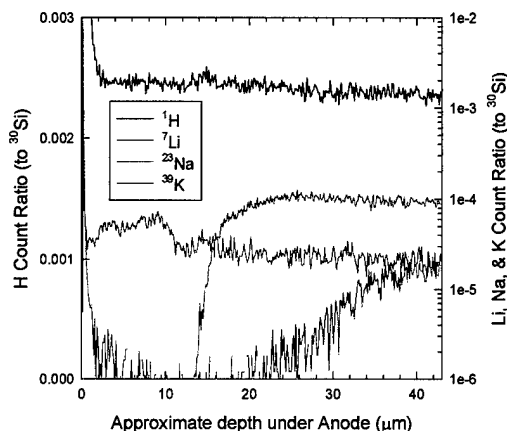
Figure 3.31 SIMS analysis of sample poled for a total of 155 min and subsequently depoled (short-circuited). Large Li and Na depletion regions remain.

distribution is quite different, but since the H distribution tends to vary from sample to sample, no conclusions can be drawn. Unfortunately, a poled piece of the sample was not preserved prior to depoling for comparison. One can conclude that Li and Na didn't move very far in the short time it was depoled (~1 min + cool-down). There was an electrical

138

current response as well as elimination of SHG. In order to eliminate the nonlinearity, charge had to move enough to cause the internal electric field to integrate to zero over a coherence length (matching the boundary condition of zero applied voltage). It isn't known which charge species moved.

The cover slip samples mentioned in the SIMS analyses above were type II fused silica from Heraeus Amersil that is commercially available as T08. Heraeus lists in its catalog[21] typical trace impurities that occur in its type I and type II fused silica. Table 3.6 shows the typical impurity levels from the manufacturer's catalog. Several fused silica samples, including Heraeus cover slips were also chemically analyzed using atomic absorption (AA) measurements. Table 3.7 shows the results in ppm by weight, along with Corning's reported Na and K levels for one sample (Corning Seacor). The measurement method used by Corning is unknown. The AA measurement of the Seacor sample is within 20% of Corning's stated level for K, but for Na, the AA measurement is twice that of Corning's level. The Heraeus cover slips show AA measured impurity levels much higher (20 to 52 times) than expected for type II samples listed in Table 3.6.

Table 3.6 Typical manufacturer's data for trace impurities in Heraeus Amersil fused silica

Impurity	Al	Ca	Cr	Cu	Fe	K	Li	Mg	Na	Ti
Types I & II (ppm)	20	1	0.1	0.1	0.8	0.8	1	0.1	1	1
Types III & IV (ppm)	0.05	0.05	0.005	0.01	0.02	0.01	0.01	0.005	0.05	0.05

Table 3.7 Atomic absorption chemical analysis of fused silica samples

Impurity	Na	K	Li	Fe	Al
Type II (Heraeus T08) Cover Slip #1	50	16	<0.4	<8	963
Type II (Heraeus T08) Cover Slip #2	52	24	<0.4	<9	488
Type II (Esco A1) Cover Slip	41	100	4.4	158	428
Type III (Esco S1-UV) Cover Slip	7.7	16	<0.1	50	373
Type II Seacor (Corning)	38	246	7.8	192	941
Corning Analysis of Type II Seacor	17	203			

The Type II Seacor fused silica sample listed in Table 3.7 was analyzed with SIMS. The 5.9 mm thick sample had been first poled approximately 4.5 years prior to the SIMS measurement. It was poled at ~275°C and 4.5 kV on two different occasions with the same polarity for 10 min. each time. The result is shown in Figure 3.32 for both the anode and cathode sides. Note that cation depletion is still present after 4.5 years. Because Na and K levels were given by the glass manufacturer, this sample was analyzed in order to roughly calibrate the count ratio observed through SIMS. The bulk ion SIMS count ratio for Na is ~3×10^{-4} for 17 ppm (Corning measurement) or 38 ppm (the AA measurement). In contrast, a Heraeus cover slip SIMS count ratio is ~2×10^{-5}, a factor of 15 less than the Corning Seacor sample. Yet the Na level in the cover slips was measured by AA to be larger than the Seacor sample, suggesting a higher SIMS count ratio should be measured as well. This discrepancy puts in doubt that the AA measurements represent true bulk impurity levels for the cover slips. It could be that matrix effects from different glass compositions affect SIMS measurements and led to the discrepancy. However, given that the fused silica samples are >99% pure SiO_2, it could also be expected that SIMS matrix effects should not play a large role in the different types of fused silica. The cover slip samples submitted for AA analysis were small and the amount was just barely sufficient for analysis. Because the samples were so small, it was possible that surface contamination was sufficient to cause inaccuracy of bulk impurity values.

The different impurity makeup present in the Seacor sample led to interesting behavior as also seen in Figure 3.32. For example, higher levels of K led to formation of a depletion region in K. There is even a slight depletion region formed for Ca

corresponding to the most depleted region of K, along with a small pileup of Ca located

in the lesser depleted region of K, which could have ion exchanged with K. Two dips in
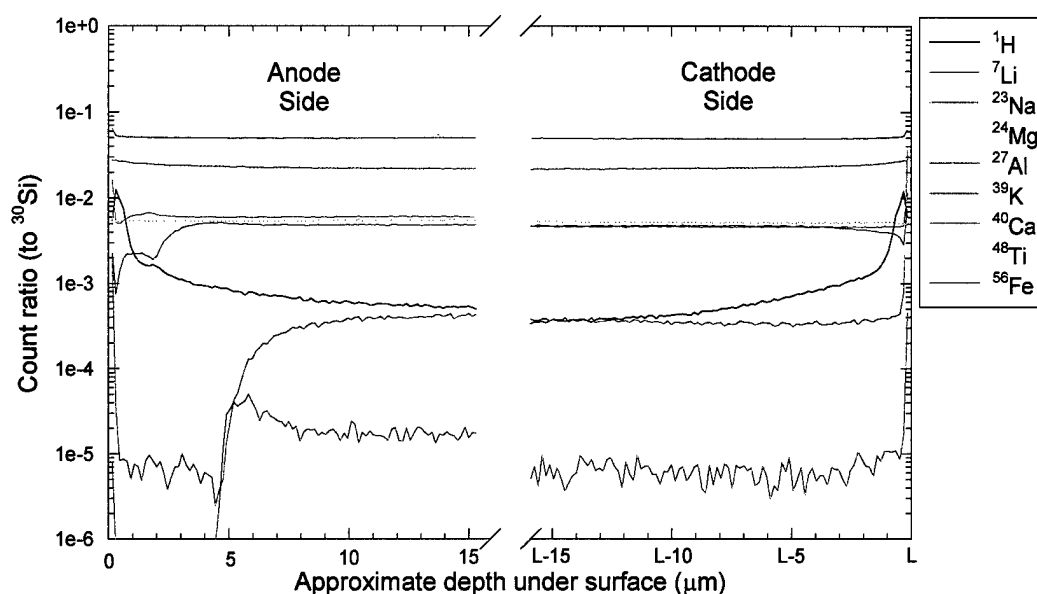
Figure 3.32 SIMS analysis of thick (5.9 mm) poled sample from Corning. The right side shows the near-surface anode side, the left side shows the near-surface cathode side.

the K depletion region correspond to peaks in the H distribution, implying H could ion

exchange with K. The larger peak of H corresponds to dips in the K distribution on both

the anode and the cathode sides, again suggesting ion exchange of H for K. A small

second dip in K on the anode side corresponds to a small peak in H.

The bulk count ratio of Li in the cover slips was ~8×10^{-5}. For the Seacor sample it

was ~1 to 2×10^{-5}, implying a lower impurity level than the cover slips. A smaller

impurity level should lead to a larger depletion width (to be discussed in chapter 4). In

the same vein, a larger impurity level should lead to a smaller depletion width. In the

Seacor sample, the relative depletion widths of Na and Li are about the same. In the

cover slips, the Na depletion region was about twice as large as the Li depletion. The

141

bulk count ratio of Na was 15 times larger in the Seacor compared to the cover slips, suggesting a larger impurity level of Na compared to the cover slips. The larger impurity level of Na led to a smaller depletion width relative to Li.

On the cathode side, it should be noticed that levels of Li and Na are 20 to 50 times higher in the very near-surface (<0.5 μm) region compared to the anode side, presumably from cation accumulation during poling. Yet, K, a slow-moving cation, still contains a small depletion region.

A type III fused silica cover slip (Esco S1-UV) was analyzed via SIMS. Normally, alkali impurities are expected to be <1 ppm in type III glasses. Table 3.5 shows otherwise for Na and K. However, the AA measurements are suspect of being inaccurate for the cover slips. Fig. 3.33 shows selected isotopes for the SIMS analysis of both the anode and cathode sides. The ~180-mm thick cover slip was poled at 5 kV, ~275°C, for 10 min, and showed SHG levels comparable to other samples, and did not require additional heat treatment. The SIMS analysis shows bulk count ratio levels for alkali impurities that are more than 10 times smaller than observed in type II cover slips. In fact, the bulk count ratios were near the instrument detection limit. In Fig. 3.33 anode side, one can see that both Na and K are injected into the glass, staying within 10 μm from the surface. A distribution peak of K was created between 2 to 8 μm below the anode, peaking at ~3 μm. A K depletion region formed in the first 2 μm as the peak moved into the glass. The SIMS data appears to be somewhat correlated with features observed in the etching experiment. The etching data of this sample (Fig. 3.25) showed a ridge formed from etching that was located between the surface edge and an etching groove that begins at ~2 μm and ends at ~3 μm below the anode. Thus, the etching

groove could very well be indicative of a gradient in the K charge distribution or, alternatively, in the field distribution.

On the cathode side (Fig. 3.33), there is also an accumulation of Na and K. The K accumulation is within 2 μm of the surface. The Na accumulation occurs within 20 μm of the cathodic surface, and is larger than the accumulation on the anode side. This is probably due to Na^+ migration towards the cathode during poling. The large gradual rise towards the cathodic surface in lieu of a sharp rise similar to that of K, would not be expected unless the migration pathways are clogged and the Na current backs-up, or alternatively, there are a very limited number of pathways to begin with. The clogged pathways could be due to other ions such as K or Ca, or it could be due to surface hydration. The H distribution has a similar shape, but the level is slightly lower on the cathode side when compared to the anode side. It appears that the near-surface shape of the H distribution, with its dip near the surface edges, somewhat matches the rise in the Na distribution. Also, the lower level of H on the cathode side matches a higher level of Na. The process of accumulating Na seems to be caused by ion exchange of Na for H in this sample.

The ability to thermally pole the type III sample and detect SHG without any additional treatment could be due to surface contamination of K. When poled, a small depletion region was created from surface injection of K. A high field associated with the K depletion region would then exist under the first 3 μm of the anode.
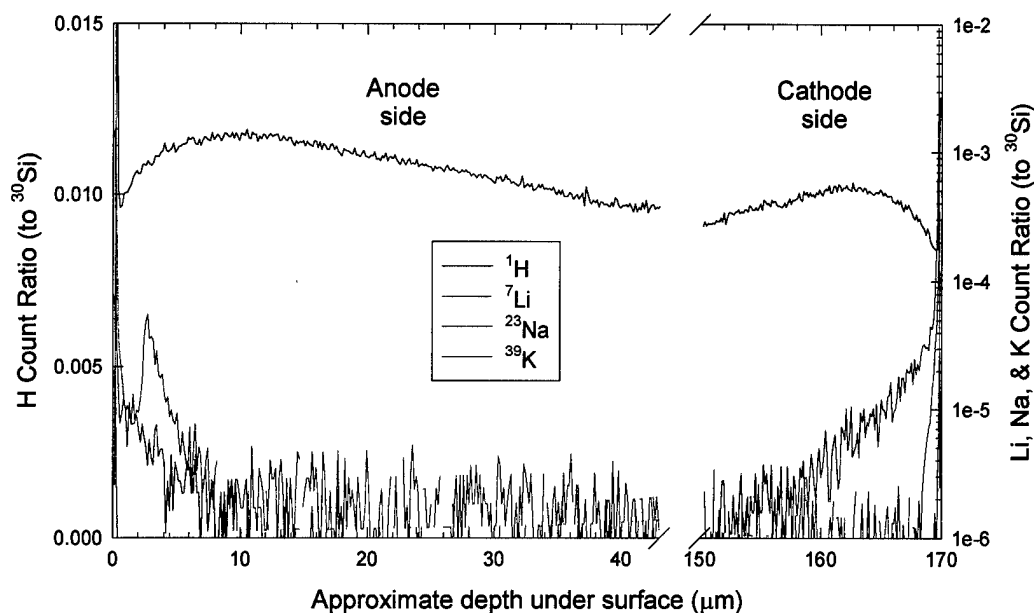
Figure 3.33 SIMS analysis of type III fused silica (Esco S1-UV) cover slip. The right side shows the near-surface cathode side, the left side shows the near-surface anode side. Poled at 5 kV, ~275°C, for 10 min.

3.2.3 Profiling summary

The etching data combined with the SIMS data showed:

(1) The alkali depletion region in type II glasses continues to move deeper into the sample with increased poling time at approximately a logarithmic rate, while the SHG signal level stays at comparable levels for all measured poling times. This indicates that the electric field (and consequently the $\chi^{(2)}$) must be varying dramatically.

(2) Na, K, and possibly a hydrogenated species are injected into the sample from surface contamination during poling. Ion exchange can occur, e.g. H can ion exchange for K, and Na can ion exchange for H.

(3) The second ridge (decreased etching rate) in the etching experiments correlates well with the edge of the depletion region, marked by Li. The groove (increased etching rate) appears to be associated with the accumulation peak of K, or

alternatively, with the edge of a second, slower-forming, depletion layer as K moves in from the surface.

(4) Migration of Na towards the cathode can be hindered near the cathode surface edge by other impurity accumulations (e.g. K and/or hydronium), causing "clogged" pathways, and causing the Na to "back-up" and "pile-up".

3.3 Evidence of water entering glass while poling

Current measurements showed that multiple time scales occur in the poling process. The SIMS data has shown that Na and K can be injected into glass from the surface. The migration of a fast ion such as Na can be limited by the presence of another ion such as K or by surface hydration. Because of extensive evidence of water entering glass in the literature (see chapter 2), it is hypothesized here that a hydrogenated ion such as hydronium (H_3O^+) is injected at the glass anode. Because SIMS does not differentiate between hydrogenated species in the glass, conclusions cannot be drawn from the SIMS H count ratio distribution about the presence of molecular water or hydronium. Two different methods of detecting surface injection of hydrogenated species were attempted.

3.3.1 Fourier transform infrared (FTIR) spectroscopic measurement

The absorbance spectra of several fused silica cover slips were taken using a Nicolet fourier transform infrared (FTIR) spectrometer. Each spectrum plotted was the average of 36 scans with a resolution of 2 cm^{-1}. Figure 3.34 shows the spectra collected. The figures show the difference between background absorption and spectra with samples in place. Graphs (a)-(c) show samples measured in a single-pass transmission. The plots

were normalized to the highest peak shown in the plot for comparison. The primary difficulty in making comparisons is that small differences in beam path (angle or length) can cause measurable differences in band intensities. Figure 3.34 (a) shows a poled and unpoled type II cover slip sample comparison using a MCT detector. Figure 3.34 (b) shows the same samples using a DTGS detector. The ripples are due to a Fabry-Perot interference. Absorption bands were identified using Davis and Tomozawa's study on water-related species in silica glasses.[22] The bands marked with an asterisk in (a) are identified as silica combination/overtone bands. The band structure between 3700 and 3500 cm^{-1} are identified as OH stretching bands. Bound and Free H_2O bands would show up between 3400 and 3200 cm^{-1} if they exist. No H_2O absorption structure is obvious in the transmission spectra. The peak seen between 2400 and 2300 cm^{-1} is an artifact of the fourier-transform difference between the background and the sample spectra that sometimes occurs, and should be ignored. Fig. 3.34 (c) shows a type III cover slip in single-pass transmission. The OH-related bands in the type III sample have a relatively higher absorbance than the type II samples, indicating higher OH content. Still, no H_2O-related bands are obvious. Fig. 3.34 (d) shows the absorbance spectra for the type II samples mounted in an attenuated total reflection (ATR) mode. In this case, the samples were mounted against a high index, infrared transmitting, KRS-5 (n=2.37 at 1000 cm^{-1}) prism. In the ATR mode, light is sent into the prism and is total internally reflected. When a sample is brought in contact with the totally reflecting surface of the ATR prism, an evanescent wave exists in the test sample, which is attenuated at wavenumbers corresponding to absorption bands. The evanescent wave only penetrates a limited depth (~1 to 2 μm)[23] of the sample, giving a near-surface absorption spectrum of the sample.

146
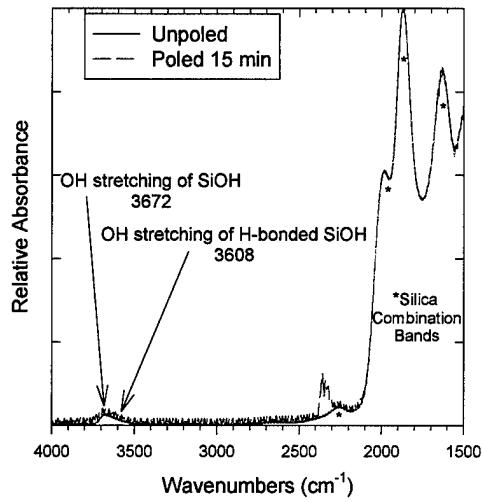
(a)
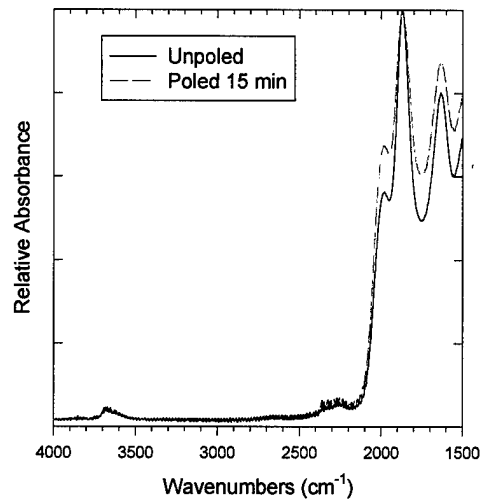
(b)
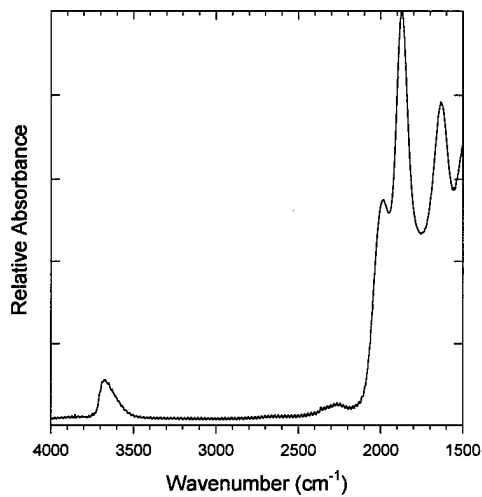
(c)
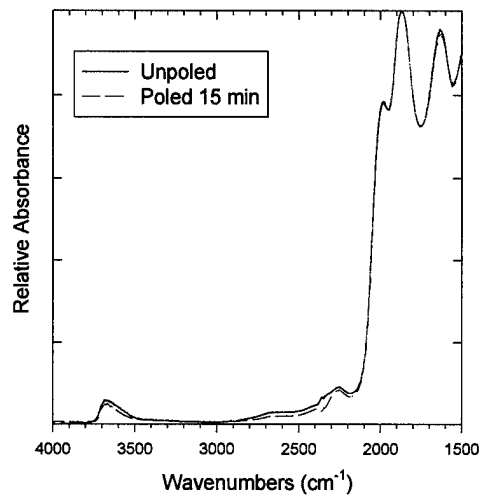
(d)

Figure 3.34 FTIR spectra of fused silica samples. All spectra are normalized to highest peak shown. (a) Shows the single-pass transmission spectra for a poled and unpoled Heraeus T08 (type II) cover slip using a MCT detector. (b) Same as (a), but using a DTGS detector. (c) Single-pass transmission spectra for a poled Esco S1-UV (type III) cover slip. (d) Attenuated total reflection spectra for a poled and unpoled Heraeus T08 cover slip.

Multiple reflections are possible by using a trapezoidal prism with angles cut at 45°. Two pieces of the sample can be mounted on opposite sides of the trapezoid, increasing evanescent absorbance.

Although the relative sizes of some of the peaks are different in the ATR spectra when compared with the transmission spectra, the same peaks are present. There is a rise in absorption observed between 2800 cm^{-1} and the silica combination band at ~2250 cm^{-1}. This might be another OH-stretching band of OH that is H-bonded to the oxygen of neighboring silanol groups.[22] The OH-stretching bands have a slight difference in absorption when comparing poled with unpoled samples. When the spectra are normalized to the highest peak, the poled sample has a lower OH absorption. This is tentative, however, because the difference may be entirely due to path difference in ATR prism alignment. As in the single-pass transmission experiments, there is no obvious absorption spectra due to H_2O species, and no significant difference was detected between the poled and unpoled samples in the H_2O absorption band (3400 and 3200 cm^{-1}).

Thus the FTIR experiment was unable to detect appreciable levels of water or H_3O^+ injection due to thermal poling. This might be expected however, because the samples in Davis and Tomozawa's study[22] required 10's to 100's of hours of hydration treatment in an autoclave bomb at elevated temperature in order to detect appreciable changes in H_2O-related absorption.

3.3.2 SIMS study of deuterated water injection

A 1.6-mm thick fused sample (Esco G1) was treated with deuterium (D) prior to

poling. This was accomplished by leaving the sample in heated (~ 100°C) deuterated

water (>99% D_2O) for 10 hours. The sample was then poled for 30 min. at 5 kV and

275°C. A peak SH signal comparable to the EG1A reference in section 3.1.1.3 was

measured. The sample was then analyzed using SIMS. Fig. 3.35 shows the result for

selected isotopes. A dip in the distributions of Na and Li indicate a depletion region. An
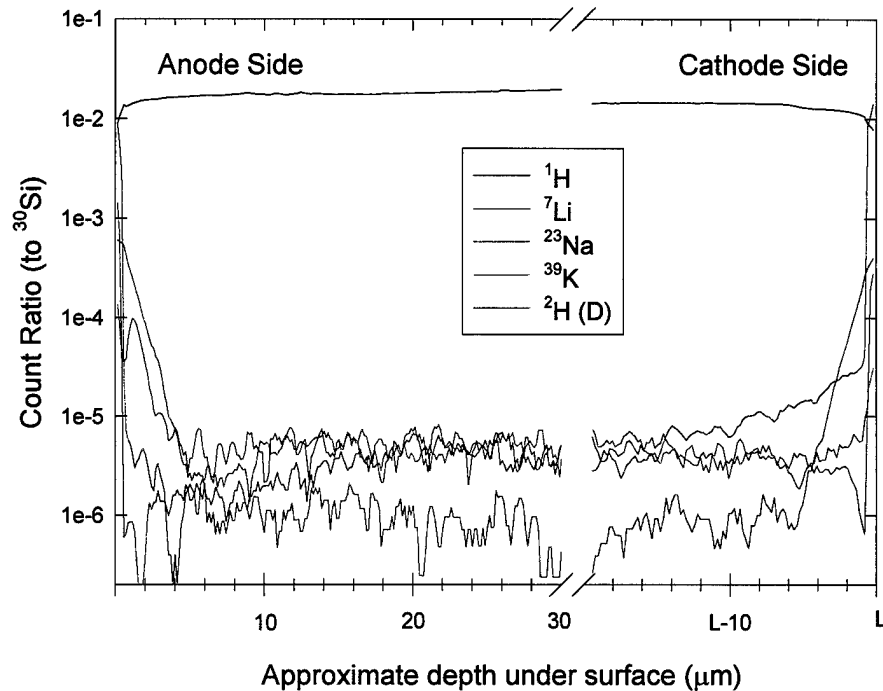
Figure 3.35 SIMS analysis of near-surface regions of deuterium-treated Esco G1 type II fused silica sample.

accumulation of Na over 10 μm under the cathode is also seen. The deuterium

distribution at both surfaces of the sample is compared in Fig. 3.36. There is ~ 50%

more D under the surface on the anode side than the cathode side. The difference in the

two curves shows that more D is brought into the anode side than the cathode side; whether or not this is a significant effect is undetermined.

(a)   (b)
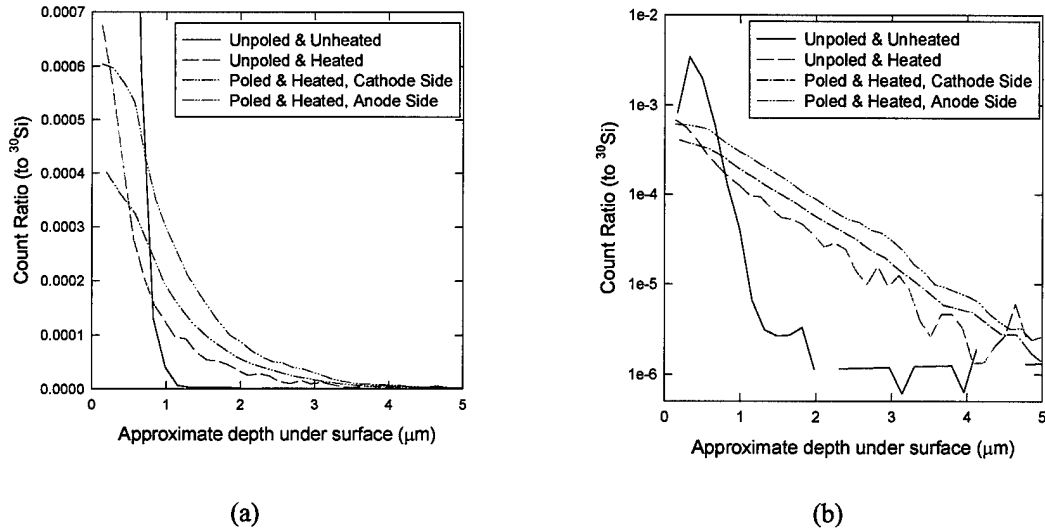
Figure 3.36 Comparison of deuterium distributions from SIMS analysis. (a) shows linear scale for the count ratio. (b) shows a logarithmic scale for the count ratio. The unpoled & heated sample wasn't heated at the same time as the poled sample; it may not be directly comparable to the poled sample.

The effect of thermal diffusion can be seen by comparing the unpoled sample distributions in Fig. 3.36. Thermal diffusion at 275°C causes significant in-diffusion of D from D_2O. An unpoled, unheated sample from the same treated glass can be compared with an unpoled sample that was heated for 30 min at ~275°C (although not at the same time as the poled sample). The thermal treatment decreases the D distribution within the first μm of the surface. The thermal treatment also causes diffusion of D deeper into the first 5 μm's of the sample.

The SIMS study of deuterated water injection leads to two conclusions: (1) thermal diffusion of water at the poling temperature occurs and significant amounts of H enter the glass in this manner. (2) More H enters the glass on the anode side than the cathode side, presumably from electric field injection of ionized forms of H.

3.4 References

[1] R.A. Myers, N. Mukherjee and S.R.J. Brueck, "Large second-order nonlinearity in poled fused silica," Opt. Lett., **16**, 1732 (1991).

[2] P.D. Maker, R.W. Terhune, M. Nisenoff, and C.M. Savage, Phys. Rev. Lett. 8, 21 (1962).

[3] R.A. Myers, *Large Second-Order Nonlinearity in Amorphous SiO$_2$ Using Temperature/Electric-Field Poling*, Ph.D. Dissertation, University of New Mexico (1995).

[4] M.J. Weber, ed., *CRC Handbook of Laser Science and Technology Volume III: Optical materials,* part 1, (CRC Press, New York, 1986).

[5] R.A. Myers, X. Long, and S.R.J. Brueck, "Recent advances in the second-order nonlinear optical properties of amorphous silica materials," in *Doped Fiber Devices and Systems*, Proc. M.J.F. Digonnet, ed., SPIE **2289**, 185 (1994).

[6] A. Kameyama, E. Muroi, A. Yokotani, K. Kurosawa, and P.R. Herman, "X-ray radiation effects on second-harmonic generation in thermally poled silica glass," J. Opt. Soc. Am. B **14**, 1088 (1997).

[7] J. Xu, X. Lu, H. Chen, L. Liu, W. Wang, C. Zhu, and F. Gan, "Second harmonic generation investigation on electric poling effects in fused silica," Opt. Materials **8**, 243 (1997).

[8] H. Nasu, H. Okamoto, A. Mito, J. Matsuoka, and K. Kamiya, "Influence of the OH content on second harmonic generation from electrically polarized SiO$_2$ glasses," Jpn. J. Appl. Phys. **32**, L406, (1993).

[9] L.J. Henry, A.D. DeVilbiss, and T.E. Tsai, "Effect of preannealing on the level of second-harmonic generation and defect sites achieved in poled low-water fused silica," J. Opt. Soc. Am. B **12**, 2037, (1995).

[10] R.W. Boyd, *Nonlinear Optics* (Academic Press, San Diego, 1992).

[11] D.W. Shin and M. Tomozawa, "Electrical and dielectric relaxation in silica glasses at low temperature," J. Non-Crys. Solids **211**, 237 (1997).

[12] W. Margulis, F. Laurell, and B. Lesche, "Imaging the nonlinear grating in frequency-doubling fibres," Nature **378**, 699 (1995).

[13] W. Margulis and F. Laurell, "Interferometric study of poled glass under etching," Opt. Lett. **21**, 1786 (1996).

[14] A. Agarwal and M. Tomozawa, "Correlation of silica glass properties with the infrared spectra," J. Non-Cryst. Solids **209**, 166 (1997).

[15] D.E. Carlson, K.W. Hang, and G.F. Stockdale, "Ion depletion of glass at a blocking anode: II, properties of ion-depleted glasses," J. Am. Ceram. Soc. **57**, 295 (1974).

[16] B. Lesche, F.C. Garcia, E.N. Hering, W. Margulis, I.C.S. Carvalho, and F. Laurell, "Etching of silica glass under electric fields," Phys. Rev. Lett. **78**, 2172 (1997).

[17] D.E. Carlson, "Ion depletion of glass at a blocking anode: I, Theory and experimental results for alkali silicate glasses," J. Am. Ceram. Soc. **57**, 291 (1974).

[18] C.M. Lepienski, J.A. Giacometti, G.F. Leal Ferreira, F.L. Freire Jr., and C.A. Achete, "Electric field distribution and near-surface modifications in soda-lime glass submitted to a dc potential," J. Non-Cryst. Solids 159, 204 (1993).

[19] R.G. Gossink, "SIMS analysis of a field-assisted glass-to-metal seal," J. Am. Ceram. Soc. **61**, 539 (1978).

[20] R.G. Gossink, "Application of secondary ion mass spectrometry (SIMS) to glass surface problems," Glass Tech. **21**, 125 (1980).

[21] Quartz glass for optical data and properties, Heraeus Amersil Inc., 3473 Satellite Boulevard, Duluth, GA 30136.

[22] K.M. Davis and M. Tomozawa, "An infrared spectroscopic study of water-related species in silica glasses," J. Non-Cryst. Solids **201**, 177 (1996).

[23]*The complete guide to FT-IR,* "Introduction to attenuated total reflectance (ATR) spectroscopy," 12-2 (1996), SpectraTech Inc., 2 Research Dr., Shelton, CT 06484.

Chapter 4 Modeling and Theory of the Space Charge Region

in Fused Silica

The formation of a second-order nonlinearity in thermally poled fused silica has

previously been discussed in the literature[1] in terms of a simple, single ionic carrier model

leading to an anodic depletion region of width $w_0 = \sqrt{2\varepsilon V/eN}$ [with ε the dielectric

constant, V the applied voltage, e the magnitude of the electronic charge and N the Na

density] under an applied dc electric field. This single carrier model is inconsistent with

experimental observations presented in the last chapter including: the peak in the

nonlinearity several μms under the surface; alternating polarity charge regions near the

anode; multiple time scales for establishing the nonlinearity dependent on the prior

thermal/voltage history of the sample; the presence of a nonlinearity under the negative

electrode under some conditions; and the fact that the depletion region as shown by SIMS

does not relax on the same time scale as the nonlinearity. Introduced in this chapter is a

two-carrier model including field-induced hydrogen-ion exchange driven by the large

fields in the depletion region that accounts for the hysteretic nonlinearity dynamics. A

qualitative fit is obtained with the experimental observations.

4.1 Space charge/depletion layer

There is a good deal of evidence supporting the establishment of a negatively

charged, depletion layer or space charge region in poled bulk fused silica. As mentioned

in the section on SIMS in chapter 3, several groups have observed a space-

charge/depletion region using ion probes. These observations are restated below along with some related observations on the space charge region. An early experimental measurement of a space charge region in fused silica was reported by Cohen[2] using metal foil voltage probes. At an applied potential of 10V, the majority of the applied potential developed across a thin region under the anode. Proctor and Sutton found similar results over a longer poling period in a relatively alkali-free glass using embedded foil probes.[3] Field-assisted glass-to-metal sealing in borosilicate glasses was observed by Wallis and Pomerantz to be associated with a space-charge layer depleted of sodium ions with a corresponding high electric field[4,5]. Gossnik used secondary ion mass spectrometry (SIMS) to analyze the field-assisted glass-to-metal seal in soda-lime silicate glass and found a near surface layer depleted of sodium, potassium, and calcium ions, and to a lesser extent magnesium and manganese ions.[6] Krieger and Lanford[7], as well as Lepienski et al.[8], measured a sodium and calcium depleted region in soda-lime glass after dc poling. Carlson[9,10] measured a cation-depleted region in a poled sodium silicate glass using ion scattering spectrometry, as well as confirming the formation of the depletion region with dc electrical measurements. Carlson[11] also attributed conduction in the high field depletion region of the sodium silicate glass to proton injection from the anode, as well as possible movement of some of the large underlying concentration of non-bridging oxygen ions. He et al.[12] modeled the development of the space charge region in glasses under room temperature and low applied potential conditions (1-10V), using a single carrier model, consistent with that first proposed by Myers et al.[13] for thermal poling.

4.2 Simplifications to the calculations

Diffusion is neglected in the transport equations and the charge densities are treated as columns of constant density. As shown below, this is appropriate for the formation of the space charge layers since the electrical energies are comparable to kT for scales much less than the depletion widths. However, this assumption breaks down when the fields are reversed and the fast ions are blocked by the slow ions. In the reversed field case, there is no variation in the local electric field and diffusion is the only active process.

In general the current equation contains two terms, a field conduction term and a diffusion term:

$$j = e\mu En + eD\left(\frac{\partial n}{\partial x}\right) \tag{4.1}$$

where e is the electronic charge, n is the ionic carrier concentration, and D is the diffusion coefficient, related to the mobility by the Nernst-Einstein relation $\mu = (eD/kT)$. The scale length Λ for which these two terms are approximately of equal importance can be estimated

$$e\left(\frac{eD}{kT}\right)En \approx eD\left(\frac{n}{\Lambda}\right) \tag{4.2}$$

and from Poisson's equation

$$E \approx eN\Lambda/\varepsilon \tag{4.3}$$

so,

$$\Lambda \approx L_D \approx \sqrt{\frac{\varepsilon kT}{e^2 N}} \tag{4.4}$$

where L_D is the Debye length for screening an external field from a free carrier plasma, and N is the fixed background negative charge density. At a temperature of 275°C and a background charge density of 1 ppm, L_D is approximately 30 nm. On the other hand, the depletion width is ~ 10 μm, or ~ 300 L_D, making the diffusion term negligible. Thus the approximation is made that:

$$j = e\mu En \tag{4.5}$$

which dramatically simplifies the numerical computations.

4.3 Single Carrier Model

When fused silica is thermally poled, the field in the space charge region can be quite large. For a first estimate, the field strength (E_{dc}) and space charge width (w_0) can be calculated following Von Hippel et al. [14], assuming a single ionic carrier. The development for the case of a single cationic carrier (e.g. Na$^+$) in fused silica is also given by Myers and can be found in detail in ref. [15]. For the sake of completeness, a similar development will be repeated here.

The poled sample can be divided into three regions as in Fig. 4.1. Region I will be the region depleted of the mobile cation, and region II will largely be unaffected. If the cathode is assumed to be totally blocking to cation movement, region III will consist of an accumulation of cations. If the cathode is non-blocking, cations will leave the sample and
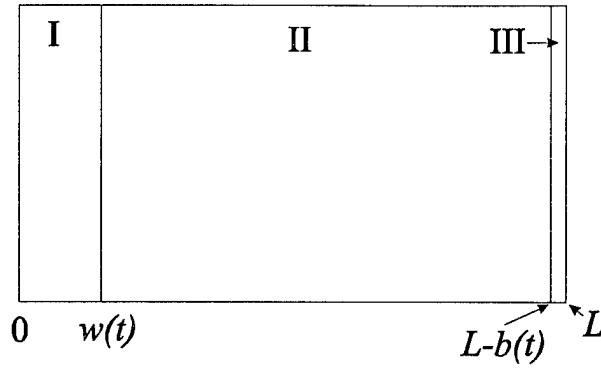
Figure 4.1 Three electric field regions in a poled sample. *w(t)* marks the edge of a single carrier depletion region under the anode; *b(t)* represents an accumulation region under the cathode.

there will be no region III. The assumption made here is that cations are at least partially blocked, that the cathode is what blocks the movement and that an accumulation region forms, but it is very small and occurs at the cathode surface.

The electric field in each region can be related to the charge density by Poisson's equation in one dimension (movement is largely in one dimension only):

$$\frac{dE_I}{dx} = \frac{-\rho^-}{\varepsilon} \quad \text{(region I)}$$

$$\frac{dE_{II}}{dx} = 0 \quad \text{(region II)} \tag{4.6}$$

$$\frac{dE_{III}}{dx} = \frac{\rho^+}{\varepsilon} \quad \text{(region III)}$$

where ε is the dielectric constant, the negative charge density is given by $\rho^- = eN^-$ and the positive charge density is given by $\rho^+ = eN^+$ and N is the charge number density and e is electronic charge.

157

When the three equations in (4.1) are integrated, we have:

$$E_I = \frac{-\rho^-}{\varepsilon} x(t) + C_I(t)$$

$$E_{II} = C_{II}(t) \tag{4.7}$$

$$E_{III} = \frac{\rho^+}{\varepsilon} x(t) + C_{III}(t)$$

C_I, C_{II}, and C_{III} are constants of integration and can be found by applying initial and boundary conditions. The initial condition at $t = 0$ is $E = V/L$ =constant in all three regions. V is the applied voltage and L is the total sample width. The boundary conditions require that the electric fields are continuous at the boundaries of the three regions. Therefore:

$$C_{II}(t) = C_I(t) - \frac{\rho^-}{\varepsilon} w(t)$$

$$C_{II}(t) = C_{III}(t) + \frac{\rho^+}{\varepsilon}(L - b(t)) \tag{4.8}$$

C_{II} can be eliminated, and all three electric fields can be written in terms of one constant such as C_I.

$$E_I = C_I(t) - \frac{\rho^-}{\varepsilon} x$$

$$E_{II} = C_I(t) - \frac{\rho^-}{\varepsilon} w(t) \tag{4.9}$$

$$E_{III} = C_I(t) - \frac{\rho^-}{\varepsilon} w(t) - \frac{\rho^+}{\varepsilon}(L - b(t)) + \frac{\rho^+}{\varepsilon} x$$

The constant C_I can be found by applying the voltage boundary condition that the integral of the electric field over all three regions must equal the applied voltage:

$$V = \int_0^L E\,dx = \int_0^{w(t)} E_I\,dx + \int_{w(t)}^{L-b(t)} E_{II}\,dx + \int_{L-b(t)}^L E_{III}\,dx \qquad (4.10)$$

After inserting eqn. 4.9 into 4.10 and doing some algebra, the following result is found for C_I:

$$C_I(t) = \frac{V}{L} - \frac{1}{\varepsilon L}\left\{\frac{\rho^- w^2(t) + \rho^+ b^2(t)}{2} - \rho^- w(t)L\right\} \qquad (4.11)$$

Another relation for C_I can be found from considering that current must be continuous across boundaries. Region I is traversed by displacement current $\left(\frac{\partial D}{\partial t}\right)$ only (all moving charges have left earlier).

$$J_I = \frac{\partial D}{\partial t} = \varepsilon\frac{\partial E_I}{\partial t} = \varepsilon\frac{\partial C_I}{\partial t} \qquad (4.12)$$

In Region II, there is displacement current and electrical current from moving charges:

$$J_{II} = -\rho^- \mu E_{II} + \varepsilon\frac{\partial E_{II}}{\partial t} \qquad (4.13)$$

where μ is the cation mobility. Setting J_I equal to J_{II}, we find that for C_I:

$$\mu C_I(t) = \frac{\rho^-}{\varepsilon}\mu w(t) - \frac{\partial w(t)}{\partial t} \qquad (4.14)$$

Combining equations 4.11 and 4.14, C_I can be eliminated and an expression for the time rate of change of the depletion region is found:

$$\frac{\partial w(t)}{\partial t} = -\frac{\mu V}{L} + \frac{\mu w(t)}{2\varepsilon L}\left\{\rho^- w(t) + \frac{\rho^+ b^2(t)}{w(t)}\right\} \qquad (4.15)$$

159

If we apply the condition that the depletion region, due to its trapped, immobile charges, will be much larger than the cathodic accumulation region, or $w(t) \gg b(t)$, the last term can be ignored and equation 4.15 becomes:

$$\frac{\partial w(t)}{\partial t} - \frac{\mu \rho^-}{2\varepsilon L} w^2(t) = -\frac{\mu V}{L} \qquad (4.16)$$

The solution to this equation is given by:

$$w(t) = w_0 \tanh\left(\frac{t}{2\tau}\right) \qquad (4.17)$$

where w_0 is the steady state depletion width given by

$$w_0 = \sqrt{\left(\frac{2\varepsilon V}{eN}\right)} \qquad (4.18)$$

and the time constant is given by

$$\tau = \sqrt{\frac{\varepsilon L^2}{2eN\mu^2 V}} \ . \qquad (4.19)$$

The behavior of equation 4.17 is shown in Figure 4.2. With a single positive
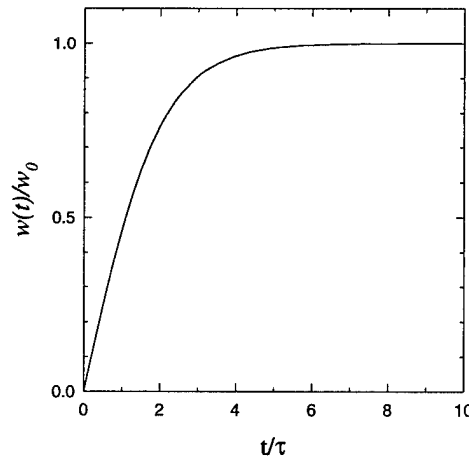

Figure 4.2 Behavior of a single carrier depletion width with time, based on equation 4.17.

160

carrier, a negatively charged depletion width is expected to form and reach a steady state

on a time scale of several τ.

In regions I & II, the electric field is now given by:

$$E_{dc} = \frac{eN}{\varepsilon}(w_0 - x) \quad 0 < x < w_0$$
$$= 0 \qquad\qquad x > w_0$$

(4.20)

where E_I is now written as the dc electric field E_{dc}. Because the width of region III is

assumed to be very small (b ~ 0), the potential drop (integrated electric field) in region III

is approximately $V_{III} \sim E_{III}b \sim 0$, and can therefore be ignored. This is a valid assumption

only if $w >> b$. The single-carrier model makes no provision for a wider accumulation

region, because only the cathode itself is assumed to be blocking. Because V in region III

is negligible, the SHG power from region III is negligible as well because it is

proportional to the square of the voltage drop by:

$$P_{SHG} \propto \left| \int E_{dc} e^{2\pi i x / l_{coh}} dx \right|^2 \approx \left| \int E_{dc} dx \right|^2 \propto V^2.$$

(4.21)

Thus in the single carrier model, the SH signal is only expected to originate from the

anode side depletion region. As demonstrated in chapter 3, moderate SH signals have

occasionally been observed to originate on the cathode side and are evident in both *in-situ*

measurements and in Maker fringes with frozen-in fields.

The simple model can be summarized schematically in Fig. 4.3. The figure shows

positive-negative charge pairs before applying an external electric field. Once the electric

field is applied, the cations (Na$^+$ ions) move to the thin region at the cathode, leaving a

negatively-charged depletion region due to negative charge sites that are fixed in the glass

matrix. The figure shows the charge distribution, internal electric field and potential difference associated with the different regions in the glass after the depletion region has formed.
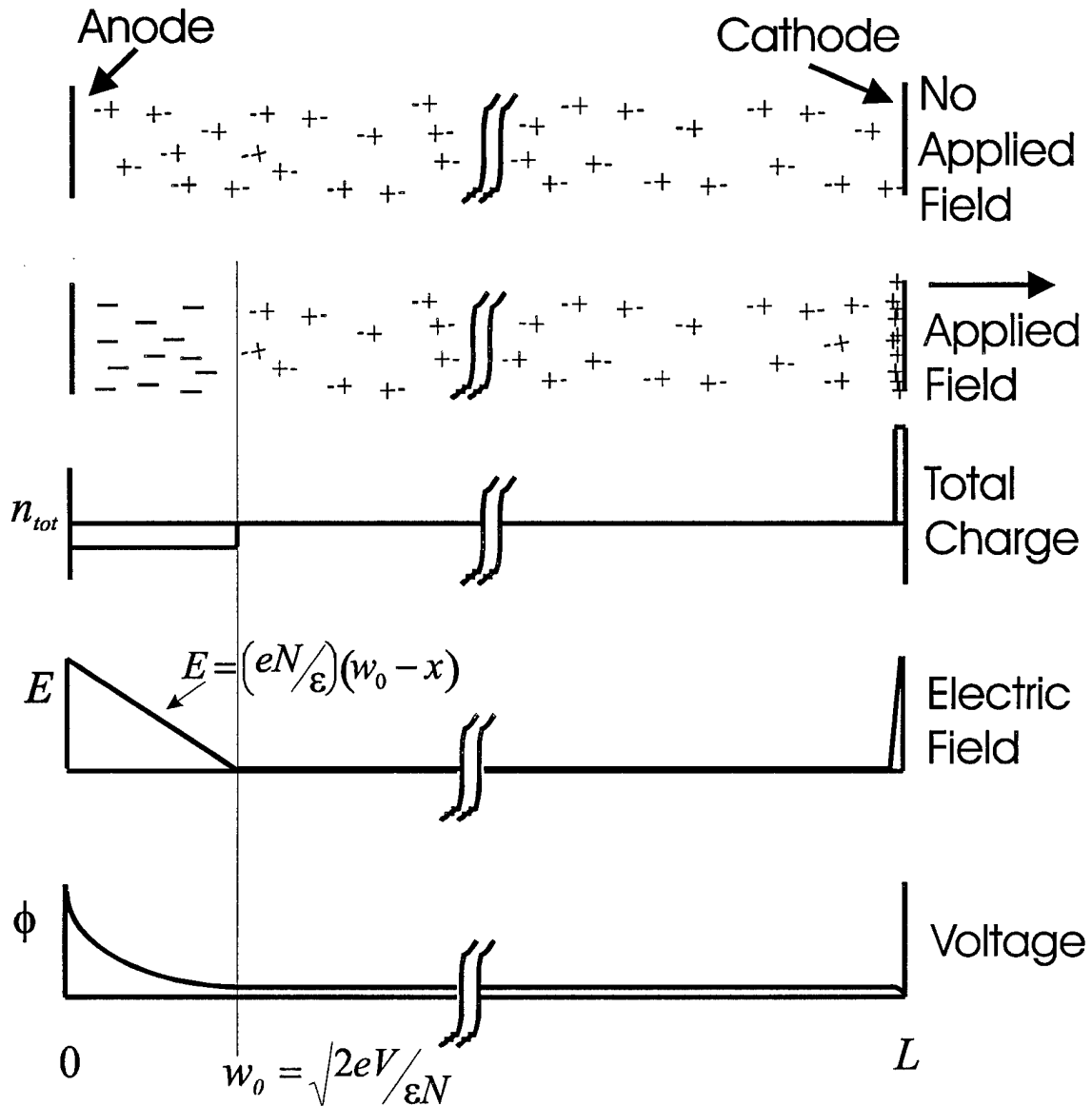

Figure 4.3 Schematic representation of single-carrier depletion region.

The charge density N can be estimated by considering that when the cations move, they leave behind an equal density of immobile, negatively charged non-bridging oxygen hole centers, NBO$^{\cdot}$. The Na concentration[16] in type II, electrically-fused silica is ~ 1 ppm

or $\sim 2 \times 10^{16}$ cm^{-3} (also see Table 3.6). A depletion width is calculated to be $w_0 \sim 10$ μm and a peak electric field is calculated as $E_{dc} \sim 1 \times 10^7$ V/cm occurring at the surface for $\varepsilon = 3.8\varepsilon_0$. This peak electric field strength approaches the nominal fused silica breakdown field strength, $E_{bd} \sim 3 \times 10^7$ V/cm.[16] The calculated depletion width is in qualitative agreement with initial results[13] for the extent of the nonlinearity, as well as order of magnitude agreement with the etching and SIMS results presented in chapter 3. However, as seen in chapter 3, observations have shown that the near-anode region is not adequately described with a simple depletion width model.

4.4 The two-carrier model

4.4.1 Assumptions and approximations for the two-carrier model

In order to describe the observed dynamic behavior of the second-order nonlinearity in glass, it is asserted here that the space charge region and associated high electric field are affected by injection of a secondary ionic species. If we assume that water, present either as surface moisture or already diffused into the glass, is injected in the form of a positively charged, hydrogenated species (e.g. hydronium, H_3O^+), the evolution of the space charge, field, and signal strength can be simulated.

Several assumptions are necessary to fit the experimental data presented in chapter 3:

(1) A fast carrier is required to explain processes that occur on fast (10's of seconds) time scales (see for example Fig. 3.12). The fast carriers are taken to be Na^+ ions.

(2) A second, slower positive carrier is needed to explain slow processes. It is proposed here that they are hydrogenated ions. It is also possible that potassium, from surface contamination, can fill this role as seen in the SIMS measurements. As was

mentioned in section 2.2.4.1, two groups[17,18] found $\mu_K \sim 10^{-3}$-$10^{-4} \, \mu_{Na}$ in fused silica at 350-380°C, and one group[19] found $\mu_H \sim 10^{-4} \, \mu_{Na}$ at 800-1300 °C. For the sake of consistency, this model will refer to the slow ions as H^+ or H_3O^+, although it is not critical that the slow ion be related to hydrogen.

(3) The presence of a SH signal under the new cathode can be accounted for by a buildup of excess positive charge as the slow positive carrier is swept into the high field space-charge region at the anode. A voltage drop will occur over this region on field reversal <u>only</u> if the buildup leads to a positive charge accumulation in excess of the background charge density. This voltage drop then leads to a SH signal.

(4) After field reversal, as the excess positive charge is pushed back out, the sodium ion movement is effectively slowed by the presence of the low mobility ions. The sodium ions do not move independently of the slow ions.

(5) Diffusion during this blocking phase results in a mixture of hydrogen and sodium ion concentrations; the resulting mobility is between that of sodium and hydrogen ions. We are forced to make this assumption by our neglect of diffusion processes. A more complete model including diffusion may encompass this effect as well.

4.4.2 Analytical approximation to the two carrier model

An approximate analytical calculation can be made for the slow ionic carrier by starting with the single carrier model and assuming the fast carrier moves fast enough to be in equilibrium at all times. This approximation allows ion exchange of the slow carrier as a column of positive charge that matches the underlying negative charge

(NBO⁻) concentration. The initial condition for this calculation is the partial formation of the single (fast) carrier depletion region. The simplification is made that the fast ions move instantaneously in comparison with the slow ions. This is analogous to the Born-Oppenheimer approximation decoupling electronic and ionic motions because of the large mass differences. This is appropriate for the large mobility ratio between the slow and fast ions in fused silica and can help in developing a physical intuition. The electric field for a depletion region of constant negative charge is shown in Fig. 4.4 (a). E_p is the peak electric field at x = 0 and is given by equation 4.20 as

$$E_p = \frac{eN}{\varepsilon} w_F \qquad (4.22)$$

where w_F is the fast ion's depletion width.

As the slow ion moves in, it pushes the depletion region marked by w_F further into the sample. The extent to which the slow ion's column of charge moves in is marked by w_s and because this region is assumed to be neutral in this approximation, the electric field is flat, as shown in Fig. 4.4 (b). E_p will increase until the integrated electric field equals the total external applied voltage.
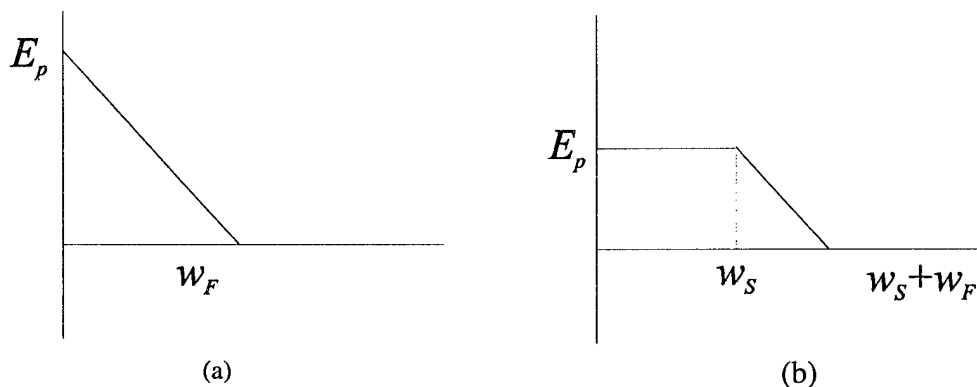

(a)   (b)

Figure 4.4 The electric field under the anode for (a) the fast single carrier model (b) the two carrier analytical approximation.

The rate at which the slow column of charge enters the sample is dependent on its mobility (μ_s) and the electric field it encounters and is given by:

$$\frac{d}{dt} w_s = \mu_s E_p \qquad (4.23)$$

The slow ion will move in until the integrated electric field matches the external applied voltage V. This is simply found by finding the area shown in Fig. 4.4 (b):

$$E_p w_s + \frac{1}{2} E_p^2 \frac{\varepsilon}{eN} = V \qquad (4.24)$$

The positive solution of this quadratic equation is obtained as a function of w_s:

$$E_p(w_s) = -\frac{eN}{\varepsilon} w_s + \frac{1}{\varepsilon} \sqrt{eN\left(eN w_s^2 + 2V\varepsilon\right)} = \frac{eN}{\varepsilon}\left[-w_s + \sqrt{w_s^2 + \frac{2V\varepsilon}{eN}}\right] \qquad (4.25)$$

Equation 4.23 can now be entered into equation 4.25, and the result is

$$\frac{d}{dt} w_s = \frac{\mu_s eN}{\varepsilon}\left[-w_s + \sqrt{w_s^2 + w_0{}^2}\right] \qquad (4.26)$$

where w_0 is the single carrier depletion width given by $\sqrt{\frac{2V\varepsilon}{eN}}$. By using a substitution of variables, equation 4.26 can be rewritten as

$$\frac{d}{d\tau} \omega_s = -\omega_s + \sqrt{\omega_s{}^2 + 1} \qquad (4.27)$$

where $\tau = \frac{\mu_s eN}{\varepsilon} t = \frac{t}{t_s}$ and $\omega_s = \frac{w_s}{w_0}$. This equation can be integrated to give

$$\tau = \frac{1}{2}\left(\omega_s{}^2 + \omega_s \sqrt{\omega_s{}^2 + 1} + \operatorname{arcsinh} \omega_s\right) \qquad (4.28)$$

Note that when comparing equations 4.22 and 4.25, and using the change of

variables, the normalized depletion width $\omega_F = {}^{w_F}\!\!/_{w_0}$ can be given in terms of ω_s:

$$\omega_F = -\omega_s + \sqrt{\omega_s^2 + 1} \qquad (4.29)$$

A graphical solution for ω_s is found by plotting equation 4.28. This is plotted in

Fig. 4.5 along with equation 4.29, showing the approximate behavior of the normalized

depletion width edge versus time (normalized to $t_s = \frac{\varepsilon}{\mu_s e N}$). The long term behavior of

ω_s (and $\omega_s + \omega_F$) is given by $\omega_s \approx \omega_s + \omega_F \propto \sqrt{\tau}$. Thus a two carrier model will predict

continuous migration of the depletion edge into the sample with time. The analytical

approximation given here, however, will not explain other phenomena such as the SH

signal (and inferred space-charge) observed under the cathode. This requires a better

approximation which will be given by numerical simulation and is described in the next

section.

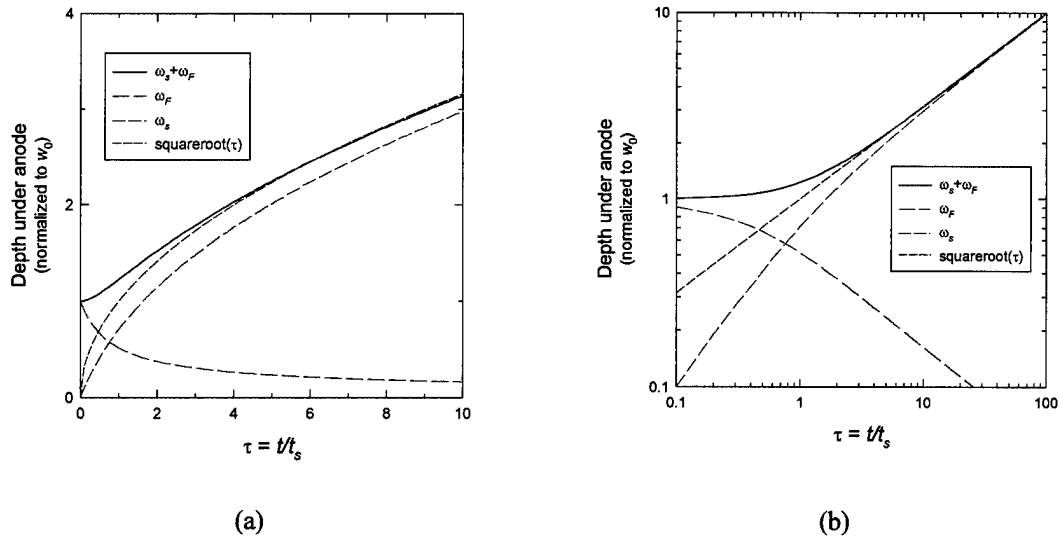(a)   (b)

Figure 4.5 Approximate behavior of the depletion region as predicted by analytical calculation of two-carrier model. (a) shows linear scales while (b) shows logarithmic scales.

4.4.3 Development of the numerical two-carrier model

The injection of hydrogen at the surface is described with the continuity equation:

$$\frac{\partial j}{\partial x} = -e\frac{\partial n_H}{\partial t} \tag{4.30}$$

where j is given by equation 4.5. Differentiation of j leads to

$$-\frac{\partial n_H}{\partial t} = \mu_H E \frac{\partial n_H}{\partial x} + \mu_H n_H \frac{\partial E}{\partial x} \tag{4.31}$$

The hydrogen charge distribution, n_H, can be evaluated by using a simple backward differencing method provided E is known. The electric field is found from Poisson's equation :

$$E(x) = C - \frac{e}{\varepsilon}\int_0^L n_{tot}(x')dx' \qquad 0 < x < L \tag{4.32}$$

subject to the circuit condition that the total voltage drop across the sample equals the applied voltage, V. If only the Na ions are mobile, a further condition for the steady-state is that $E(x \geq w) = 0$, otherwise the Na ions would move in response to a non-zero field. (This is in the approximation that allows decoupling of the fast and slow ionic motions.) Thus, C is given by:

$$C = \frac{e}{\varepsilon}\int_0^w n_{tot}(x')dx' \tag{4.33}$$

When Na^+ ions move, a depletion region of immobile negatively charged non-bridging oxygen hole centers NBO^- remains leading to a large electric field buildup. In response to

this field, slow positive H ions are drawn into the depletion region with a charge

distribution $n_H(x)$. The total charge distribution is then given by

$n_{tot}(x) = n_{Na}(x) + n_H(x) - N$. The initial and boundary conditions for the charge

distributions are:

$$n_{tot}(0 < x < L, t = 0) = 0$$
$$n_{tot}(x = 0, t) = +\eta_H$$

(4.34)

where η_H, the charge density at the surface, is an adjustable parameter that describes the

injection of hydrogen. As the fast Na^+ column of charge moves in response to the applied

electric field, its edge moves into the sample marking the edge of the depletion region.

The charge distribution in the depletion region is approximated by a constant level of

fixed negative charge equal to the Na charge density.

$$n_{tot}(0 < x < w, t) = -N$$

(4.35)

It is again assumed that there is negligible voltage drop under the cathode. This

corresponds to either a non-blocking cathode, or a blocking cathode in which the

accumulation region is very small compared to the depletion region. Recent SIMS results

(e.g. Fig. 3.30) show that sodium ions can be slowed or blocked in a region under the

cathode much broader than that assumed here. As a first approximation, however, it will

be assumed that Na^+ ions only accumulate in a small enough region such that the voltage

drop is negligible. Because the great majority of the potential drops across the space

charge region after Na^+ ions move, we can estimate the total potential difference that is

applied to the sample as:

$$\Delta V \cong -\int_0^w E(x')dx' \qquad (4.36)$$

where w is the width of the space charge region. This can be calculated numerically via the trapezoidal rule. The trapezoidal rule approximates the integration of ΔV as:

$$\Delta V \cong -\frac{w}{m}\sum_{k=1}^{m}\frac{E_{k+1}+E_k}{2} \qquad (4.37)$$

m is the number of spatial (Δx) divisions and k labels the kth Δx division so that $E_k = E(x = k\Delta x)$. Because in this equation ΔV is proportional to w, w can be calculated, given $E(x)$ and ΔV.

The initial electric field is $E(x,t = 0) = V/L$. Given a suitable time step, the movement of the Na^+ charge column is calculated in the electric field. The uncovered charge in the newly created depletion region allows calculation of a new electric field distribution and associated voltage drop. The field-driven injection of the slow ion into the depletion region is calculated within the time step, and again the electric field and voltage drop are recalculated to reflect the new charge distribution. This procedure is iterated. The Na^+ charge column movement is initially rapid, but slows as the voltage drop in the depletion region matches the external applied voltage. Movement of the depletion edge will continue, however, due to the continuing injection of the slow ion, which lowers the depletion region voltage drop and allows a small electric field across the sample to move the Na column once again.

4.4.4 Model results

4.4.4.1 Unlimited supply of slow ions

Figure 4.6 shows a simulation of the evolution of the total charge density

distribution under the anode as slow positive hydrogenated ions, present at the surface,

are pulled into the sample by the space-charge field. Charge density and field

distributions are shown for several positive poling times ranging to an hour for a 5-mm

thick sample. For this example calculation, a mobility of 2 x 10^{-13} cm^{2}V^{-1}s^{-1} was used for

hydrogen (based on Hetherington *et al.*'s[20] H to Na mobility ratio of $M = 10^{-4}$ and Page *et*

al.'s[21] 2 x 10^{-9} cm^{2}V^{-1}s^{-1} value for sodium mobility). The values of the mobilities are

uncertain quantities with large ranges reported in the literature as discussed in section

2.2.4.1. Regardless of what values are assumed for the mobilities, the important quantity

in regards to the simulation is the mobility ratio. Simulation results can be given in terms

of the characteristic time scale of the slow ion as seen in Fig. 4.6 and given in section

4.3.3 as $\tau_H = \frac{\mu_H eN}{\varepsilon} t$. In order to be consistent with the experimental observation of a

nonlinearity under the cathode after field reversal, it is necessary to have a positive charge

accumulation above the background charge density near the surface (assumption 3).

Within the model, this is provided by adjusting η_H to a level 10 times greater than the

background negative charge density. A level of $\eta_H = 10\,N$ was found to be a nominal

value that illustrated the effects of positive charge accumulation well. Larger levels of η_H

did little to change the positive charge accumulation. Lower levels produced smaller

charge accumulations and were less effective in illustrating the effects of positive charge

accumulation. For this simulation, η_H is constant with time, i.e. there is an unlimited
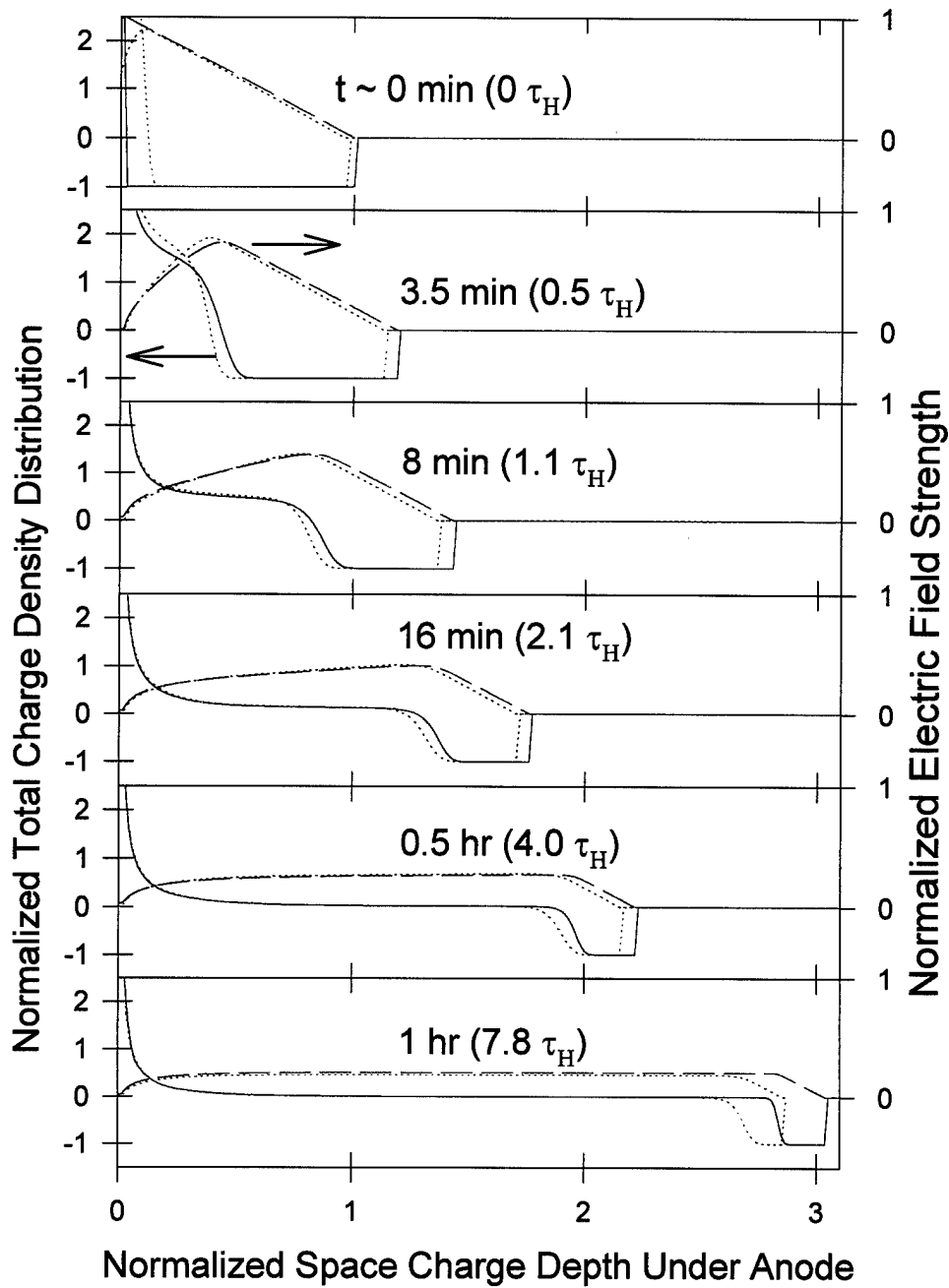
Figure 4.6 Two-carrier (fast Na, slow H) numerical simulation of development of space charge region using +5 kV applied voltage for a 5 mm thick sample with mobility ratio of $M = 10^{-4}$. Red dashed lines represent electric field, blue solid line represents total charge density distribution assuming Na moves instantaneously compared with H. Red and blue dotted lines represent calculated field and charge when Na is given a finite mobility. $\tau_H = \frac{\mu_H eN}{\varepsilon} t$ is the characteristic time scale of the slow ion. The total charge density is normalized to the background negative charge density.

172

supply of hydrogen ions. This simulates the case where substantial water is available, either from the poling atmosphere or from prior hydration of the glass. The simulation proceeds on the time scale of the slow ion. Two simulations are shown. In one (solid and dashed lines), the fast Na ions essentially equilibrate themselves instantaneously to the movement of slow H ions, i.e. the calculation allowed the Na ions to have an infinite mobility. For the dotted lines, the fast Na ion movement is calculated with a finite mobility, 10^4 times greater than H. The differences in the calculation are minor, with significant differences happening only with long poling times. The assumption that Na^+ ions move instantaneously is justified if the mobility ratio M of hydrogen to sodium is $M \ll 1$.

Before any H^+ motion; at t ~ 0 min., a negative space charge or sodium depletion region results from the t > 0 min. movement of Na ions upon application of the applied voltage. At later times the slow H ions start to move, resulting in the positive charge accumulation that is shown in the left hand side of the graph. Note that a double layer of positive charge followed by negative charge is formed. The depletion region moves deeper into the sample and becomes smaller with time, as predicted with the analytical calculation in section 4.3.3.

The electric field is modified at the same time as also shown in figure 4.6. The fields are calculated from the charge distributions using Poisson's equation. A total potential difference of 5 kV is applied across the electrodes. The peak of the electric field moves deeper into the sample with time. This is consistent with experimental observations that the peak SHG value is embedded somewhat in the sample as mentioned in section 1.2.3.1. As the peak moves inward, the peak field strength diminishes. We see

that after about an hour, the peak field strength is below 20 percent of its initial value. The SH signal strength should be relatively constant as it is proportional to V^2 as long as the region is less than or equal to the 1.06 μm coherence length (approximately 25 μm).

If the sample thickness used in the calculation stays the same (5 mm), but the mobility ratio is smaller, as shown in Fig. 4.7, with a mobility ratio of $M = 10^{-2}$, we have a situation similar to field-assisted ion exchange. Hydrogen is exchanged for sodium. The sample may develop a depletion region, but it is smaller and the electric field here only builds up to one tenth the value in the initial case. As the depletion region moves deeper into the sample, the slow ion distribution is able keep pace. This will occur when the fast and slow ions' velocities, given by the products of the mobility with the electric field, are approximately equal, as in $\mu_H E_H \approx \mu_{Na} E_{Na}$. The result of this is that there is a negligible depletion region, charge neutrality can be assumed and most of the voltage is dropped across the entire sample width: $E_{Na}L \sim V$ as long as the depth of the interface is $\ll L$.

As will be shown in section 4.3.5.4, if the calculation is done for a thinner sample ($L = 0.18$ mm) with $M = 10^{-2}$, less ion-exchange and more depletion region development is seen. This is because the initial electric field, $E_{Na} = V/L$, is larger when L is small and V is fixed, leading to higher velocity of the Na charge column.

The mobility ratio $M = 10^{-4}$, puts this calculation in a regime different than traditional field assisted ion exchange. For field assisted ion exchange, the fields are much lower, and if a space charge develops, it is not of much importance, because it will move along with the incoming ions. For the simulations of interest here, H^+ ions move a great deal slower than the Na^+ ions.
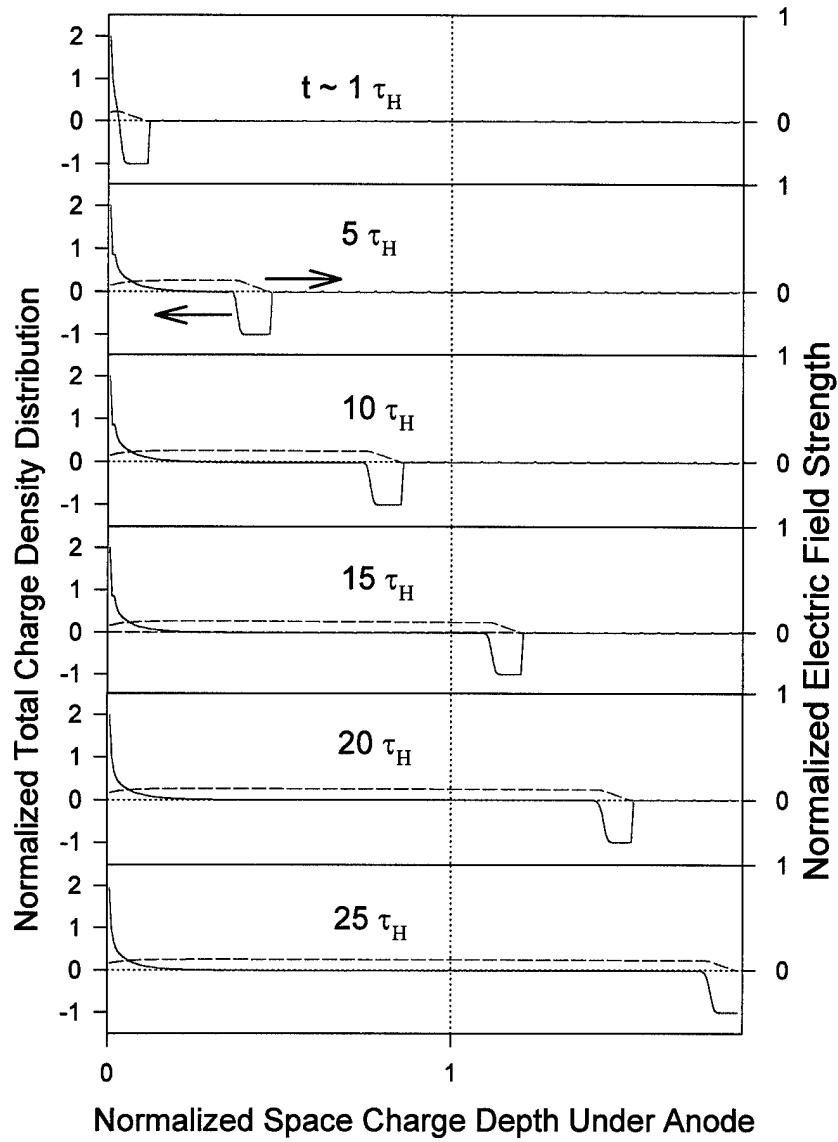
Figure 4.7   Numerical simulation of space charge development from 5 kV applied voltage for 5 mm thick sample and a mobility ratio of 10^{-2}.

4.4.4.2 Short circuit (after space-charge field is established)

If the poling circuit is subsequently short-circuited, the integrated area under an electric field curve is the potential difference, and is forced to equal zero. The electric

fields and charge distributions adjust to meet this condition, and are shown in Fig. 4.8 for

various poling times. When the circuit is shorted, some Na ions move back to the

left towards the sample surface. However, a somewhat smaller depletion region still

remains in order to satisfy the condition of $\Delta V = 0$. This assumes no other space charge

regions exist in the glass, including the opposite side, giving zero electric field across the

rest of the sample. For long poling times, the depletion region edge moves relatively little

from its position prior to being short circuited (compare with dotted lines in Fig. 4.6).

This is consistent with the SIMS and etching data of a short-circuited sample presented in

chapter 3.

(a)   (b)

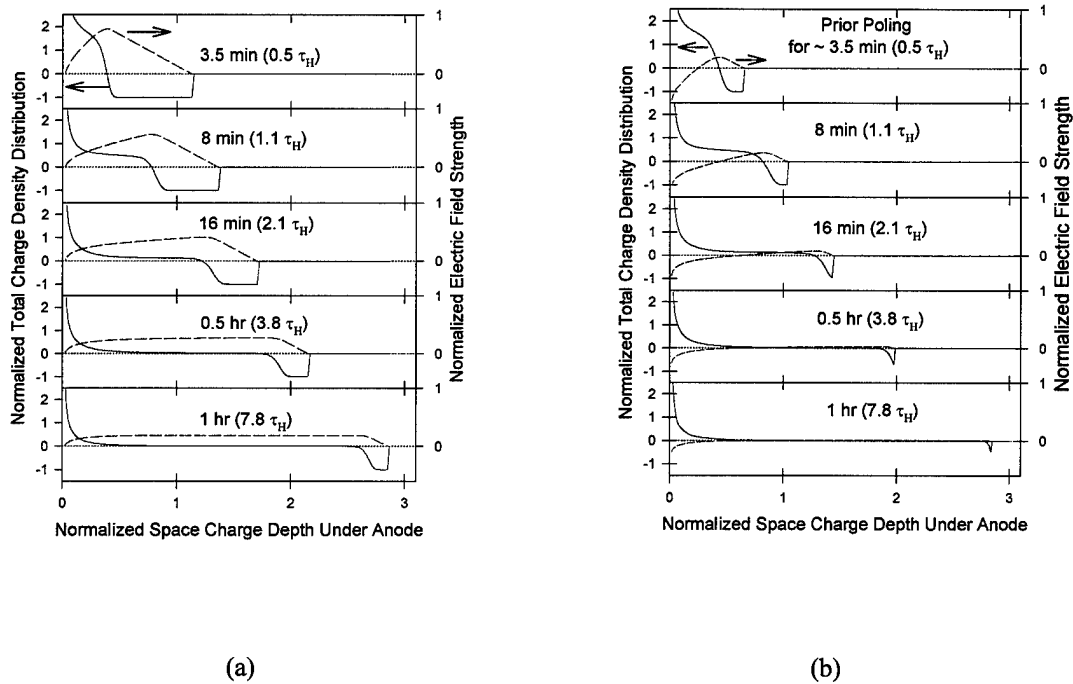Figure 4.8 Comparison of field and charge distributions for the space-charge region of a 5-mm sample (a) after being poled for various times and (b) immediately after switching to ground (0 voltage) after being poled for various periods of time at 5 kV. In (b), the electric field (marked in red) integrates to zero. This simulation assumes no other space charge regions exist in the glass, including at the other electrode.

4.4.4.3 Field Reversal

If the polarity of the applied field is completely reversed from +5 kV to -5 kV, the result is shown in Fig. 4.9. Because of the accumulation of positive charge at the sample surface from the injection of the slow H ion, there will still be a substantial electric field under this new cathode. When the field is reversed, Na ions move back towards the new
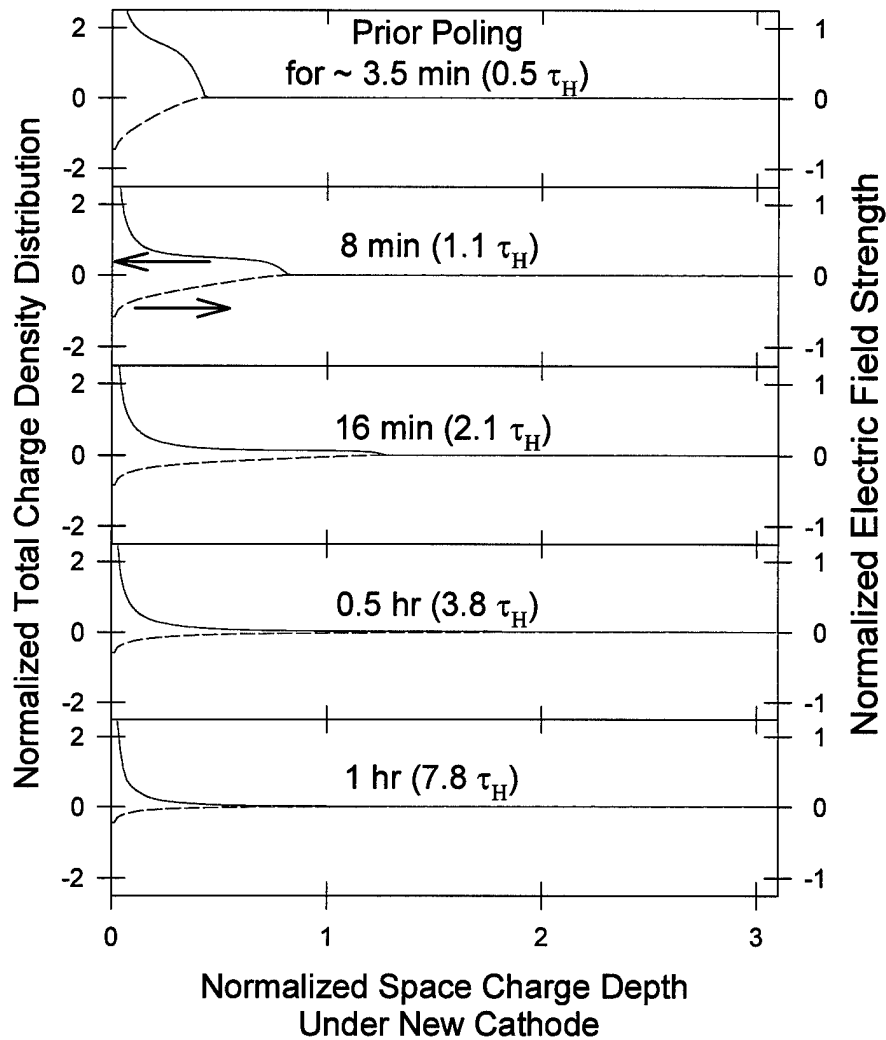

Figure 4.9 Numerical simulation of space-charge region after field reversal (+5 kV to -5 kV) for a 5-mm thick sample with $M = 10^{-4}$.

cathode, erasing the old depletion region and moving until they run into the positive charge distribution. At this point we are forced to make the assumption that the Na^+ ions cannot move through the positive charge accumulation and the movement of the front is blocked. This assumption is forced by the observation of the incubation period as presented in section 3.1.2 (e.g. Figs. 3.9, 3.14-15). The blocked movement of the Na^+ charge column hinders the formation of a depletion region at the new anode (not shown here), hence the incubation period. Some evidence of blocking of Na^+ movement after field reversal was also given by SIMS measurement (see Fig. 3.30).

After the old depletion region is erased, there is zero field across the sample up to the point where there is positive charge. At that point an electric field exists that is opposite in polarity to that which existed prior to reversal. If one integrates the negative field, the potential drop under the new cathode is found. Figure 4.10 shows the potential difference V under the new cathode as a function of the period of time which the sample was previously poled at +5 kV. For instance, in this simulation, if a sample is poled for ~ τ_H (~ 450 s) and then the field is reversed, a voltage drop of ~ 1500 V will occur under this new cathode. The potential difference under the new cathode is highly dependent on how the positive charge density is distributed and its resultant electric field. A uniform positive charge distribution throughout the space charge region would lead to a linear electric field and higher potential difference when the field is integrated. The curvature in the field causes lower calculated values for the potential difference. The largest potential difference in this calculation occurs at ~ τ_H.
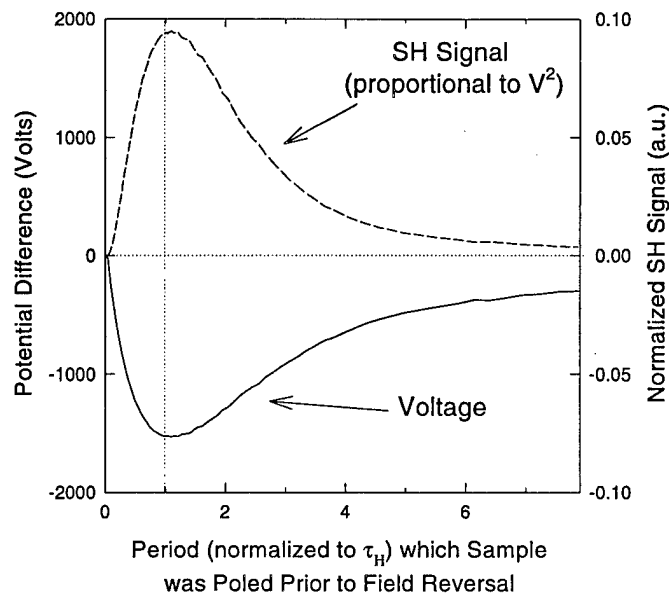
Figure 4.10 Calculated voltage drops and SH signal levels found under the new cathode versus the period of time which the sample was poled prior to field reversal.

The voltage drop due to the positive charge buildup leads to a SH signal at the new cathode. The relative intensity value for the SH signal is proportional to V^2 as in equation 4.16. The relative SH signal immediately after field reversal is also shown in figure 4.10. Qualitatively, this shows why one can detect a SH signal under the new cathode immediately after field reversal.

During the period of time of the incubation period, i.e. when the Na^+ is blocked, a relatively high current is observed (e.g. Fig. 3.9 or 3.17). If Na^+ is blocked, something else must provide the current. A displacement current is unlikely because the depletion region is not yet forming (high current = no resistive layer) and as a result there are not yet significant change of fields with time. The likely cause is the outward movement of the slow positive ion. For the specific poling time of 500 s (~ τ_H) at +5 kV, the calculated evolution of the charge and field under the new cathode with the field reversed

179

is plotted in figure 4.11. This simulation assumes Na^+ motion is blocked by the positive charge accumulation, but does not pile-up. Fig. 4.11 shows that as the slow H ion leaves the sample, the positive charge density distribution diminishes during 300 sec ($0.66 \tau_H$). Again, by calculating V^2, we see in figure 4.12 the corresponding change in SH signal strength under the new cathode as H leaves the sample. Thus the signal produced under the new cathode will diminish with poling time at a rate determined by the slow ion's mobility and the electric field.

4.4.4.4 Limited supply of slow ions

If hydrogen blocking electrodes are used, prior surface hydration, will act as a limited supply of H. To illustrate this condition, Fig. 4.13 shows the time evolution of the electric field and space charge for a 180-μm thick sample. In this case a sodium mobility of 10^{-11} cm^{2}V^{-1}s^{-1} was used in order to simulate experimental observations for the poling of a thin sample. An H mobility of 10^{-2} μ_{Na} was also used, but a smaller mobility would be equally valid to illustrate what happens with a limited supply of H. As the depletion region first forms, H is immediately pulled into the sample. In this case we see the positive charge buildup as before, but on a shorter time scale due to the thin sample and resultant larger initial electric field (V/L). At 90 sec, the supply of H runs out and a pulse of slow positive charge moves into the sample. As it does, a negatively charged depletion region once again forms at the anodic surface resulting in a triple layer of negative-positive-negative charge, with an electric field peak at the anodic surface and another deeper within the sample. The injection of a limited supply of slow H ions might explain the alternating polarity regions of charge measured with the LIPP technique[22]. If potassium plays the same role as slow H ions, the injection of a limited supply of K at the
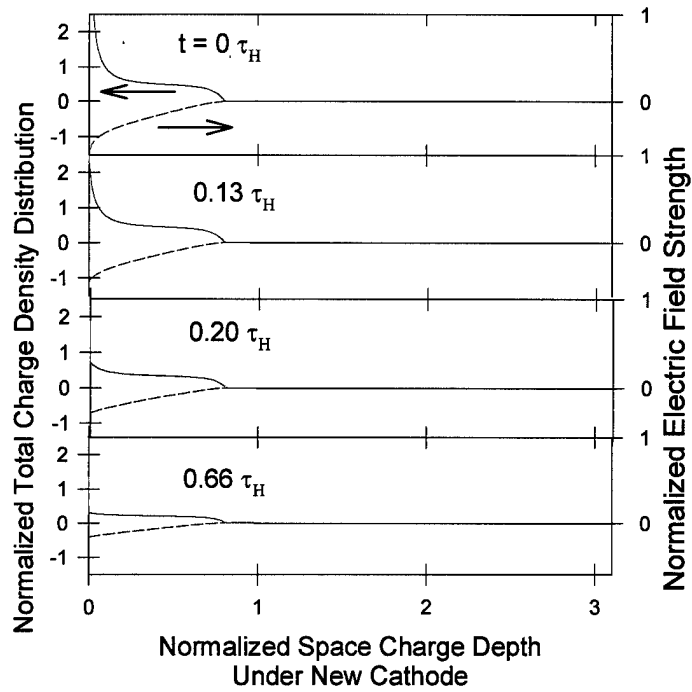
Figure 4.11 Calculated evolution of field and charge under new cathode with reversed poling time. The sample had previously been poled for ~ 500 s (~ τ_H) prior to field reversal.
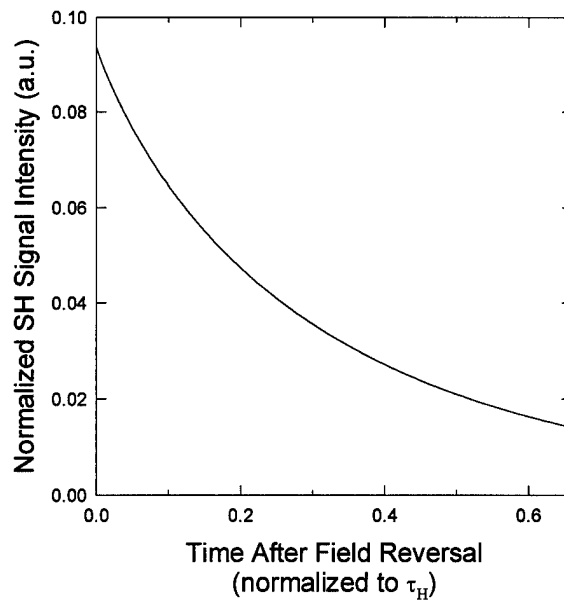
Figure 4.12 Calculated evolution of SH signal under new cathode with reversed poling time.

181

surface can help explain the near-surface depletion region seen developing in the

distribution of K measured with SIMS in Fig. 3.28 (c) & (d).

Figure 4.13 Evolution of electric field and total charge density under a limited supply of slow H ions at the surface. This calculation used a sample width of 180 μm and mobility ratio of $M = 10^{-2}$. At t = 90 s, the supply at the anode surface of H ions was set to zero.

4.4.4.5 Comparison of model to experimental data

Figure 4.14 shows the evolution of the total charge density distribution for an applied voltage of +5kV assuming that there is a negligible space charge region at the cathode. Several poling times up to 10 minutes are shown for a 6-mm thick sample. For this example several parameters are fit to the experimental observations (e.g. Fig. 3.12): $\mu_{Na} = 5 \times 10^{-9}$ cm^{2}V^{-1}s^{-1} (to fit the fast rise/fall times of 30 s); $\mu_H = 2 \times 10^{-13}$ cm^{2}V^{-1}s^{-1} (largely set by the fit to the slow 20-min. rise time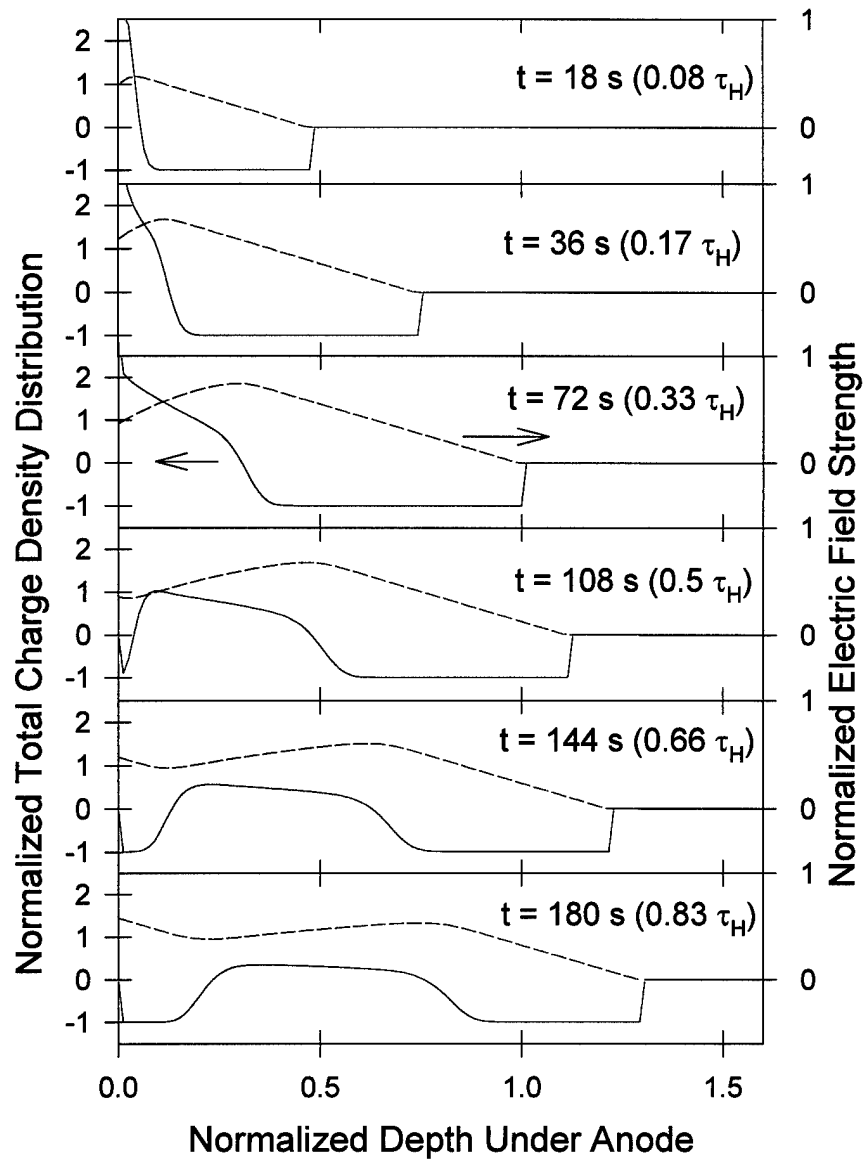s). The slow ion charge density at the surface, η_H, is adjusted to a level 10 times greater than the background negative charge density. For this simulation, η_H is constant with time, i.e. there is an unlimited supply of hydrogen ions.

At 13 s from the application of the voltage (Fig. 4.14a), the Na ions have moved towards the cathode to partially form the depletion region and a strong anodic field has been established. The x-axis is normalized to the single-carrier depletion width, w_0. After 40 s (Fig. 4.14b) there has been some H-ion injection from the anode and the Na-depletion width has adjusted to maintain the overall voltage drop across the space-charge region. The depletion width is able to adjust because the ion injection changes the field distribution, lowering the voltage drop in the space-charge region. The remaining voltage is dropped across the rest of the sample causing a non-zero field which allows Na$^+$ to readjust until the total voltage is once again dropped across the space-charge region. The position of the peak electric field has moved in from the surface. These trends are continued for longer times of 5 and 10 min.(Figs. 4.14c &d): H continues to be pulled in by the field forming a double layer of positive and negative charge, but at a decreasing rate because the field is decreasing; the edge of the depletion region moves further into

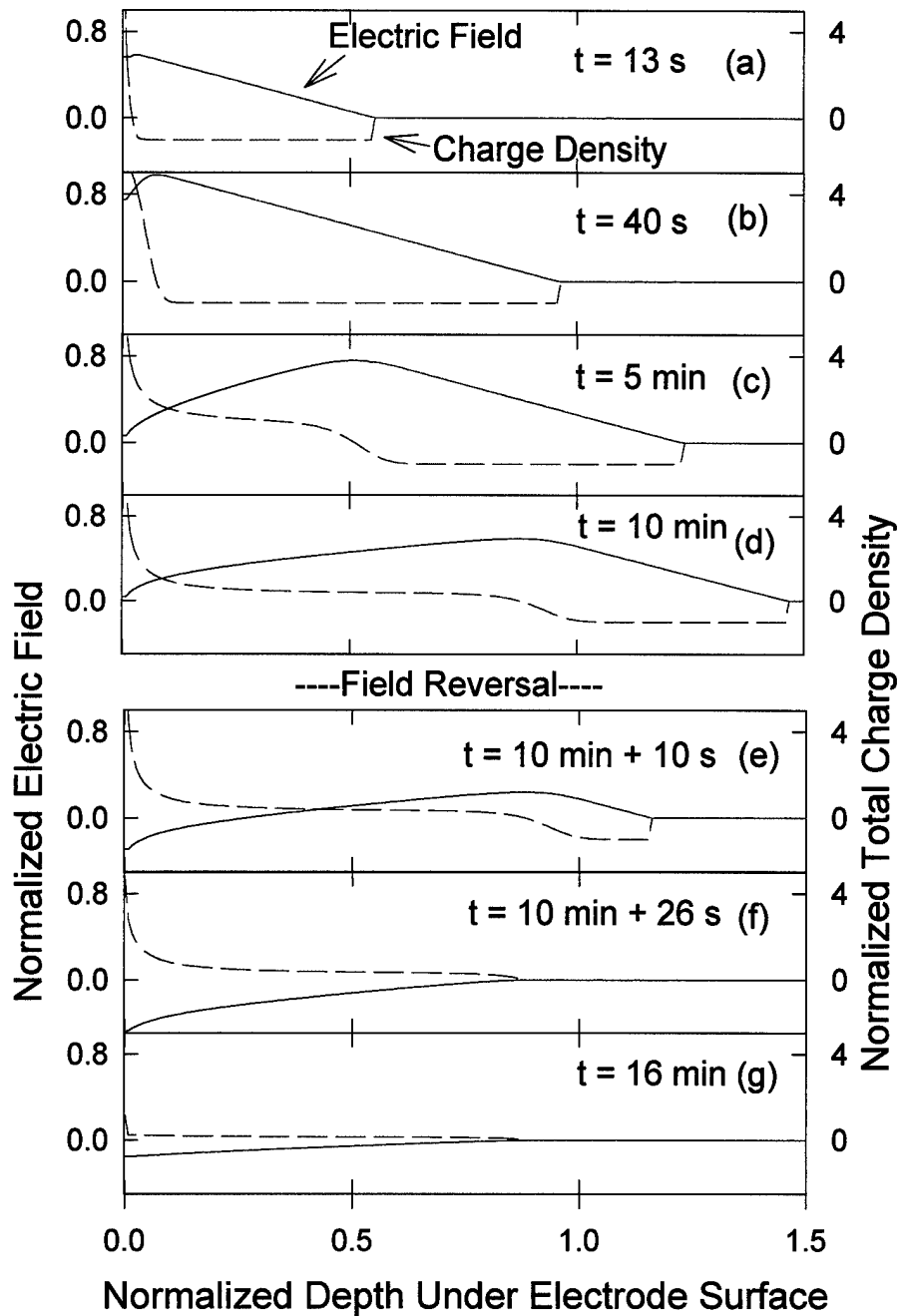Figure 4.14 Evolution under field reversal of the field and charge density. Figures (a) to (d) show poling times at +5 kV. At 10 min, between (d) and (e), the voltage is reversed. Figures (e) and (f) show the electric field drop as Na ions neutralize the depletion layer. Figure (g) shows the decrease in the magnitude of the electric field as excess positive charge is pushed out at the surface.

184

the sample, and the width of the depletion region decreases as more of the voltage is dropped across the H accumulation region; the peak of the electric field moves into the sample and decreases. The H density decreases to the background charge density (i.e. one-for-one charge exchange) within a scale comparable to the fast carrier depletion width. As long as this depth is small compared to the SH coherence length, the SH signal (proportional to V^2) is constant once the depletion region has formed.

In the simulation, the applied voltage is reversed to –5kV at t=10+ min. After a capacitive charging time (ms), a field of $-2V/L$ is added to the field shown in Fig. 4.14d. Fig. 4.14e shows the charge and field distributions 10 s later. The depletion width has decreased as the Na ions move in response to the reversed field, but the H ions have not yet responded. The SH signal is proportional to the square of the voltage drop which is almost zero at this charge distribution. After an additional 16 s (Fig. 4.14f), the depletion region has been completely eliminated and the remaining field is due to the H accumulation. Because there is still a voltage drop due to the positive charge buildup, there is a SH signal proportional to V^2. At longer times, the excess H concentration is pushed out of the sample and the SH signal decreases.

The calculated evolution of the SH signal corresponding to the charge distributions of Fig. 4.14 is shown as the curve labeled model in Fig. 4.15. A steady-state level of the SH is established after some time at a positive bias (as in Fig. 4.14 a-d). Note that the charges are still redistributing during this time but that there is no effect on the SH signal. On voltage reversal, the SH signal decreases rapidly to zero and then recovers somewhat on the time scale of the Na motion. If the sample had been shorted rather than biased at the opposite polarity, the SH signal would be expected to smoothly decrease to
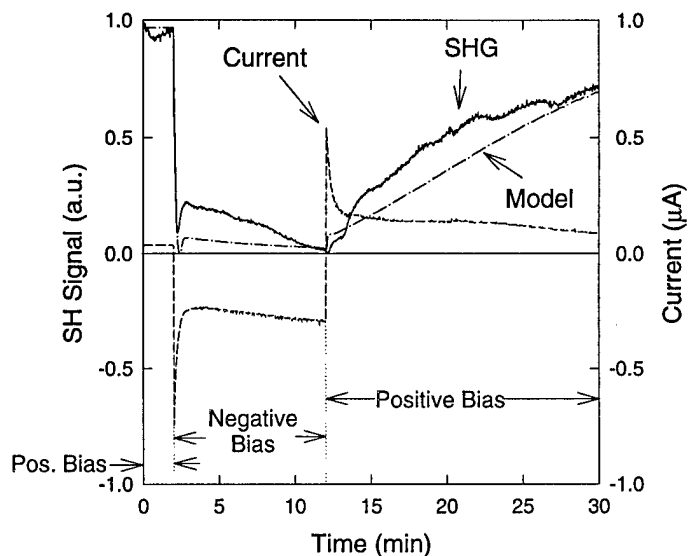
Figure 4.15 Effect of field reversal on SHG and electrical current in 6 mm thick type II (Esco G1) fused silica. Voltage applied was ±5 kV at approximately 275°C. The curve labeled model results from the simulation.

zero on this short time scale (because the voltage condition would result in an alternating electric field). The signal then decreases to zero on the time scale of the slow H motion.

The relative level of the SH after field reversal is less than that actually observed.

However, the model qualitatively explains why a SH signal is observed under the new cathode after field reversal.   The experimentally observed cathodic SH level could be higher than calculated because of two possible factors. (a) When the field was reversed, the SIMS data showed Na ions were blocked or slowed as they moved towards the new cathode, causing a pile-up of Na ions under the surface over 10-15 μm (Fig. 3.30). The model did not account for the Na accumulation. The width of the Na accumulation region is appreciable and if positively charged, will result in a significant voltage drop.

(b) If a significant amount of the nonlinearity is due to orientation of bonded H ions in

186

the field, the large accumulation of H ions will enhance the level of the cathodic SH signal observed.

The modeling must also be extended to the opposite electrode to get a complete analysis of the charge distributions. At the other end of the sample, what happens is dependent on the old cathode/new anode's distribution of Na^+ ions. If enough time passed during the prior poling such that the slow positive ion accumulation is pushed out, the former cathode region becomes non-blocking or only partially-blocking to Na^+. In this case, loss of some Na^+ can occur, up to an amount equal to that removed from the depletion region. Upon reversal, whether or not a depletion region will immediately form at the new anode is dependent on the amount of Na^+ lost in the prior poling. If no Na^+ is lost, the formation of the depletion region must wait until the field ($\sim V/L$) pushes the injected H ions out. If an amount of Na^+ equal to that removed from the initial depletion region is lost during the initial poling, when the field is reversed a new depletion region can immediately form equal in size to what was neutralized on reversal. This is why during the incubation period observed for some poled samples there is a small level of SH signal measured before a large growth. This small SH level corresponds to a small depletion region that cannot fully form until the Na column of charge is able to push all the way to the cathode surface. This is shown in Fig. 4.16. In this simulation, an amount of Na^+ (equal to the amount of charge of one depletion width w_0) was assumed to be lost (the case where the sample's cathode becomes totally non-blocking) in the prior poling. At $t = 6$ s after field reversal (Fig. 4.16a), only a small depletion region could form under the new anode, equal in charge density to the neutralized depletion region, as the Na^+ charge column moved towards the new cathode. The width of this space-charge region

187
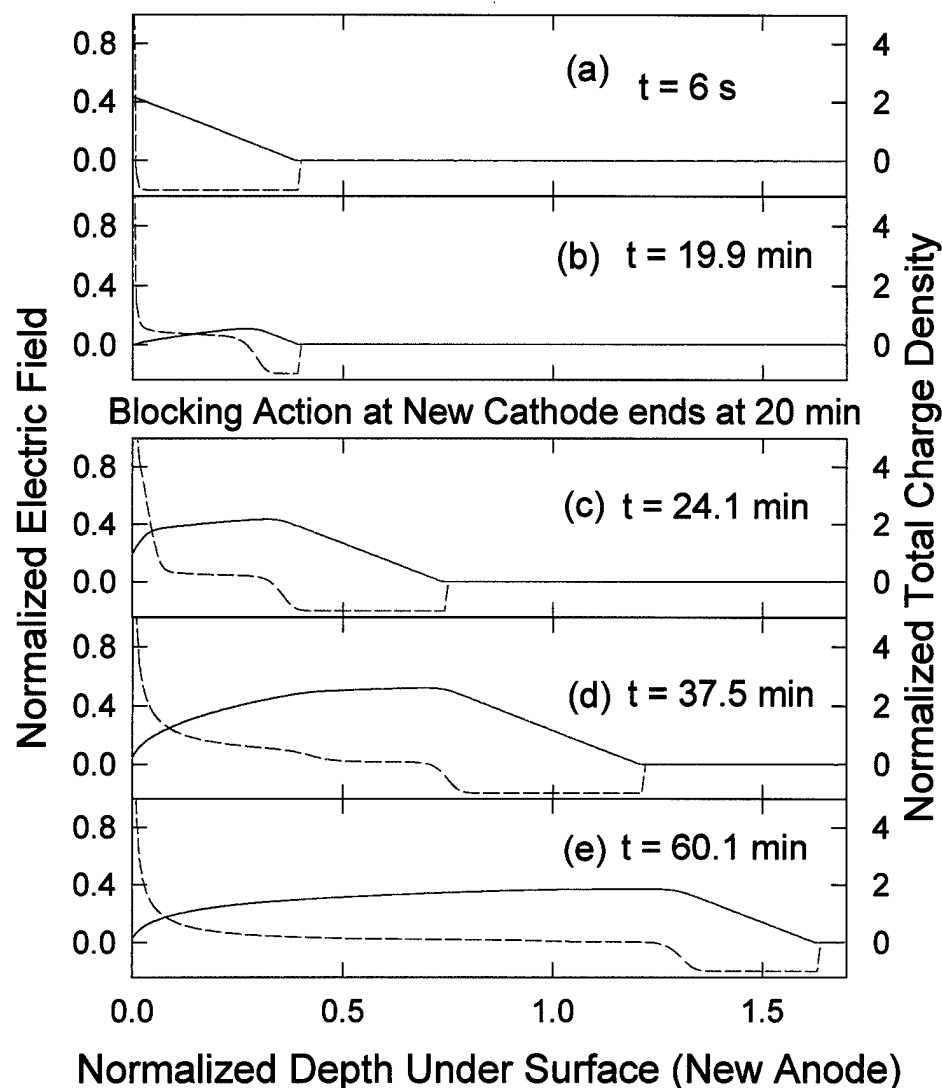
Figure 4.16 Evolution after field reversal at the new anode of the field and charge density. Figures (a) and (b) show a depletion region that can only partially form due to blocked Na movement at the positive charge accumulation at the opposite electrode. At 20 min, between (b) and (c), the Na is allowed to push through to the new cathode. Figures (c) through (e) show the evolution of a fully formed space charge region.

stays relatively constant through $t = 19.9$ min (Fig. 4.16b) as the positive charge

accumulation at the new cathode is pushed out. The simulation allowed more H^+ to move

in during this incubation period, which caused a small anodic SH signal to decay during

the incubation period. This is sometimes observed (e.g. Fig. 3.14). At $t = 20$ min, the

positive charge accumulation has been pushed out sufficiently that the Na^+ charge column can push through to the new cathode and the depletion region can fully form at the new anode (Figs. 4.16c-e).

Experimentally we observe either a slow (approximately 20 min.) growth in the SH starting immediately after the voltage reversal (figure 4.15) or, under other poling histories, an incubation period followed by the slow growth (figure 4.17). The observations force the final two assumptions: that the Na^+ ions are blocked once they have moved up to the H front and the depletion region is eliminated (Fig. 4.14f); and that
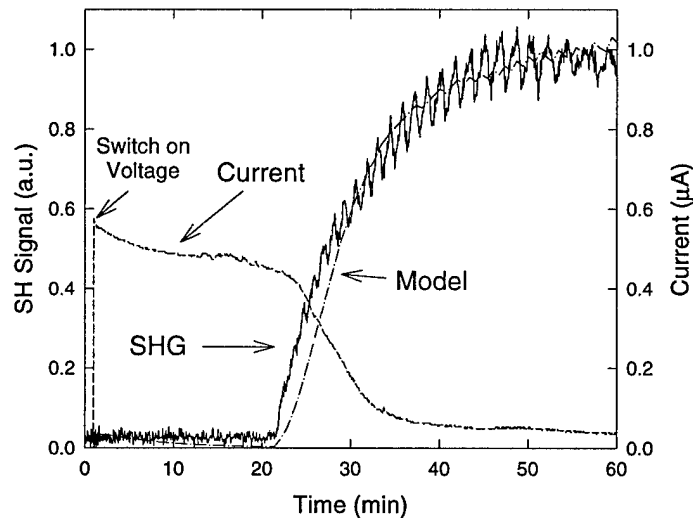
Figure 4.17 Delay of growth (incubation period) of SHG for a 6 mm type II (Esco G1) fused silica sample poled at +5 kV. In this case the sample had been previously poled for approximately 90 min. at -5 kV. The model is shown for qualitative comparison. The ripples in the observed SH signal are sometimes, but not always, observed.

the Na and H intermix in the vicinity of the front between the H and Na ionic densities to form a region with an intermediate mobility μ_M. This assumption is forced by fitting to the often observed incubation period before formation of the nonlinearity (Fig. 4.16).

Abou el Leil and Cooper[23] showed that this intermixing occurs upon field reversal for

traditional ion exchange. Because the computation at present neglects diffusion, this mixing can only be included in an ad hoc fashion as a region with an effective mixed mobility. The mixed mobility falls in-between the mobilities for sodium and hydrogenated ions alone. Fitting the data shown in Fig. 4.17, gives a mixed mobility of approximately 2×10^{-10} cm^{2}V^{-1}s^{-1}, 25 times less than the sodium mobility.

These two assumptions lead to an inhomogeneous starting distribution with H ions at both sides of the sample, a mixed ionic zone at both ends and finally a Na zone extending over the bulk of the sample. The Na ions are capped on both sides by H ionic regions. If the prior poling left an excess region of H ions on the initial anode (new cathode after field reversal) there is an incubation period with a time scale set by $\mu_H V/w$ (the depletion width) while the excess H ion density is pushed out of the sample. As this point of complete removal of excess H is reached, a depletion region forms under the opposite electrode at a time scale of $\mu_M V/d$ where μ_M is the mixed mobility and the applied voltage is dropped across the bulk of the sample of thickness d. If there is no excess H ion density (as in Fig. 4.15 where the excess density was pushed out of the sample during the negative bias cycle and it has not yet been able to accumulate on the opposite side) the nonlinearity begins to grow immediately on applying the reverse voltage.

In chapter 3, data was presented regarding the poled type II fused silica cover slips. It was found from the etching data that the position of the second etching ridge under the anode followed an approximately logarithmic trend with poling time. The SIMS data showed a correlation between the second ridge and the edge of the Li depletion region (Fig. 3.29). Because the SIMS data indicates that both Li and Na move

to form depletion regions, it is apparent that the total charge distribution N is equal to the sum of the two ions ($n_{Li} + n_{Na} = N$). Because Li is the slower ion, the total cation depletion region edge is the edge of the total charge depletion region. This trend can be compared with that predicted by the numerical model.

A numerical simulation for the cover slips was calculated by fitting mobilities to a current measurement shown in Fig. 3.22, and observations of multiple poling effects. The mobilities used in the model calculation were $\mu_{Na}=7.5 \times 10^{-11}$ cm^{2}V^{-1}s^{-1} and $\mu_{H}=5 \times 10^{-4}\mu_{Na}$, which is much lower than the values of $\mu_{Na}=5 \times 10^{-9}$ cm^{2}V^{-1}s^{-1} and $\mu_{H}=4 \times 10^{-5}\mu_{Na}$ used to fit Figs. 4.15 and 4.17. For the present parameters, a depletion region forms quickly (~1- to 2-min), followed at a much longer time with the formation of a positively charged region of excess H$^+$ ions under the surface, while the negatively charged depletion region continues to move deeper into the sample. As seen in Fig. 4.17, the model provides a qualitative fit to the data. The flattening in the middle of the model curve corresponds to the establishment of the depletion region. After the flat region of the model curve in Fig. 4.17, the space charge depth continues to increase due to surface injection of slow positive ions. The long term behavior of the numerical model goes as $\sqrt{t}$ as predicted by the analytical approximation (section 4.3.2). This appears to be faster than the limiting experimental behavior which fits a ln(t) dependence.

4.4.5 Model summary

The qualitative nature of the fit to the experimental data shows this model is only an approximate prediction of the dynamics of the space-charge region. The model is a two-carrier approximation to a more complicated situation. It was seen in the SIMS
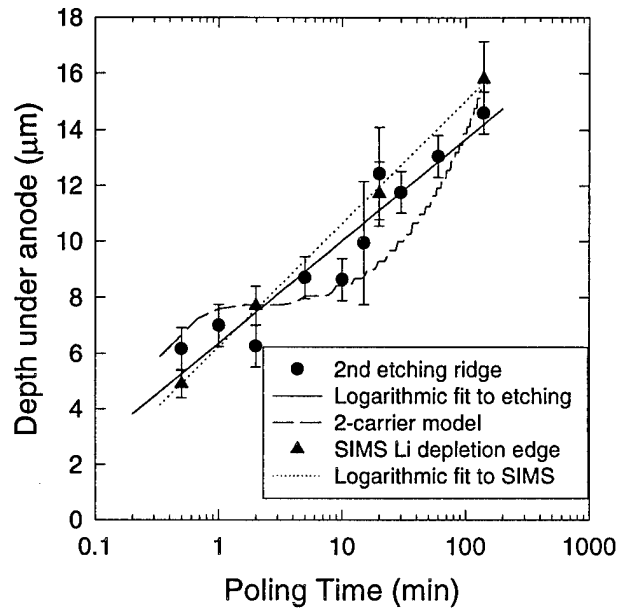
191

Figure 4.17 Comparison of etching data and SIMS data with 2-carrier model approximate best fit. The logarithmic best fits are $y = 1.583 \ln(t) + 6.366$ for the etching data and $y = 1.908 \ln(t) + 6.239$ for the SIMS data. The long term behavior of the model goes as $\sqrt{t}$.

experiments that several alkali ions move, most notably Na^+, Li^+ and K^+. If slow H^+ ion movement is included, there are 4 carrier mobilities that need to be taken into account for a more accurate prediction. Interdiffusion and impacts of each of these concentrations on their mobility are not well understood. There are other factors that make the situation more complicated as well. The SH/current data exhibited an incubation period and slow SH growth for initial polings and field reversals. The SIMS data showed that Na movement could be blocked at the cathode on field reversal. These observations forced assumptions for the model about accumulation regions and blocked ionic movement. They indicate that when some ions mix, there can be a blocking effect on the ions' mobility. The presence of impurities already diffused in the near-surface regions on initial poling can immediately affect ionic mobility and will affect the rate of growth of

the nonlinear region. The nature and distribution of these impurity levels will vary from sample to sample due to different handling and manufacturing histories. The uncertainty from sample to sample of how large a role ionic mixing and blocking play in space-charge formation adds another layer of complexity. One final factor that affects accurate modeling of the space-charge region is the role of diffusion. As mentioned in section 4.3.2, when compared with field driven effects associated with the growth of the space-charge region, diffusion effects are small. However, when ions mix before formation of the depletion region, diffusion terms can be important.

Given that the model is a first, relatively naive approximation, it still does very well to provide a qualitative understanding of how the space-charge region continues to evolve with poling time. Certainly, to reach the level of understanding concerning the formation of the nonlinearity that this model represents has required a multi-disciplinary approach, with fields of study including ionic conductivity in glass, ion exchange in glass, and nonlinear optics.

4.5 References

[1] N. Mukherjee, R.A. Myers, and S.R.J. Brueck, "Dynamics of second-harmonic generation in fused silica," J. Opt. Soc. Am. B **11**, 665 (1994).

[2] J. Cohen, "Electrical conductivity of fused quartz," J. Appl. Phys. **28**, 795 (1957).

[3] T.M. Proctor and P.M. Sutton, "Space charge development in glass," J. Am. Ceram. Soc. **43**, 173 (1960).

[4] G. Wallis and D. Pomerantz, "Field Assisted Glass-Metal Sealing," J. Appl. Phys. **40**, 3946 (1969).

[5] G. Wallis, "Direct-current polarization during field-assisted glass-metal sealing," J. Am. Ceram. Soc. **53**, 563 (1970).

[6] R.G. Gossink, "SIMS analysis of a field-assisted glass-to-metal seal," J. Am. Ceram. Soc. **61**, 539 (1978).

[7] U.K. Krieger and W.A. Lanford, "Field assisted transport of Na^+ ions, Ca^{2+} ions and electrons in commercial soda-lime glass I: Experimental," J. Non-Cryst. Solids **102**, 50 (1988).

[8] C.M. Lepienski, J.A. Giacometti, G.F. Leal Ferreira, F.L. Freire Jr., and C.A. Achete, "Electric field distribution and near-surface modifications in soda-lime glass submitted to a dc potential," J. Non-Cryst. Solids **159**, 204 (1993).

[9] D.E. Carlson, K.W. Hang, and G.F. Stockdale, "Electrode polarization in alkali-containing glasses," J. Am. Ceram. Soc. **55**, 337 (1972).

[10] D.E. Carlson, "Ion depletion of glass at a blocking anode: I, Theory and experimental results for alkali silicate glasses," J. Am. Ceram. Soc. **57**, 291 (1974).

[11] D.E. Carlson, "Anodic proton injection in glasses", J. Am.Ceram. Soc. 57, 461 (1974).

[12] Z. He, G. Borchardt, and W. Wegner, "Ionic space charge phenomena during SIMS analysis of ceramic materials," Fresenius' J. Anal. Chem. **348**, 264 (1994).

[13] R.A. Myers, N. Mukherjee, and S.R.J. Brueck, "Large second-order nonlinearity in poled fused silica," Opt. Lett. **15**, 1733 (1991).

[14] A. Von Hippel, E.P. Gross, J. G. Jelates, and M. Geller, "Photocurrent, space-charge buildup, and field emission in alkali halide crystals," Phys. Rev. **91**, 568 (1953).

[15] R.A. Myers, *Large Second-Order Nonlinearity in Amorphous SiO₂ Using Temperature/Electric-Field Poling*, Ph.D. Dissertation, University of New Mexico (1995).

[16] Quartz glass for optical data and properties, Heraeus Amersil Inc., 3473 Satellite Boulevard, Duluth, GA 30136-5821.

[17] R.H. Doremus, "Electrical conductivity and electrolysis of alkali ions in silica glass," Phys. Chem. Glasses **10**, 28 (1969).

[18] V. Jain and A.K. Varshneya, "Ionic conductivity in fused silica: II, Steady-state behavior," J. Am. Ceram. Soc. **73**, 409 (1990).

[19] G. Hetherington, K.H. Jack and M.W. Ramsay, "High temperature electrolysis of vitreous silica: I," Phys. Chem. Glasses **6**, 6 (1965).

[20] G. Hetherington, K.H. Jack and M.W. Ramsay, "High temperature electrolysis of vitreous silica: I," Phys. Chem. Glasses **6**, 6 (1965).

[21] M.C. Page, R. Oven, and D.G. Ashworth, "Scaling rules for glass based planar optical waveguides made by field assisted ion diffusion," Electron. Lett. **27**, 2073 (1991).

[22] P.G. Kazansky, A.R. Smith, P.St.J. Russell, G.M. Yang, and G.M. Sessler, "Thermally poled silica glass: Laser-induced pressure pulse probe of charge-distribution," Appl. Phys. Lett. **68**, 269 (1996).

[23] M. Abou el Leil and A.R. Cooper, "Analysis of field-assisted binary ion exchange," J. Am. Ceram. Soc. **62**, 390 (1979).

Chapter 5 Summary and Future Directions

5.1 Summary

The focus of this thesis has been the investigation of the underlying physics of the formation of the second-order nonlinearity in thermally-poled fused silica glass. The studies presented here were part of the continuing investigation by our group at the Center for High Technology Materials, University of New Mexico that began with the discovery in 1991 that a large second-order nonlinearity could be induced in fused silica through thermal poling. This effort has encompassed studies of various types of bulk fused silica, thin films, and fibers, has led to the development of an electro-optically active fiber, and is continuing towards the demonstration of a thermally-poled electro-optic fiber switch.

The specific work in this dissertation concentrated on studies of bulk fused silica; the samples were mostly type II fused silica with several ppm alkali impurities. Dynamic measurements of the second harmonic (SH) signal showed that the growth of the nonlinearity was dependent on the prior history of the sample and that complex features such as an incubation period and a signal from the cathode side could occur. It was also shown that the poling atmosphere could affect the formation. Electrical conductivity measurements in conjunction with SH signal measurements demonstrated that a space-charge current relaxation or electrode polarization occurs as the nonlinearity grows. There were several response time scales observed in the conductivity and SH measurements, again showing complex behavior. These complexities implied that a simple, single ionic charge carrier (i.e. Na^+) model was insufficient to describe the formation of the nonlinearity.

196

A technique to identify the extent of the nonlinear region was developed by using HF acid to etch cross-sections of thin glass samples. Depending on the length of time for which the sample was poled, different locations of the sample etched at different rates indicating the varying extent of the nonlinear region. When examined via microscope (optical or atomic force), relatively unetched ridges were identified, as well as a groove (from an increased etch rate) for samples poled for long periods of time. By examining multiple samples that had been poled for various amounts of time, it was found that one of the ridges moved deeper into the sample approximately logarithmically with time. This was evidence that the nonlinear region does not reach a short-term steady state, as had been predicted by the prevalent single-carrier model.

The nonlinear/space-charge region was also examined using secondary ion mass spectroscopy (SIMS). Distribution of impurity levels were measured with depth into the sample. These measurements demonstrated that multiple ions were moving, especially Na, Li, and K. Depletion regions were observed for Li and Na. Slow K ions and fast Na ions were injected from the surface by the influence of the large space-charge field, most probably from surface contamination. The H distribution also varied, but no trend was identifiable, probably due to several different bonding configurations available to H in fused silica, not all of which are active in terms of the SHG process. Peaks in K seem to match grooves measured by etching. Movement of the edge of the Li depletion region with increasing poling time correlated well with the trend observed for the ridge caused by etching. It was inferred that the Li depletion edge was the total charge depletion edge, indicating that the etching ridge also marked the end of the depletion region. The SIMS data also showed that Na^+ movement can be slowed or blocked by other ions as it moves

toward the cathode, causing a pile-up of charge. Both the etching and SIMS data showed that the space-charge region does not vanish when a thermally-poled sample is short-circuited. The alkali ion depletion regions remain, and etch-rate features still occur when etched.

A two-carrier model was developed in order to describe the complex behavior observed experimentally. The model was based on the notion of a fast ionic carrier (e.g. Na^+), and a slow ionic carrier (either a hydrogenated ion, e.g. H_3O^+ or H^+, or K^+), injected from the anodic surface into the high-field depletion region left behind by Na movement. Fitting the data to SH observations, the difference in mobility of the two carriers was several orders of magnitude and a nominal mobility ratio value of $\sim 10^{-4}$ was used based on experimental observation of other workers as well as the difference in time scales presented in chapter 3. The model was successful in describing aspects of experimental observation such as a transient nonlinearity under the cathode, the incubation period before space charge relaxation, and several response time scales. It is helpful in understanding why the depth of the space-charge region does not reach a short term steady state and why several researchers have observed a buried nonlinearity and regions of alternating charge.

Table 5.1 compares the models described in chapter 4 with behaviors that are experimentally observed. Suggestions are given on ways to improve the model to address its shortfalls.

Table 5.1 Comparison of experimental observations with the two models described in chapter 4. X's mean the model fails to predict the observation. √'s mean that the model predicts the observation. √-'s mean that the observation is qualitatively predicted but improvements can be made. Improvements to the model are suggested to correct shortfalls and deficiencies.

| Experimental Observation	Single-carrier model	Two-carrier model	Improvement suggested
Slow growth in SH from anode. (Fig. 3.9)	X One (relatively fast) μ assumed for Na.	√- Assumes an ad hoc intermediate μ for Na due to interdiffusion of slow & fast ions.	Account better for mixed alkali effect. Allow diffusion terms.
Fast response in SH from anode. (Fig. 3.12)	√ Assumes fast μ for Na.	√ Assumes fast μ for Na.	
SH Incubation period at anode. (Figs. 3.14-15, 4.17)	X Assumes immediate growth of SH	√ Assumes Na blocked by slow ion accumulation	
SH signal from cathode on field reversal. (Figs. 3.14-15, 4.15)	X Assumes signal on anode side only. Assumes accumulation of Na only at cathode with no significant voltage drop.	√- (Underpredicts) Assumes build-up of slow positive ionic charge is only effect causing SH signal. Assumes accumulation of Na only at cathode with no significant voltage drop.	Allow interdiffusion of ions to cause wider blocking region causing a pile-up of Na which leads to a significant voltage drop. If verified experimentally, allow contribution of oriented dipolar H-groups.
Slow decay of cathodic SH signal. Relatively high dc conductivity. (Figs. 3.14, 3.17, 4.15)	X Assumes signal on anode side only.	√ Assumes process controlled by outward movement of slow ion at its μ.	
SIMS depletion edge and etching ridge move ~ logarithmically deeper into sample with poling time. (Figs. 3.29, 4.17)	X Predicts steady state reached.	√- Assumes ion accumulation pushes depletion region edge deeper into sample at $\sim \sqrt{t}$ long term rate.	Unknown. Use 3-carrier model? Allow more voltage drop at cathode?
Pile-up of Na over wide region at cathode after field reversal observed with SIMS. (Fig 3.30)	X Assumes accumulation of Na only at cathode with no significant voltage drop.	X Assumes Na column can move to edge of slow ion accumulation. Pile-up of Na occurs only at cathode with no significant voltage drop.	Allow interdiffusion of ions to cause wider blocking region causing a pile-up of Na.
SIMS shows several ions move, esp. Li$^+$, Na$^+$ and K$^+$. (Fig 3.28) Relative mobilities are: $\mu_{Na}>\mu_{Li}>\mu_K$. H_2O also pulled in. (Fig. 3.36)	X One (relatively fast) μ assumed for Na.	√- (Incomplete) Assumes 2 carriers only, one fast and one slow with $\mu_{Na}>\mu_S$, where μ_S could be K$^+$ or H_3O^+.	Allow for at least three mobilities.
SIMS depletion region doesn't relax on same time scale as SH signal when shorted (Fig 3.31)	X Assumes one μ. Relaxation of depletion region occurs on this time scale	√ Predicts only partial relaxation of depletion region. (Fig. 4.8)	

5.2 Future directions

The etching and SIMS experiments were successful in indicating the extent of the nonlinear region that develops in type II fused silica. An unsuccessful attempt (not presented here) was made at a measurement of the electric field that develops in the space-charge region. After breaking thin cover slips to expose the broken edge, samples were examined using Electric Force Microscopy (EFM), in order to examine the field along the break. EFM uses the same equipment as an atomic force microscope, except it runs in a special mode with a longer conductive tip. The lack of success could have originated in one of several factors: contamination screening the field after the break, too much topography along the break, etc. Future work might investigate whether or not these factors might be overcome with a more controlled experiment.

Other methods of measuring the internal electric field might be devised. Fused silica samples doped with rare earths could be manufactured or prepared (e.g. ion implantation). After thermal poling, measurement of electric field-induced Stark shifts in luminescence could provide a direct measurement of the field. It may also be possible to observe Stark shifts using photochromic dyes, after finding an appropriate way to incorporate or apply the dye. A more direct measurement of the electric field would be useful to study other types of fused silica that have fewer impurities such as type III and type IV, as well as Ge-doped fused silica.

The question still remains for purer forms of fused silica of what species plays the role of alkali charge carriers. Poled Ge-doped fused silica exhibits a comparable nonlinearity as has been demonstrated in thermally-poled optical fibers and preforms. Future studies should certainly include bulk samples of Ge-doped SiO_2 especially since

most applications will be made in this media. In fibers, the sample thicknesses are small, and H^+ or H_3O^+ might play a role. As mentioned in section 2.2.4.1, Hofstein[2] studied SiO_2 films and found slow and fast hydrogen motion. It's possible that the fast hydrogen motion can leave behind a space-charge/depletion region in thin films and fibers.

Relatively alkali-free type III and IV fused silicas can also form a space charge region through thermal poling, but often require defect-enhancing treatment first, such as x-ray, γ-ray or heat treatment. Treatment isn't always necessary as was shown for the type III samples that were thermally poled and presented in chapter 3. In an interesting connection, metal-SiO_2-Si (MOS) devices, with their thin layer of SiO_2, can become charged, and the charge trapping is classified as consisting of 4 types[3]. Two charge traps are due to the two MOS interfaces, but the two others are caused by (a) mobile (alkali) ionic charge and (b) oxide trapped space charges associated with defects. The oxygen-related defects are usually electrically neutral traps, but can be charged from holes or electrons in the SiO_2 (e.g. non-bridging oxygen hole centers). Studies based on SiO_2 films and electrets indicate that silanol (SiOH) groups along with water or hydronium play an important role in forming stable trapped negative charge through the reaction:[4]

$$\equiv SiOH + H_2O = SiO^- + H_3O^+ \tag{5.1}$$
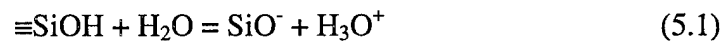
Silanol groups are reported to either be the source of conductivity due to mobile protons or due to their ability to attract water molecules which in turn react to form more silanol groups. It was shown that in charged films that charge retention after poling at room temperature could be prolonged by substitution of surface silanol with other nonconducting groups.[4]

It is highly possible that the H ion plays the role of the major charge carrier in alkali-free fused silica types and that a high field space-charge region forms, depleted of H ions, leaving behind negatively charged defect centers. Nuclear reaction analysis might be used to study profiles of hydrogen or more preferably, deuterium that has been introduced into the sample. This area remains to be investigated more thoroughly.

As described in chapter 4, the two-carrier model could be improved. It could be made more accurate by making it a 3 or 4 carrier model. By adding diffusion terms, allowing impurity accumulation regions at the surface, and accounting for the mixed alkali effect, time response behavior can be better modeled.

The question of which nonlinear effect: $\chi^{(3)}E_{dc}$ or dipole orientation, contributes most to the $\chi^{(2)}$ was left unanswered in this thesis. The model underpredicted the level of cathodic SH signal that was actually observed. The observed larger level could be due to a Na^+ pile-up/accumulation over a wide region that was not included in the model, but it could also be due to orientation of dipolar H-related groups in the space-charge region, which also was not included in the model. If more H-related groups are located in the high-field space-charge region, the nonlinearity will be enhanced if orientation plays a significant role. The question of whether oriented H groups enhance the nonlinearity could be studied by hydrating and subsequently poling bulk fused silica samples. The hydration could be accomplished by treating the samples in an autoclave/hydration bomb such as those used for geological studies. Several studies were presented in section 2.2.3.3 in which hydration bombs were used to study the effect of hydration on conductivity in fused silica.

Thermal poling has the potential of real device application. Most immediately this application is the fabrication of electro-optically active fibers for switching and modulation, as well as the manufacture of quasi-phase matched nonlinear gratings in fibers for frequency-doubling. For device reproducibility and optimized interaction, it is desirable to predict with accuracy where the nonlinear region will appear in the fiber. This thesis has shown that alkali impurities and water at the sample surface can change the field distribution of the space charge region and push it deeper into the sample with poling time. If a steady state depletion region is desired, contaminants would need to be removed and poling carefully controlled. However, alkali or water contaminants could also be used to our advantage; the nonlinear interaction can be optimized by determining and controlling the amount of contamination and poling time necessary to center the electric field region in the fiber. This would be by no means an easy task due to the careful controls needed for such a study.

5.3 References

[1] S.R Hofstein, "Proton and sodium transport in SiO_2 films," IEEE Trans. Elect. Dev. **ED14**, 749 (1967).

[2] S.M. Sze, *Physics of Semiconductor Devices*, 2nd edition, Wiley & sons, New York, 1981.

[3] W. Olthuis and P. Bergveld, "On the charge storage and decay mechanism in silicon dioxide electrets," IEEE Trans. Electrical Insulation **27**, 691 (1992).